UNIVERSITÀ DEGLI STUDI DI PARMA
FACOLTÀ DI SCIENZE MATEMATICHE FISICHE NATURALI

DOTTORATO IN
SCIENZA E TECNOLOGIA DEI MATERIALI INNOVATIVI
XXIII CICLO

MOVPE GROWTH AND STUDY OF III-V MULTI-JUNCTION STRUCTURES FOR ADVANCED PHOTOVOLTAIC APPLICATIONS

Tutors:
Prof. Luciano Tarricone
Prof. Antonella Parisini

Coordinatore:
Prof. Anna Painelli

Candidato:
Michele Baldini

Contents

Introduction **1**

1. The energy question **11**

1.1 Fossil fuel exploitation 11

1.2 Nuclear power 17

1.3 Renewable sources 21

1.4 Actual PV situation, grid parity and Italian PV market 25

References 29

2. The physics of solar cells **31**

2.1 Introduction 31

2.2 Solar energy 33

2.2.1 Air Mass 33

2.3 Basic operation principles 35

2.3.1 Ideal I-V characteristic 35

2.3.2 Short-circuit current 37

2.3.3 Open-circuit voltage 39

2.3.4 Fill factor 40

2.3.5 Efficiency 42

2.3.6 Effects of parasitic resistances 44

2.3.7 Two-diode model....46
References....48

3. Third generation photovoltaics....49
3.1 History of solar cells....49
3.2 Three generations of solar cells....52
3.2.1 First generation....54
3.2.2 Second generation....55
3.3 Solar cell efficiency limits....58
3.3.1 Efficiency loss mechanisms....58
3.3.2 Shockley-Queisser efficiency limit (Detailed balance)....60
3.4 Third generation innovative concepts....62
3.4.1 Multi-junction solar cells....62
3.4.2 Quantum well solar cells....66
3.4.3 Intermediate-band solar cells....70
3.4.4 Hot carriers solar cells....73
3.4.5 Spectrum conversion....78
3.4.6 Low cost alternatives: dye-sensitized and organic solar cells...81
References....85

4. Metal organic vapour phase epitaxy....91
4.1 Introduction....91
4.2 MOVPE operating principle....93
4.3 Thermodynamics....95
4.4 Kinetics, mass transport and fluid dynamics....98
4.4.1 Heterogeneous reactions....99
4.4.2 Homogeneous reactions....100

4.4.3 Growth regimes 101
4.4.4 Fluid dynamic aspects 103
4.5 Metal-organic precursors 107
4.6 MOVPE system at Parma SEMLABS 111
References 114

5. InGaP/GaAs MQW structures 115
5.1 Introduction 115
5.2 Admittance spectroscopy 122
5.3 Photoelectric spectroscopy 128
5.3.1 Experimental setup 130
5.3.2 The photoelectric signal 131
5.3.3 Spectral response 133
5.3.4 Line-shape analysis 135
5.3.5 Modulation frequency dependence of PE signals 138
5.3.6 Temperature dependence of PE signals 149
5.3.7 Conclusions 158
References 160

6. GaAs/GaSb tandem structures 163
6.1 Introduction 163
6.2 Low band gap materials for PV and TPV 165
6.2.1 Germanium 165
6.2.2 Gallium Antimonide 167
6.3 GaSb: physical properties, applications and Hall analysis 169
6.3.1 Band structure 170
6.3.2 Doping 172

6.3.3 Fields of interest 173
6.3.4 Hall measurements in Te-doped GaSb substrates 175
6.4 GaSb bottom junction 179
6.4.1 GaAs growth on GaSb 181
6.4.2 Experimental procedures 182
6.4.3 Dark I-V characterization 185
6.4.4 SIMS characterization 186
6.4.5 Light response with solar simulator 190
6.4.6 Effective diffusion length extracted from light I-V curves 192
6.5 GaAs tunnel junction 198
6.5.1 Theory of the tunnel junction 199
6.5.2 MOVPE growth of GaAs n^{++}-p^{++} tunnel junctions 202
6.6 GaAs/GaSb: the tandem structure prototype 205
6.6.1 Experimental procedures 206
6.6.2 Preliminary characterization 207
6.7 Conclusions 209
References 212

Conclusions and perspective **215**

Acknowledgments **221**

Introduction

The energy question is one of the most important problems of modern society. Indeed, the whole human history has been characterized, since the beginning, by the search for energy sources. At first the basic energy request consisted mainly in household heating and cooking, while, since the last centuries, energy was needed to sustain the growing industrialization. Nowadays, the energy demand is an urgent issue connected with the drawbacks of fossil fuels (oil, coal and natural gas), which provide 80% of the total energy we consume [1]. These energy sources, in fact, suffer from two main disadvantages: i) their reserves are running out, making their cost higher and higher; ii) their exploitation produces harmful effects, such as the emission of CO_2 and other gases that contribute to environment pollution and global warming. Moreover, in the next future, the world energy demand is expected to dramatically increase, due to the extremely fast economic development of Asian nations, like China and India, that is going to bring roughly 2.5 billion people to our occidental lifestyle.

Nuclear power may seem a good option to replace fossil fuels, since the fission process does not emit any CO_2. Nuclear reactors, however, imply several other negative issues. First of all, uranium itself is a finite resource and cannot represent a long-term solution to the energy question. Secondly, the construction of new nuclear power plants needs large capital costs and takes a long time, equal to ~10 years. Finally, the safe long-term disposal of nuclear waste is still an unresolved question.

Considering all the issues related to fossil and nuclear energy sources, the only realistic solution to the energy crisis is represented by the large employment of renewable energy sources, assisted by global energy conservation policies. Energy saving, in fact, plays a key role in this challenge; it would not make sense to face the complex energy question without limiting the several wastes that characterize our lifestyle. It has been proved that, in industrialized countries, a decrease in energy consumption would not result in a deterioration of the life standards [2].

Renewable energy sources use natural inexhaustible resources with no, or minor, harmful side effects for the environment and, unlike nuclear plants waste products, cannot be used for military offensive. As the cost of ordinary fuel is increasing, renewables are getting cheaper. Different reasons contribute to this price trend. First of all, while fossil fuel technologies are mature and well known, renewable technologies are rapidly evolving. In this way, innovation and scientific research permit to constantly increase the efficiency of energy conversion, leading to a competitive $/kW ratio. Moreover, once the renewable plants have been built, the fuel is limitless, unrelated to the market fluctuations, and free, forever.

Photovoltaic represents one of the most interesting renewable technologies, since it's the only one that can convert solar energy directly into electricity, without the use of any moving parts. Solar radiation, moreover, is abundant, inexhaustible and diffuse all over the world. Solar cell technology may thus contribute to reduce disparities among the world's nations, considering that most poor countries have plentiful solar energy.

The photovoltaic effect, which is at the basis of solar cells, is the process in which two dissimilar materials in close contact produce an electrical voltage when struck by light. Although it was observed for the first time by French physicist A. E. Becquerel as early as in 1839, the first solar devices appeared only in the 1950s, thanks to the development of semiconductor physics.

The light shining on a solar cell produces both a current and a voltage to generate electric power that is consumed by the external load (Figure 1). This process requires, firstly, a material that, by the absorption of the incident light, generates hole-electron pairs, and secondly, the movement of these charge carriers from the solar cell into an external circuit. Although a variety of materials and processes can potentially satisfy the requirements for photovoltaic energy conversion, nearly all the commercially available solar cells use semiconductor materials in the form of a *p-n* junction.

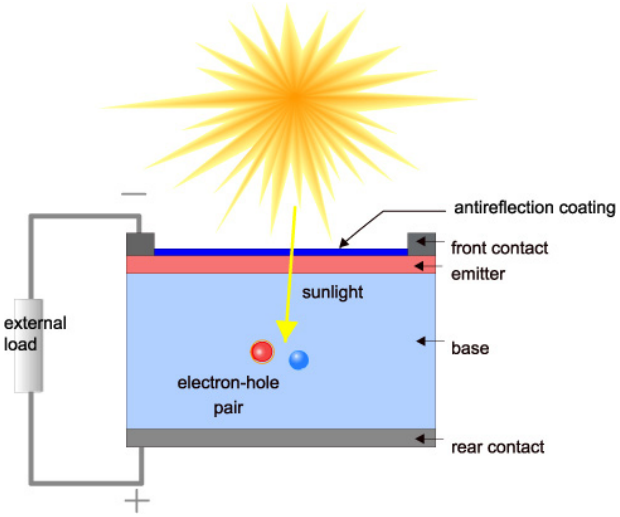

Figure 1: Cross section of a *p-n* junction solar cell with its main components.

The generation of current in a solar cell involves two key processes, as shown in Figure 2. The first process is the absorption of incident photons to create electron-hole pairs, which will be generated in the solar cell provided that the incident photon has an energy greater than that of the band gap. However, electrons (in the *p*-type material), and holes (in the *n*-type material) are meta-stable and will only exist, on average, for a length of time equal to the minority carrier lifetime before they recombine. The second process, the collection of the carriers, prevents this

recombination by the action of the electric field existing at the *p-n* junction to spatially separate the electron and the hole. If the light-generated minority carrier reaches the *p-n* junction, it is swept across the junction by the electric field, where it is now a majority carrier. If the emitter and base of the solar cell are connected together (i.e., if the solar cell is short-circuited), the light-generated carriers flow through the external circuit.

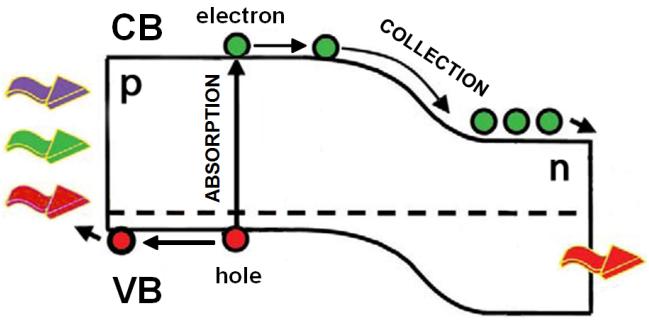

Figure 2: Band structure of a *p-n* junction solar cell with the two main processes needed for the generation of the photocurrent: light absorption and carriers collection.

Since the 1950s, when the first silicon solar cell was produced, three generations of devices were conceived with the purpose of improving the production cost/conversion efficiency ($/W) ratio to become market-competitive [3].

The first generation refers to high quality, and hence low defect, photovoltaic devices based on mono- and polycrystalline silicon. These reached a quite high conversion efficiency (η~25%), which is approaching the theoretical limit for single band gap devices of ~31% that was calculated in 1961 by Shockley and Queisser [4]. However, such devices are labour and energy intensive and are not likely to get lower than 1 $/W.

Second generation technology involves thin-film solar cells of polycrystalline materials, such as CdTe, CIGS and amorphous Si. These devices are produced by low cost growth techniques such as vapour deposition and electroplating. Moreover, by

using only few micron thick active layers, such processes can bring costs down under 0.50 $/W. The resulting conversion efficiency is, however, a little minor than Si-based devices.

The third generation is based on devices that mean to exceed the Shockley-Queisser limit by reducing the main energy loss mechanisms that affect solar cells: i) the failure to absorb below band gap energy photons and ii) the thermalization of high energy hole-electron pairs. The innovative concepts that are supposed to achieve this purpose are: multiple band gap structures (bulk-like [5] and low-dimensional multijunctions [6, 7]), hot carrier cells (obtained through multiple exciton generation [8] and selective energy contacts [9]), and the modification of the incident spectrum (up- and down-conversion [10]). A further type of third generation solar cells (dye-sensitized [11] and organic [12] solar cells) aims at cutting down the cost of photovoltaic devices by using alternative materials such as organic compounds and conductive polymers, accepting the resulting lower efficiencies.

This PhD thesis deals with the study of two types of third generation structures based on multiple band gaps, which is the only innovative concept that led to exceed the 31% conversion efficiency given by the Shockley-Queisser limit.

The first structure analyzed in this work is based on a InGaP p-i-n junction with an intrinsic region consisting of 30 periods of 8 nm thick GaAs quantum wells (QW) and 12 nm thick InGaP barriers, conceived to be part of a quantum well solar cell (QWSC) (Figure 3a). This heterostructure was grown by a low pressure MOVPE reactor, with the employment of liquid alternative metalorganic precursors for the group V elements, terbutylarsine (TBAs) and terbutylphosphine (TBP), in place of the standard gaseous ones arsine (AsH_3) and phosphine (PH_3), leading to a strong decrease of the toxicity of the growth process. In particular, it was investigated the light response of the structure by an accurate photoelectric spectroscopy (PES) study conducted by varying the modulation frequency of the optical excitation and the

sample temperature [13, 14]. This type of measurement on semiconductor structures consists in recording, as a function of the wavelength of the exciting light, the electrical signal (current or voltage) produced by the optically generated excess charge carriers. Through the analysis of the acquired spectra, it is possible to obtain important information, such as the absorption of the incident light, the quantized level energy position in QWs, the transport mechanisms that dominate in the devices in different conditions.

The subject of the second part of this PhD research was the realization of a relatively simple monolithic tandem structure for photovoltaic applications (Figure 3b). In particular, the main purpose was to study and develop the bottom part of the whole structure. In order to achieve a p-n junction able to absorb, and efficiently convert, the low energy radiation, a Zn-heavily doped GaAs layer was deposited by MOVPE on n(Te)-doped GaSb substrates, so that the high temperature of the growth process (T_g=600° C) induced the interdiffusion of Zn from GaAs in GaSb, forming a buried GaSb p-n homojunction [15]. Both the different Zn doping levels and the time-temperature annealing values were investigated in order to control the depth of the junction, which has a relevant role in controlling the collection of light-generated carriers. The GaAs/GaSb samples were characterized by electrical (dark and light I-V) and SIMS (secondary ion mass spectrometry) measurements. Once the bottom junction was realized, the tandem multi-junction was completed by the growth of the upper, all-GaAs-based, part of the structure, consisting of a n^{++}-p^{++} GaAs tunnel diode and a p-i-n GaAs top junction. The electrical behaviour of differently doped tunnel junctions and of the resulting complete structure was studied.

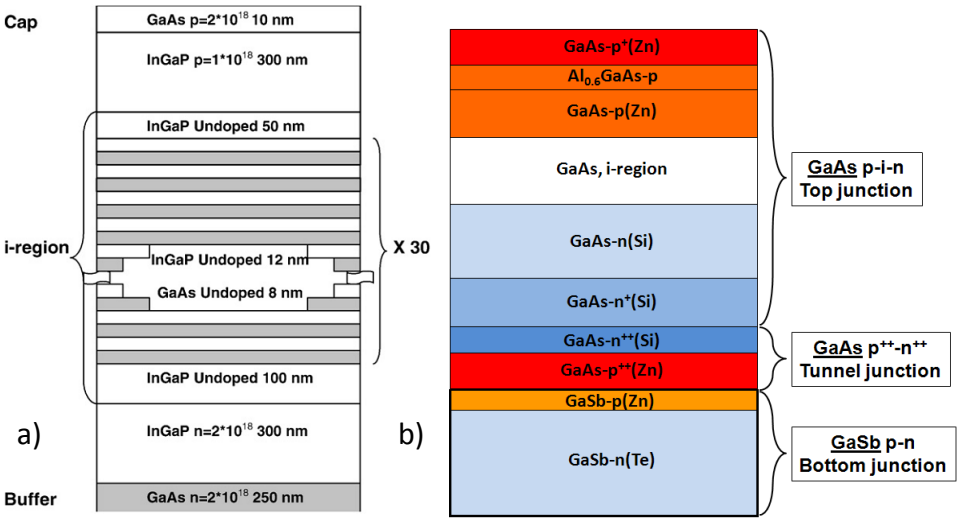

Figure 3: (a) InGaP *p-i-n* structure with 30 stacked GaAs/InGaP MQW in the intrinsic region and (b) GaAs/GaSb tandem structure, with the three main constituent parts evidenced.

This thesis layout is the following:

- The first chapter ("The energy question") deals with the actual energy crisis and the effects that the exploitation of fossil fuels has in terms of environmental damage and geopolitical issues. Among the alternative energy sources, photovoltaics emerges as one of the most promising renewable technologies.
- In the second chapter ("The physics of solar cells") the operating principle and the physical properties of solar devices are described, starting from the analysis of the solar spectrum on the Earth's surface, up to the main parameters that contribute to define the conversion efficiency, together with the solar cell equivalent circuits.

- The third chapter ("Third generation photovoltaics") deals with the different solar device technologies that were developed until now. The main efficiency losses and the theoretical efficiency limit for single junction solar cells are discussed. A review of the current literature regarding the innovative concepts at the basis of third generation photovoltaics is also provided.
- The subject of the fourth chapter ("Metal organic vapour phase epitaxy") is MOVPE, which is the main current technique for the production of optoelectronic devices and in particular of high efficiency multi-junction solar cells. The growth mechanisms and the different processes involved in this epitaxial growth method are explained and the MOVPE system employed in this research work is described.
- In the fifth chapter ("InGaP/GaAs MQW structures") the first structure studied in this work, based on a InGaP p-i-n junction with GaAs QWs, is presented, with its main physical and structural properties. The investigation of the response to the light of the structure by an accurate photoelectric spectroscopy (PES) study is reported.
- The sixth and last chapter ("GaAs/GaSb tandem structures") deals with the second type of photovoltaic structure that was designed and produced, consisting in a relatively simple monolithic GaAs-based tandem structure grown on GaSb substrates. The study of the single parts of the structure is presented, with a particular attention to the bottom junction, based on a buried GaSb p-n homojunction, which was realized with an innovative method.

References

[1] Key world energy statistics, International Energy Agency, 2010

[2] V. Smil, Energy, Oneworld, Oxford, 2006

[3] M.A. Green, Prog. Photovol.: Res. Appl. **9**, 123-135 (2001)

[4] W. Shockley, H.J. Queisser, J. Appl. Phys. **32**, 510-519 (1961)

[5] W. Guter, J. Schöne, S.P. Philipps, M. Steiner, G. Siefer, A. Wekkeli, E. Welser, E. Oliva, A. W. Bett, Frank Dimroth, Appl. Phys. Lett. **94**, 223504 (2009)

[6] K.W.J. Barnham, G. Duggan, J. Appl. Phys. **67**, 3490–3493 (1990)

[7] A. Luque, A. Marti, Phys. Rev. Lett. **78**, 5014 (1997)

[8] M. Wolf, R. Brendel, J.H. Werner, H. J. Queisser, J. Appl. Phys. **83**, 4213 (1998)

[9] G. Conibeer, M. Green, R. Corkish, Y. Cho, E. Cho, C. Jiang, T. Fangsuwannarak, E. Pink, Y. Huang, T. Puzzer, T. Trupke, B. Richards, A. Shalav, K. Lin, Thin Solid Films **511**, 654 (2006)

[10] T. Trupke, M.A. Green, P. Wurfel, J. Appl. Phys. **92**, 4117 (2002)

[11] M. Gratzel, Nature **414**, 338–344 (2001)

[12] P. Peumans, S. Uchida, S.R. Forrest, Nature **425**, 158–162 (2003)

[13] A. Parisini, C. Ghezzi, L. Tarricone, M. Baldini, S. Vantaggio, E. Gombia, J. Appl. Phys. **106**, 113709 (2009)

[14] A. Parisini, C. Ghezzi, L. Tarricone, S. Vantaggio, M. Baldini, E. Gombia, Jpn. J. Appl. Phys. **49**, 122001 (2010)

[15] M. Baldini, C. Ghezzi, A. Parisini, L. Tarricone, S. Vantaggio, E. Gombia, A. Motta, A. Gasparotto, Cryst. Res. Technol. 1–5 (2011)

Chapter 1

The energy question

1.1 Fossil fuel exploitation

The energy supply is one of the most important issue of the modern society. Our everyday life is influenced by the energy availability and the way we produce it heavily reflects upon the environment. Over the last century the global energy demand has dramatically grown, pushed by the industrialization (Figure 1.1a). In the next future this production is going to increase more and more, driven by the extremely fast economic development of Asiatic nation, like China and India, that is going to bring something like 2.5 billions people to our occidental lifestyle. The challenge for the energy supply wouldn't be so crucial if energy was not produced for the vast majority from fossil fuels. Nowadays, in fact, approximately the 80% of the total energy we consume comes from the combustion of oil (~33%), coal (~27%) and natural gas (~21%), as showed in Figure 1.1b [1].

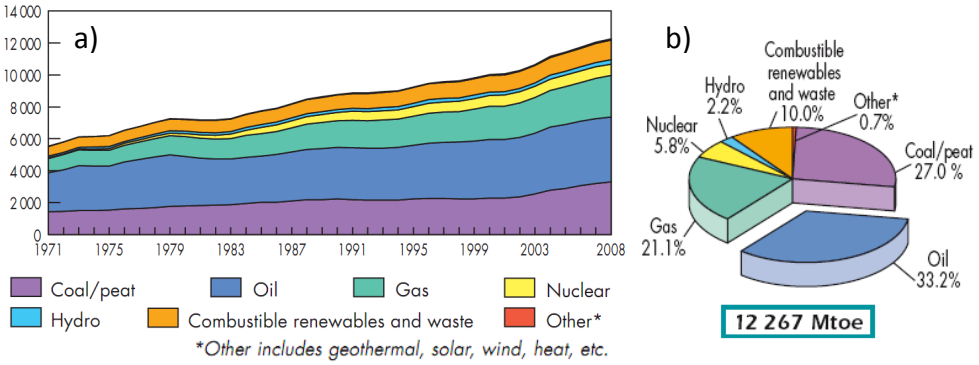

Figure 1.1: a) Evolution of world total energy supply by fuel in million tons of oil equivalent (Mtoe); b) 2008 fuel share of world total energy supply (Source: International Energy Agency, 2010).

These energy sources have been fundamental for the development of our society during the 20th century, but are characterized by two main drawbacks, which are getting more and more pressing: i) the fossil fuels reserves are limited and their cost increasingly higher (Figure 1.2); ii) their exploitation produces harmful effects, such as CO_2 and other gases emission that, among other things, contribute to the global warming.

Concerning the shortage of the reserves, the most resounding example is given by the so-called peak oil, introduced by M. King Hubbert in 1956 [2]. Peak oil is the point in time when the maximum rate of global petroleum extraction is reached, after which the rate of production enters terminal decline. This concept is also valid for natural gas, even if with longer times (Figure 1.3). The peak will occur when easily accessible oil (or gas) is exhausted. After that moment there will still be considerable fossil fuels in the ground, but they will be so expensive to extract that other energy sources will be preferable. The pessimists believe that the peak is right now, in 2010, the optimists shift it 30 years later. Whoever is right, the problem of "easy extraction" of oil and natural gas is urgent and needs a prompt response.

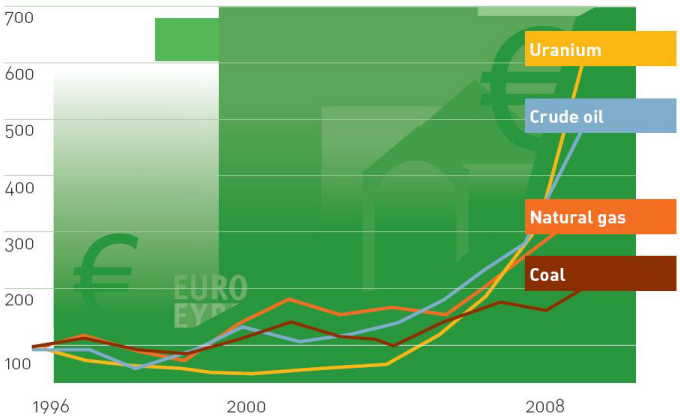

Figure 1.2: Evolution of energy fuel cost over the last 15 years. 1996 values are normalized to 100 (Source: German Renewable Energies Agency, 2009.

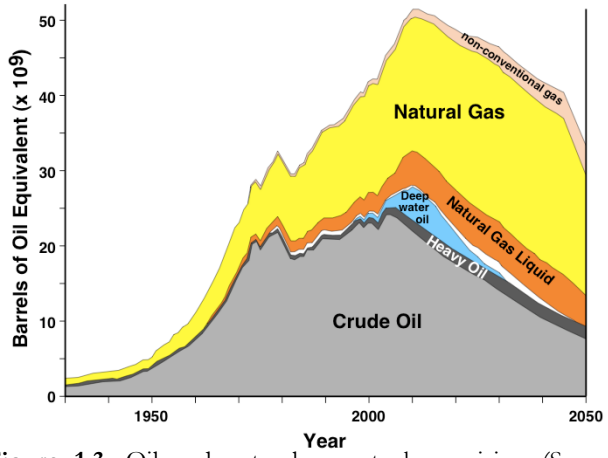

Figure 1.3: Oil and natural gas stock prevision (Source: Association for the study of Peak Oil and gas, ASPO, 2007).

Coal is not included in this survey, because its main problem is not availability (at least for the next 100 years), but environmental sustainability.

The burning of coal, oil and gas is the largest human-correlated source of carbon dioxide (Figure 1.4), which is one of the primary greenhouse gases (besides water

vapor, methane, nitrous oxide, and ozone) contributing to global warming (Figure 1.5). The amount of carbon, which in this way is injected in the air (ca. 7 Gt/year) looks marginal if compared to the natural exchange between the biosphere and the atmosphere (ca. 200 Gt/year) but it's enough, on the long term, to gradually increase CO_2 concentration (+30% since industrial revolution), alter the Earth's radiation balance and trigger artificial climate variations [3]. Moreover, fossil fuel combustion produces other air pollutants, such as nitrogen oxides, sulphur dioxide, volatile organic compounds, heavy metals and also sulfuric, carbonic, nitric acids which fall to the Earth as acid rain, impacting both natural areas and the built environment.

Fossil fuels also contain radioactive materials, mainly uranium and thorium, which are released into the atmosphere: in 2000, about 12,000 tonnes of thorium and 5,000 tonnes of uranium were released worldwide from burning coal [4]. This also generates large amounts of bottom ash and fly ash.

Environmental concerns come also from the extraction and distribution of fossil fuels. Coal mining methods have negative environmental impacts and imply serious risks for man working. Offshore oil drilling and transportation by tanker ships represent awful hazards to aquatic organisms and coastal areas: infamous examples are, respectively, the recent Deepwater Horizon oil spill in the Gulf of Mexico, from which flowed up to 4 million barrels for three months from April 2010, and the Exxon Valdez accident, occurred in Alaska on March 1989, that, although it brought about the release of a relatively low amount of oil (750.000 barrels), is considered to be one of the most devastating human-caused environmental disasters for its consequences on the ecosystem.

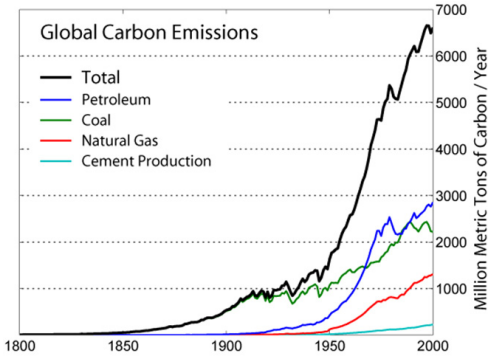

Figure 1.4: 1800-2000 Annual carbon emission broken down into various fuel types (Source: Carbon Dioxide Information Analysis Center, Oak Ridge National Laboratory, 2009).

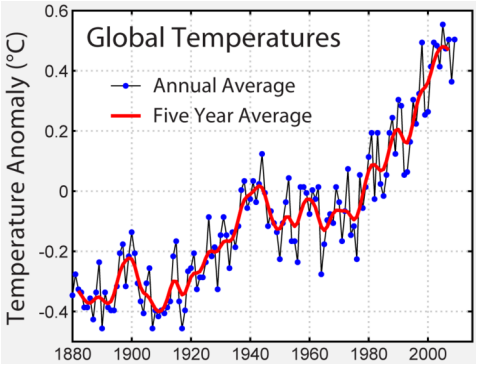

Figure 1.5: 1880-2009 Global mean surface temperature difference relative to the 1961–1990 average (Source: NASA's Goddard Institute for Space Studies, 2009).

Furthermore, the fossil fuel-based economy implies serious geopolitical issues, since the most of the energy reserves are placed in a few geographic regions. During the last half of the 20th Century, several related events occurred that complicated the actual energy picture and made future predictions more difficult. Beginning from 1950s and 1960s, most oil and gas reserves gradually came under control of state oil companies. Today, just ~10% of oil and gas reserves are held by private companies, whereas the remaining part is controlled by the governments of the countries in which the vast majority of reserves occur, such as Saudi Arabia, Iran, Iraq, United Arab Emirates and Venezuela. Political instability in the Middle East, beginning with the Arab-Israel Yom Kippur War in 1973 and the Iranian Revolution in 1979, with the resulting willingness of state oil companies to use the power of their resources for political objectives, have resulted in increasing price instability (Figure 1.6). In this context, it is relevant to remember that, at the moment, seven of the fifteen largest suppliers of oil to the United States are on the State Department's Travel Warning List, for their "long-term, protracted conditions that make a country dangerous or unstable" [5].

In July 2010, the German Bundeswehr Transformation Center, an agency directly connected with German Army Forces, asserted that oil will become one decisive factor in determining the new landscape of international relations: "The relative importance of the oil-producing nations in the international system is growing. These nations are using the advantages resulting from this to expand the scope of their domestic and foreign policies and establish themselves as a new or resurgent regional, or in some cases even global leading powers." In the same report, the authors suggest that the likely peak oil date is just 2010 and that the dramatic effects of peak oil on market and prices will begin to show in the next ten to fifteen years [6].

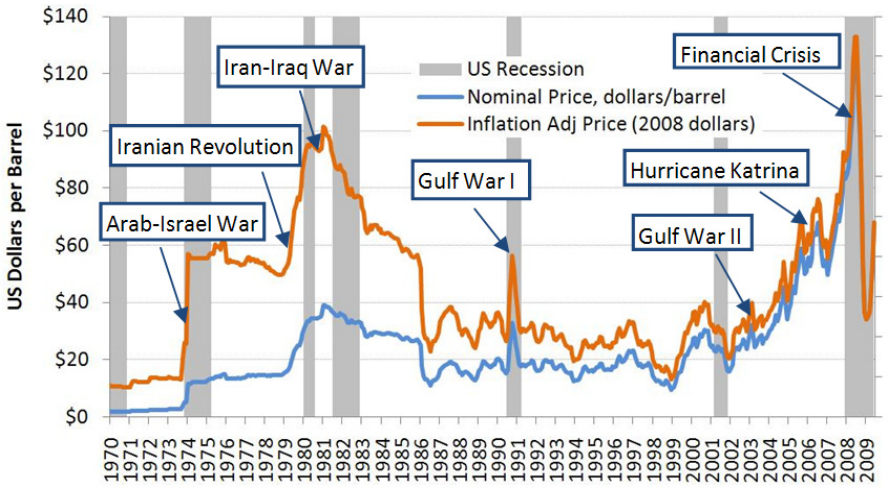

Figure 1.6: Nominal and inflation-adjusted oil prices in the 1970-2009 period, with the main correlated events. In grey the recession periods (Source: US Energy Information Administration, National Bureau of Economic Research, 2010).

1.2 Nuclear power

Nuclear power seems to be a good option to replace fossil fuels, since the fission process does not emit any CO_2 and thus provides an ideal energy source from the global warming point of view. Nuclear reactors, however, imply several other negative issues, among which the fact that uranium itself is a finite resource and cannot represent a long-term solution to the energy question, as showed by its price trend (see Figure 1.2).

Presently, there are 441 operating fission power plants in the world, with an average age of more than 20 years (Figure 1.7). In the next few years, this number will likely decrease because, while waiting for new planning and regulation clearance, the 26 plants that are now under construction will hardly replace the oldest reactors close to decommissioning (Figure 1.8) [7]. The development of fission nuclear energy faces a number of difficulties, such as the relatively long construction period, equal to ~10 years, and the large capital costs needed to build new power plants. In 2007 Moody's Investors Service released conservative estimates of between $5.000 and $6.000/Kilowatt-electric (kWe) for final or "all-in" cost of installing new nuclear capacity, equivalent to 7 billion dollars for a new third generation AP1000 reactor, producing a net 1154 MWe [8]. The recent liberalization of the electricity market in many countries has made the economics of nuclear power generation even less attractive than before, when a monopolistic provider could guarantee output requirements decades into the future [9].

Both cost and time corrections during the construction of power plants are not unusual, due to the very complex technical solutions and the required long bureaucratic procedures to provide the adequate safety of the entire structures. As an example, both the innovative European Pressurized Reactor (EPR) that are being built

in Finland and France have been delayed at least three years and the overall costs increased by 50% compared to the original budget.

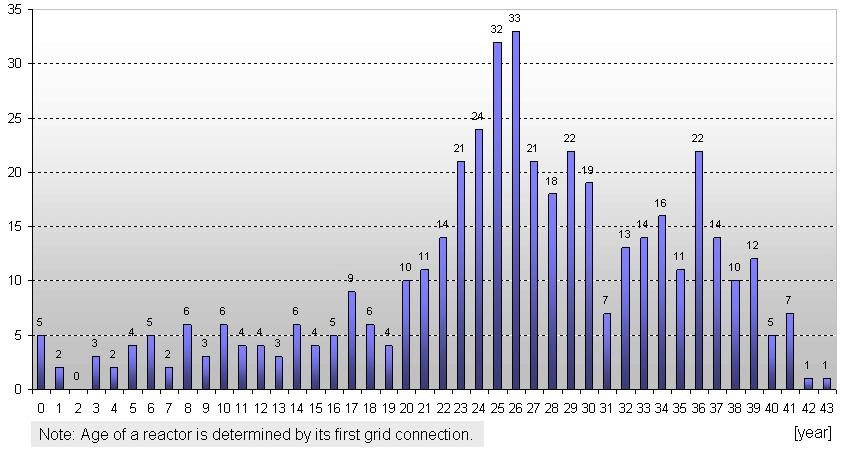

Figure 1.7: Number of operating nuclear reactors by age (Source: International Atomic Energy Agency, 2000).

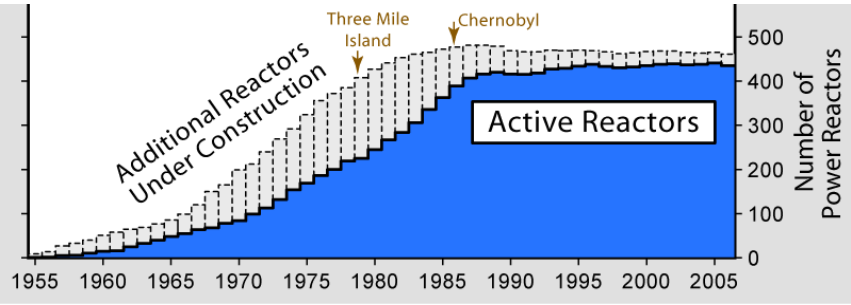

Figure 1.8: Nuclear power reactors in the world (Source: International Atomic Energy Agency, 2006).

Even if, in principle, modern reactors are safe, one of the reasons why few nuclear power plants have been built worldwide in recent years, is the concern of the society about health and safety, due to the 1979 accident at Three Mile Island and the 1986

Chernobyl disaster, whose terrible material and psychological consequences are still difficult to evaluate.

In addition to the above arguments, the main and still not solved problem of nuclear energy is the safe disposal of nuclear waste. "Low level nuclear waste", that includes material used to handle the highly radioactive parts of nuclear reactors (i.e. cooling water pipes and radiation suits) and waste from medical procedures involving radioactive treatments or x-rays, is comparatively easy to dispose of, since the level of radioactivity and the half life of the radioactive isotopes is relatively small. Then, it is sufficient to store the waste in appropriate holders, for a period of 10 to 50 years.

"High level radioactive waste", on the other hand, is generally material from the core of the nuclear reactor or nuclear weapon, such as uranium, plutonium, and other highly radioactive elements made during fission. Most of the radioactive isotopes in this case emit large amounts of radiation and have extremely long half-lives (some longer than 100.000 years), creating long time periods before the waste settles to safe levels of radioactivity. For these reasons, high-level radioactive waste is stored, at first, in spent fuel pools and in dry cask storage facilities in order to significantly reduce the radioactivity (that decays in an exponential fashion), and then, in special "long term" sites, in which the security of the radioactive waste must be assured over geologic time periods. This means that the waste must not be allowed to escape to the outside environment by any foreseeable accident, malevolent action, or geological activity. Areas currently being evaluated for this purpose are space, under the sea bed, and large stable geologic formations on land. The latter seem to be the more suitable solutions, but until now no long term site is operating. The Yucca Mountain Repository is the United States' designated deep geological repository storage facility, located between the Mojave Desert and the Great Basin Deserts in the U.S. State of Nevada. Although the location has been highly contested by environmentalists and residents, it was approved in 2002 by the United States Congress, after 20 years of

debate on the feasibility and safety of the facility [10]. In 2009 the Obama Administration stated that the site was no longer an option and proposed to eliminate all funding in the 2009 United States federal budget, after that some $13.5 billion had already been spent on the project. The total estimated cost was equal to $96.2 billion [11].

Fusion is another nuclear process that, in principle, could provide essentially limitless power, but is still at the level of preliminary laboratory experiments (except for bombs). The most technically advanced nations, such as the European Union, India, Japan, China, Russia, South Korea, and the USA, have recently joined to launch a project, called ITER (International Thermonuclear Experimental Reactor), that should demonstrate by 2038 the possibility to use nuclear fusion for civil purposes. The prototype plant would use as fuel a mixture of deuterium and tritium that fuse in a very high temperature plasma (~200 million degrees Celsius), confined by using superconducting niobium-tin solenoids that generate high magnetic fields above 13 Tesla. Indeed, it's difficult to forecast whether this futuristic project, which is extremely complex and very expensive (about 10 billion €), will be successful [12].

1.3 Renewable sources

Considering all the issues related to fossil and nuclear energy sources, the only available solution to the energy crisis is represented by the large employment of renewable energy sources, assisted by global energy conservation policies.

Energy saving, in fact, plays a key role in this challenge; it would not make sense to face the complex energy question without limiting the several wastes that characterize our lifestyle. Moreover, it has been demonstrated that the quality of life is highly correlated with energy consumption only during basic economic development, while it's almost uncorrelated in industrialized countries [13]. Over a definite threshold, additional energy input can be counterproductive, involving over-consumption of food, road traffic jams, waste production, and, from a social point of view, increase of inequality [14]. Affluent countries could cut their energy consumption by 25% at virtually no sacrifices at all for the population, but this policy would not fit well with the dogma of present-day consumerist society [15].

Renewable energy sources use natural inexhaustible resources with no, or minor, harmful side effects for the environment. Wind energy, energy from water (hydroelectricity), biomass, geothermal and solar energy are the most renowned examples (Figure 1.9). All these sources are abundant and can be exploited all over the world by a variety of technologies, some very simple, some still relatively expensive. Renewable energy sources do not pollute the eco-system nor cause fearing big accidents and, unlike nuclear plants waste products, cannot be used for military offensive. Most of them, especially solar energy, are diluted and diffused form of energy that are vital for the development of rural regions without an electrical grid. The number of rural households served by renewable energy is difficult to estimate, but runs into the tens of millions considering all forms of renewables. More than 30 million households get lighting and cooking from biogas made in household-scale

digesters and an estimated 3 million households get power from small solar photovoltaic (PV) systems [16].

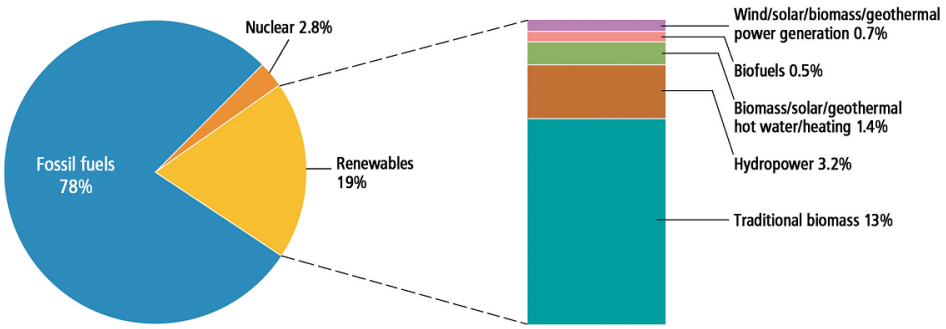

Figure 1.9: 2008 renewable energy share (Source: REN21, 2010).

As the cost of ordinary fuel is increasing, renewables are getting cheaper. Different reasons contribute to this price trend. First of all, while fossil fuel technologies are mature and well known, renewable technologies are rapidly evolving. In this way, innovation and scientific research permit to constantly increase the efficiency of energy conversion, leading to a competitive €/kW ratio. Moreover, once the renewable plants have been built, the fuel is limitless, unrelated to the market fluctuations and free, forever. Once the world makes a clear commitment to shifting towards renewable energy, the large-scale production will itself dramatically reduce the cost of the devices, triggering a real economic boom [17].

Some renewable source would already be economically competitive with traditional technologies, if the hidden costs of energy ("externalities") were included in energy accounting. Externalities deal with short- and long-term negative impacts related to discovery, extraction, distribution and conversion of power resources. Some examples are health damage arising from air pollution exposure, nuclear waste "disposal", huge military costs related to securing energy supply (Persian Gulf War I cost approximately

$80 billion) or safeguard key energy corridors and facilities (pipelines, sea routes, refiner-ies, etc.), the impact of environmental disasters both on human and eco-system. Probably the heavier externality that industrialized countries are inflicting to all the citizens of the world is the forcing of carbon cycle, due to CO_2 emissions, that leads to global warming and therefore to an increase of extreme weather events [14]. The European Union (EU) has recently estimated the extra-cost of electricity production by different sources. For example, electricity generated by coal in Germany implies an extra cost of 0.75€ cents per kWh, that is, 10-times higher than wind energy (Table 1.1) [18].

Table 1.1
Quantified marginal external costs of electricity production in Germany, in €/kWh (Source: European Commission, 2003).

	Coal	Lignite	Gas	Nuclear	PV	Wind	Hydro
Damage costs							
Noise	0	0	0	0	0	0.005	0
Health	0.73	0.99	0.34	0.17	0.45	0.072	0.051
Material	0.015	0.020	0.007	0.002	0.012	0.002	0.001
Crops	0	0	0	0.0008	0	0.0007	0.0002
Total	0.75	1.01	0.35	0.17	0.46	0.08	0.05
Avoidance costs							
Ecosystems	0.20	0.78	0.04	0.05	0.04	0.04	0.03
Global Warming	1.60	2.00	0.73	0.03	0.33	0.04	0.03

Europe, since the last years, has proved to be the most conscious continent towards the energy question, promoting the use of renewable sources as an effective solution. This decision (behavior) is quite mandatory in order to gain the desired energy independence, since EU regions enjoy the highest quality of life but are the poorest as far as conventional energy reserves are concerned. The main European reserves of oil, natural gas and carbon, respectively placed in the North Sea, Norway and between Germany and Poland, do not exceed the 2% of global capacity. Not even nuclear

energy represents an effective alternative for the energy independence of our continent, since not a single country is listed among uranium and torium reserve holders [14]. Germany is leading this "green policy", getting to be the world's first major renewable-energy economy. The share of electricity from renewable sources has increased from 6.3% in 2000 to about 16.1% in 2009, thanks to a huge investment of €9 billions. At present, an estimated 214,000 people work in renewable energy in Germany.

The European Union (EU) has recently consolidated its involvement in fossil fuel replacement by approving on April 2009 the so-called "20/20/20 Renewable Energy Directive", that sets national targets for renewable energy for the 27 EU countries, adding up to a 20% EU-average renewable-energy target for 2020. By the same year, the directive sets also a 20% reduction both of CO_2 emissions and energy consumption with respect to 1990 levels and current forecasts respectively. This represents the strongest international action of this kind, concerning more than 500 million people.

Changes in renewable energy market, industry and policies have been so rapid in the last years that perceptions of the status of renewable energy can lag years behind the reality. During the five-years from the end of 2004 through 2009, worldwide renewable energy capacity grew at rates of 10–60 percent annually for many technologies. For wind power and many other renewable technologies, growth accelerated in 2009 relative to the previous four years. More wind power capacity was added during 2009 than any other renewable technology (Figure 1.10a). However, grid-connected PV increased the fastest of all renewable technologies, with a 60-percent annual average growth rate for the five-year period (Figure 1.10b) [16].

Photovoltaic is, in fact, one of the most interesting renewable technologies, since it's the only that let to convert solar energy directly into electricity, without the use of any moving parts.

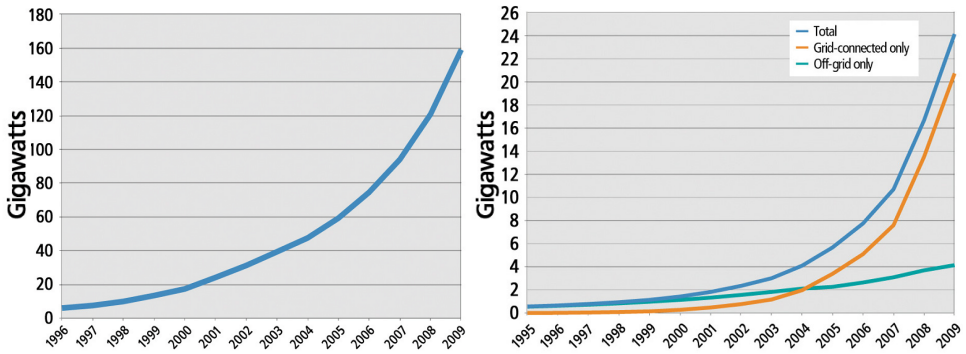

Figure 1.10: a) Cumulative world wind power and (b) cumulative world solar PV power (Source: REN21, 2010).

1.4 Actual PV situation, grid parity and Italian PV market

2010 was a real turning point for the explosion of PV market, thanks to a sharp drop in the production cost of PV modules caused by three main events [19]. The first two were the global financial crisis (triggered by the Lehman Shock in fall 2008) and the collapse of PV market in Spain (revealed to be too optimistic), which led to a large overproduction of silicon for PV applications. The third event was the collapse of the existing price structure for photovoltaic cells by First Solar, Inc. of the US: the company exploded into the market, fuelled by the power of CdTe solar cells with extremely low manufacturing costs, equal to $0.85/W, which was no more than 40% of the manufacturing cost of other solar cell technologies. Most competing major solar cell manufacturers made public commitments to drop their manufacturing costs to the same level as First Solar by the end of 2010. This competition mechanism, together with Si oversupply, led to the drop in solar cell manufacturing cost shown in Figure 1.11, where the 2-3 year old forecasts are moved up to 5-10 years.

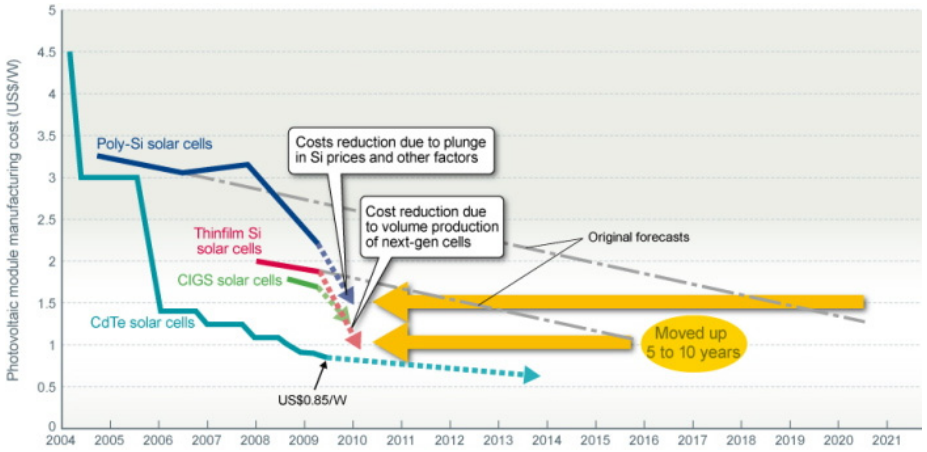

Figure 1.11: Solar cell manufacturing cost vs time. The diagram shows the trend in the manufacturing cost for photovoltaic cell modules. The low cost of CdTe solar cells overpowered other technologies in 2009, but it looks like thin-film Si solar cells may drop to about that level in late 2010 (Source: Nikkei Electronics Asia, April 2010 [19]).

This favourable situation is not thought to be just a passing phase. Photovoltaic is, in fact, the most growing alternative energy source, also in future projections, as shown in Table 1.2, which reports the expected annual growth rates of electricity produced from renewable sources, for the 27 member states of European Union [20].

Table 1.2
Renewable electricity installed capacity projections for the 27 member states of European Union (Source: European Energy Policy Commission, 2009 [20]).

Type of energy	2006	Annual growth 2002-2006	2010 (projection)	Annual growth 2006-2010	2020 (projection)	Annual growth 2006-10
Hydro	106 GW	0.2 %	111 GW	1.1%	120 GW	0.8 %
Wind	47.7 GW	19.9 %	80 GW	13.8 %	180 GW	8.5 %
Photovoltaic	**3.2 GW_p**	**73.9 %**	**18 GW_p**	**54 %**	**150 GW_p**	**23.6 %**
Biomass	22.3 GW_e	21.9 %	30 GW_e	7.7 %	50 GW_e	5.2 %

A fundamental concept for the expansion of the PV market, in particular for the Italian situation, is the concept of grid parity, which represents the point at which alternative means of generating electricity equal the cost of grid power. In Figure 1.12, where the home-use electricity rates vs annual generation per 1 kW_p panel are reported, is evident that Italy enjoys high insulation and high commercial power cost. These two effects together make our country very close to the achievement of grid parity, which, in the opinion of some analysts [21], has been already achieved by the southern regions.

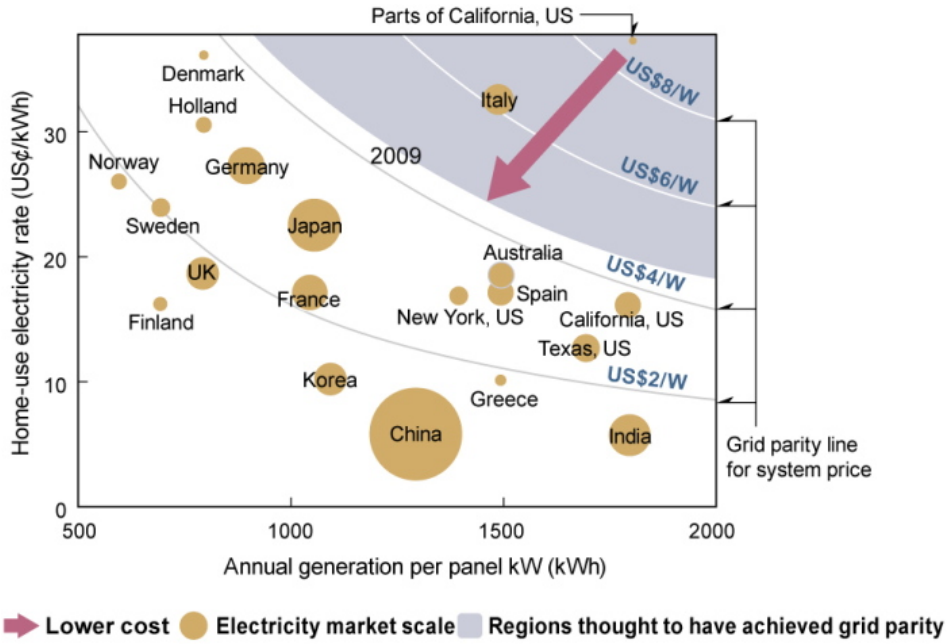

Figure 1.12: Home-use electricity rates vs annual generation per panel kW for various nations and regions. If solar cell system price (inversely proportional curve) drops, more regions will reach grid parity (Source: Nikkei Electronics Asia, April 2010 [19]).

In Italy, after a long period during which PV market was virtually nonexistent, since about 2007 residents and local governments began cooperative investment into a number of solar power enterprises. The recent launch of the feed-in tariff system, making it possible to sell electricity from renewable energy sources at high rates, resulted in a sharp jump in installed solar cells of 45x in only three years, to a total of about 1.6 GW in October 2010.

Many photovoltaic cell manufacturers are eager to get into Italy. Sharp, for example, is involved in a plan with STMicroelectronics and Enel Green Power to construct a solar cell factory in Italy to enter the power generation business. In November 2009, Mitsubishi Electric Corp. of Japan announced that it had delivered a 2.9 MW solar cell module system for use on the roof of an Italian cooperative, making it the largest-scale installation the firm has been involved in. SunPower Corp. of the US, known for solar cell modules with high conversion efficiencies, announced in December 2009 that it had completed the first phase of the world's largest solar power generating plant in Italy, with an output of 85 MW.

References

[1] Key world energy statistics, International Energy Agency, (2010)

[2] M.K. Hubbert, Nuclear energy and the fossil fuels, in American Petroleum Institute Spring Meeting: San Antonio, Texas, p. 40. (1956)

[3] R.A. Kerr, Science **311**, 1698 –1701 (2006)

[4] A. Gabbard, Oakridge National Laboratory Review (ORNL) - Summer/Fall **26**, n.3-4 (1993)

[5] M. Wild "Exponentially on purpose: a century-and-a-half of ignored warnings" – Published by Peak Generation on Fri, 09/03/2010 (http://peakgeneration.blogspot.com/2010/09/exponentially-on-purpose-century-and.html)

[6] Peak Oil. Sicherheitspolitische Implikationen knapper Ressourcen, Future Analysis Department of Bundeswehr Transformation Center, August 2010

[7] M. Inman, Science **309**, 1170–1171 (2005)

[8] "How much?", published by Nuclear Engineering International. 20/11/2007 (http://www.neimagazine.com/story.asp?storyCode=2047917)

[9] F.A. Roques, W.J. Nuttall, D.M. Newbery, "Using Probabilistic Analysis to Value Power Generation Investments under Uncertainty". University of Cambridge. July 2006 (http://web.archive.org/web/20070929150044/http://www.electricitypolicy.org.uk/pubs/wp/eprg0619.pdf)

[10] "Nuclear Waste Policy Act, as amended". Office of Civilian Radioactive Waste Management (OCRWM), U.S. Department of Energy. March 2004. (http://web.archive.org/web/20080514020437/http://www.ocrwm.doe.gov/documents/nwpa/css/nwpa.htm)

[11] "Inflation Hits Yucca Mountain Nuclear Waste Dump", Environment News Service (ENS) (2008)

[12] W.E. Parkins, Science **311**, 1380 (2006)

[13] V. Smil, Energy, Oneworld, Oxford, (2006)

[14] N. Armaroli, V. Balzani, Angew. Chem. Int. Ed. **46** , 52-66 (2007)

[15] V. Smil, Energy at the Crossroads, MIT Press, Cambridge, MA, (2003)

[16] "Renewables 2010 – global status report", REN21- Renewable Energy Policy Network for the 21st Century, (2010)

[17] A. Gore. "Our Choice", Bloomsbury, p. 58 (2009)

[18] European Commission, External Costs (2003) (www.externe.info/externpr.pdf)

[19] T. Nozawa, "Photovoltaic Cells on the Verge of Explosive Growth" Nikkei Electronics Asia - April 2010 (http://techon.nikkeibp.co.jp/article/HONSHI/20100326/181377/?P=1)

[20] "Renewable Energy Technology Roadmap", European Renewable Energy Council, 2009 (http://www.erec.org/fileadmin/erec_docs/Documents/Publications/Renewable_Energy_Technology_Roadmap.pdf)

[21] Marco Magrini, "Il sole 24 ore", June 2009 (http://www.ilsole24ore.com/art/SoleOnLine4/dossier/Economia%20e%20Lavoro/risparmio-energetico/frontiere/grid-party-in-sicilia.shtml?uuid=b581f834-567e-11de-8641-7073d85a2f75&DocRulesView=Libero)

Chapter 2

The physics of solar cells

2.1 Introduction

Solar cells are devices that absorb a part of the light radiation and convert it into electricity, more or less efficiently. In the history, the most suitable materials for this purpose proved to be semiconductors, in their basic architecture, the p-n junction.

A simple conventional solar cell structure is depicted in Figure 2.1 and consists in an active part, made by semiconductor materials, coated with an anti-reflective layer and enclosed by two metal contacts. The front grid-contact is peculiar, since it allows light to fall on the active material.

When incident photons with energy greater than the band gap of the material are absorbed, electron-hole pairs are generated by optical excitation in the semiconductor. This free carrier generation wouldn't be useful without the charge separation induced by the internal electric field present at the junction, which drifts the free electrons and holes towards the n- and p-material respectively (Figure 2.2). If the charge carriers reach the contacts placed at the extremes of the junction before recombining, a current I is generated in the external circuit. In short-circuit conditions this current is called short-circuit current I_{SC}. At the same time, the separation of the charges sets up

a forward potential difference between the two ends of the device, which under open-circuit conditions is called open-circuit voltage, V_{OC}.

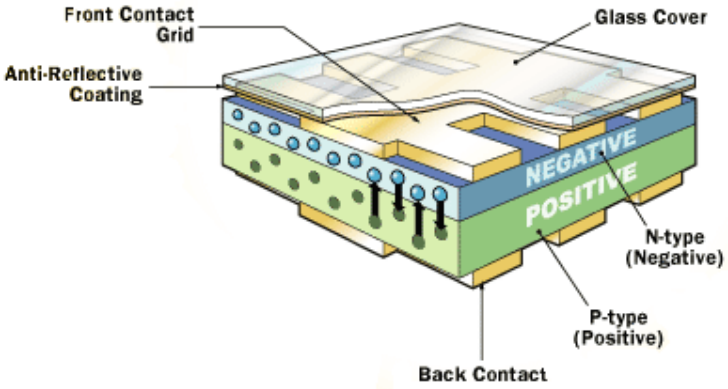

Figure 2.1: Solar cell structure.

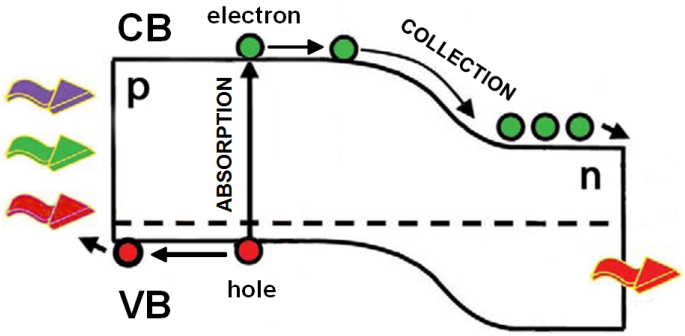

Figure 2.2: Band structure of a p-n junction solar cell with the two main processes needed for the generation of the photocurrent: light absorption and carriers collection.

2.2 Solar energy

The amount of energy reaching the surface of the Earth every hour is greater than the amount of energy used by the Earth's population over an entire year.
While the solar radiation incident on the Earth's atmosphere is relatively constant, the radiation at the Earth's surface varies widely due to: atmospheric effects (including absorption and scattering), local variations in the atmosphere (such as water vapour, clouds, and pollution), latitude of the location and the season of the year and the time of day. The above effects have several impacts on the solar radiation received at the Earth's surface. These changes include variations in the overall power received, the spectral content of the light and the angle from which light is incident on a surface. In addition, a key change is that the variability of the solar radiation at a particular location increases dramatically. The variability is due to both local effects such as clouds and seasonal variations, as well as other effects such as the length of the day at a particular latitude. Desert regions tend to have lower variations due to local atmospheric phenomena such as clouds. Equatorial regions have low variability between seasons.

2.2.1 Air Mass

The Air Mass is the path length which light takes through the atmosphere normalized to the shortest possible path length (that is, when the sun is directly overhead). The Air Mass quantifies the reduction in the power of light as it passes through the atmosphere and is absorbed by air and dust. The Air Mass is defined as: $AM=1/\cos\theta$, where θ is the angle from the vertical (zenith angle). When the sun is directly overhead, the Air Mass is 1.

The efficiency of a solar cell is sensitive to variations in both the power and the spectrum of the incident light. To facilitate an accurate comparison between solar cells measured at different times and locations, a standard spectrum and power density has been defined for both radiation outside the Earth's atmosphere and at the Earth's surface. The standard spectrum at the Earth's surface is called AM1.5G, (the G stands for global and includes both direct and diffuse radiation) or AM1.5D (which includes direct radiation only). The intensity of AM1.5D radiation can be approximated by reducing the AM0 spectrum, which is equivalent to the spectrum emitted by a 6500 K black body (1353 W/m^2), by the absorption and scattering contributes of atmosphere: AM1.5D is then equal to 768 W/m^2 and AM1.5G to 970 W/m^2 (Figure 2.3 [1]). However, the standard AM1.5G spectrum has been normalized to 1 kW/m^2, due to the convenience of the round number and the fact that there are inherently variations in incident solar radiation. The standard spectrum outside the Earth's atmosphere is called AM0, because at no stage does the light pass through the atmosphere. This spectrum is typically used to predict the expected performance of cells in space.

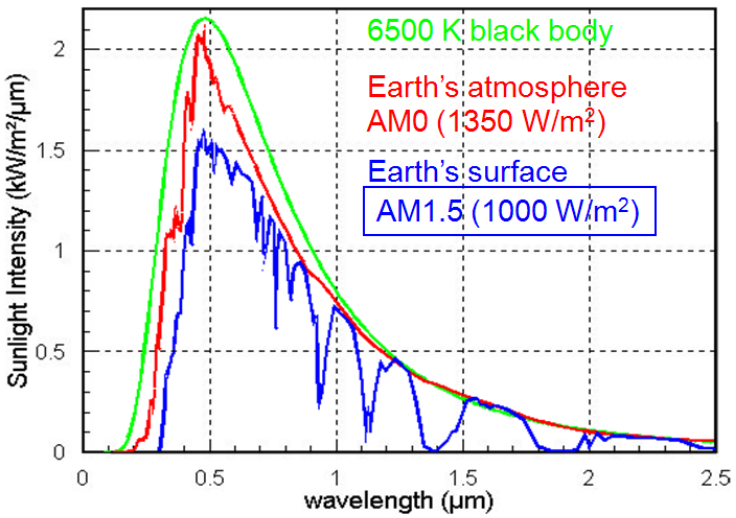

Figure 2.3: Comparison between the spectra of a 6500K black body (green) and the solar radiation outside the Earth's atmosphere (red) and on the Earth's surface (blue) [1].

2.3 Basic operation principles

2.3.1 Ideal I-V characteristic

Electrically, the solar cell is equivalent to a current generator in parallel with a diode (Figure 2.4). When illuminated, the ideal solar cell produces a photocurrent proportional to the light intensity. That photocurrent is divided between the variable resistance of the diode and the load, in a ratio which depends on the resistance of the load and the level of illumination. For high load resistances, more of the photocurrent flows through the diode, resulting in a higher potential difference between the cell terminals but a smaller current through the load. The diode thus provides the photovoltage [2].

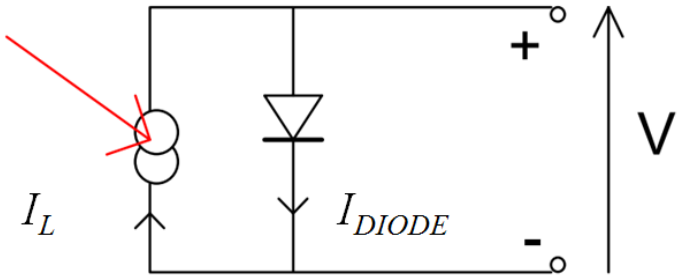

Figure 2.4: Equivalent circuit of ideal solar cell.

The I-V curve of a solar cell is then the superposition of the I-V curve of the diode in the dark with the light-generated current (Figure 2.5). The light has the effect of shifting the I-V curve down into the fourth quadrant where power can be extracted from the diode. Illuminating a cell adds to the normal dark currents in the diode (I_{DIODE}) the light generated current I_L, so that the total current I becomes:

$$I = I_0\left(e^{\frac{qV}{nk_BT}} - 1\right) - I_L = I_{DIODE} - I_L \qquad (2.1)$$

where q is the is the absolute value of the electron charge, n the diode ideality factor (n=1 in the ideal case, 1<n<2 in presence of generation-recombination centres) and k_B the Boltzmann constant.

The dark saturation current I_0 is given by:

$$I_0 = \left(\frac{qD_n n_i^2}{L_n N_A} + \frac{qD_p n_i^2}{L_p N_D} \right) \tag{2.2}$$

Where D_n (D_p) is the electron (hole) diffusion constant, n_i the intrinsic concentration of the material, L_n (L_p) the electron (hole) diffusion length in the p- (n-) region, N_A (N_D) the acceptor (donor) concentration in the p- (n-) region.

From I-V curves it's possible to determine several important parameters that are used to characterize solar cells, such as the short-circuit current (I_{SC}), the open-circuit voltage (V_{OC}) and the fill factor (FF).

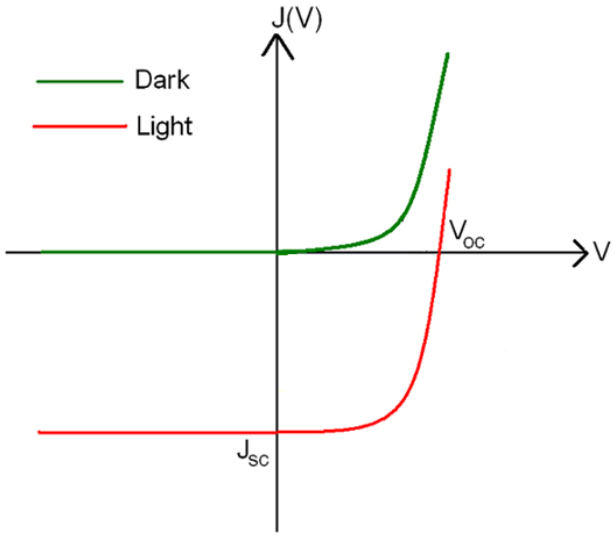

Figure 2.5: Ideal I-V curves for a solar cell in the dark (green) and in the light (red) indicating the short-circuit current I_{SC} and the open-circuit voltage V_{OC}.

2.3.2 Short-circuit current

The short-circuit current I_{SC} is the current through the solar cell when the voltage across the solar cell is zero (i.e., when the solar cell is short circuited). For an ideal solar cell at most moderate resistive loss mechanisms, the short-circuit current is identical to the light-generated current, which is produced by the generation and collection of light-generated carriers.

The collection probability describes the probability that a light generated carrier, absorbed in a certain region of the device, is collected by the p-n junction and therefore contributes to the light-generated current. The probability depends on the distance that a light-generated carrier must travel compared to its diffusion length, and on the surface properties of the device too. The collection probability of carriers generated in the depletion region can be approximated to unity as the electron-hole pair are quickly swept apart by the electric field and then are collected. Away from the junction, the collection probability drops. If the carrier is generated more than a diffusion length away from the junction, then the collection probability of this carrier is quite low. Similarly, if the carrier is generated closer to a region with higher recombination than the junction, such as a surface, then the carrier will recombine. Therefore, the surface passivation and the diffusion length are fundamental for an effective collection.

The collection probability in conjunction with the generation rate in the solar cell determine the light-generated current by the solar cell. The light-generated current is the integration over the entire device thickness of the generation rate at a particular point in the device, multiplied by the collection probability at that point. The equation for the light-generated current density (J_L), with an arbitrary generation rate (G(x))and collection probability (CP(x)), is given by:

$$J_L = p\int_0^W G(x)CP(x)dx = \int_0^W \left[\int \alpha(\lambda)H_0 e^{-\alpha(x)}d\lambda\right]CP(x)dx \qquad (2.3)$$

where W is the thickness of the device, $\alpha(\lambda)$ is the absorption coefficient and H_0 is the number of incident photons per area unit at each wavelength.

A non-uniform collection probability causes a spectral dependence in the light-generated current. For example, at the surfaces, the collection probability is lower than in the bulk. Since the generation rate at different depths in the material varies with the wavelength of the incident light, the high energy part of the solar spectrum, mainly absorbed near the surface, weakly contributes to the light-generated current if the surface or the interface region are characterized by an higher recombination rate in respect to the bulk.

The short-circuit current depends on a number of factors, such as:

- the area of the solar cell. To remove the dependence of the solar cell area, it is more common to refer to the short-circuit current density (J_{SC}, expressed in mA/cm^2);
- the density of photons per unit time (i.e., the power of the incident light). Isc from a solar cell is directly dependent on the light intensity as discussed in Effect of Light Intensity;
- the spectrum of the incident light. For most solar cell measurement, the spectrum is standardised to the AM1.5 spectrum;
- the optical properties (absorption and reflection) of the solar cell (discussed in Optical Losses);
- the collection probability of the solar cell, which depends essentially on the surface passivation and the minority carrier lifetime in the base.

When comparing solar cells of the same material type, the most critical material parameter is the diffusion length and surface passivation. In a cell with perfectly passivated surface and uniform generation, the equation for the short-circuit current can be approximated to:

$$J_{SC} = qG\left(L_n + L_p\right) \tag{2.4}$$

In an ideal device, every photon above the band gap gives one charge carrier in the external circuit, so the short-circuit current increases with decreasing band gap.

2.3.3 Open-circuit voltage

The open-circuit voltage, V_{OC}, is the maximum voltage available from a solar cell, and this occurs at zero current. The open-circuit voltage corresponds to the amount of forward bias on the solar cell due to the bias of the junction with the light-generated current.

An equation for V_{OC} is easily found by setting the net current equal to zero in the solar cell equation (2.1) to give:

$$V_{OC} = \frac{nk_BT}{q}\ln\left(\frac{I_L}{I_0} + 1\right) \tag{2.5}$$

The above equation shows that V_{OC} depends on the saturation current of the solar cell and the light-generated current. While I_L typically has a small variation, the saturation current I_0 may vary by orders of magnitude, because, as shown by equation (2.2), it strongly depends on T, through the n_i^2 factor, and is also influenced by the recombination in the solar cell. Open-circuit voltage is then a measure of the amount of recombination in the device.

The V_{OC} can also be determined from the carrier concentration, as described in Ref. [3]:

$$V_{OC} = \frac{k_BT}{q}\ln\left[\frac{\left(N_A + \Delta n\right)\Delta n}{n_i^2}\right] \tag{2.6}$$

where k_BT/q is the thermal voltage and Δn is the excess carrier concentration. The determination of V_{OC} from the carrier concentration is also termed "Implied V_{OC}".

While the short-circuit current decreases with increasing band gap, the open-circuit voltage increases as the band gap increases. In an ideal device, the V_{OC} is limited by radiative recombination.

2.3.4 Fill factor

The short-circuit current and the open-circuit voltage are the maximum current and voltage respectively from a solar cell. However, at both of these operating points, the power from the solar cell is zero. The fill factor (FF) is a parameter which, in conjunction with V_{OC} and I_{SC}, determines the maximum power from a solar cell.

The FF is defined as the maximum power, given by the product of voltage and current at max power ($V_{mp} \times I_{mp}$), divided by the product of $V_{OC} \times I_{SC}$:

$$FF = \frac{I_{mp} V_{mp}}{I_{SC} V_{OC}} \tag{2.7}$$

Graphically, the FF is a measure of the "squareness" of the I-V characteristic (Figure 2.6). The maximum theoretical FF from a solar cell can be determined by differentiating the power from a solar cell with respect to voltage and finding where this is equal to zero. However, the resulting equation only relates V_{OC} to V_{mp}, and extra equations are needed to find I_{mp} and FF.

A more commonly used expression for the FF can be determined empirically as [4]:

$$FF = \frac{v_{OC} - \ln(v_{OC} + 0.72)}{v_{OC} + 1} \tag{2.8}$$

where v_{oc} is defined as a "normalized V_{OC}", given by $v_{OC} = \frac{q}{nk_BT} V_{OC}$.

The above equations show that to a higher voltage corresponds a higher possible FF. However, large variations in open-circuit voltage within a given material system are relatively uncommon, while the variation in maximum FF can be significant for solar cells made from different materials.

The above equation also demonstrates the importance of the ideality factor n, which is a measure of the junction quality and the type of recombination in a solar cell varying between 1 and 2. A high n-value not only degrades the FF, but, since it also usually signals high recombination, it gives low open-circuit voltages.

A key limitation in the equations described above is that they represent a maximum possible FF, although in practice the FF will be lower due to the presence of parasitic resistive losses, as discussed below.

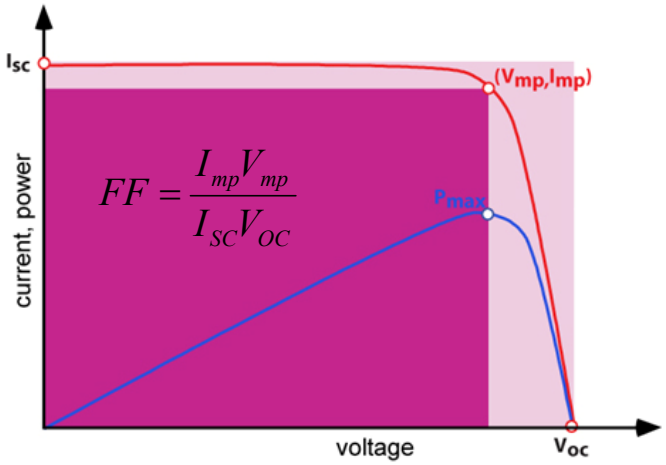

Figure 2.6: Graph of cell output current (red line) and power (blue line) as function of voltage. Also shown are the cell short-circuit current (I_{SC}) and open-circuit voltage (V_{OC}) points, as well as the maximum power point (V_{mp}, I_{mp}). The fill factor (FF) is given by the ratio between the large light rectangle (V_{OC}×I_{SC}) and the smaller dark one (V_{mp}×I_{mp}).

2.3.5 Efficiency

The efficiency is the most commonly used parameter to express the performance of a solar cell. Efficiency is defined as the ratio of energy output from the solar cell to input energy from the sun. In addition to reflecting the performance of the solar cell itself, the efficiency depends on the spectrum and intensity of the incident sunlight and the temperature of the solar cell. Therefore, conditions under which efficiency is measured must be carefully controlled in order to compare the performance of one device to another. Terrestrial solar cells are measured under AM1.5 conditions (more specifically under AM1.5G spectrum) and at a temperature of 25° C. Solar cells intended for space use are measured under AM0 spectrum.

The efficiency of a solar cell is determined as the fraction of incident power which is converted to electricity and is defined as:

$$\eta = \frac{P_{\max}}{P_{in}} = \frac{V_{OC} I_{SC} FF}{P_{in}} \tag{2.9}$$

In terms of conversion efficiency there is an optimum band gap for a solar cell based upon two competing effects: the lower the band gap is, the more low energy photons the cell will absorb and J_{SC} will rise. However, low band gap diodes will have a large dark current due to the n_i^2 dependence of the reverse saturation current, as shown by equation (2.2). This increase in dark current contributes to limit the open circuit voltage, V_{OC}. Higher band-gap cells do not absorb lower energy photons and have a lower J_{SC}, but, on the other hand, have a lower dark current and hence a higher V_{OC}. Since the efficiency is related to the product of J_{SC} and V_{OC}, an optimum band gap may be found, and for AM1.5 is about 1.37 eV, close to that of GaAs (Figure 2.7).

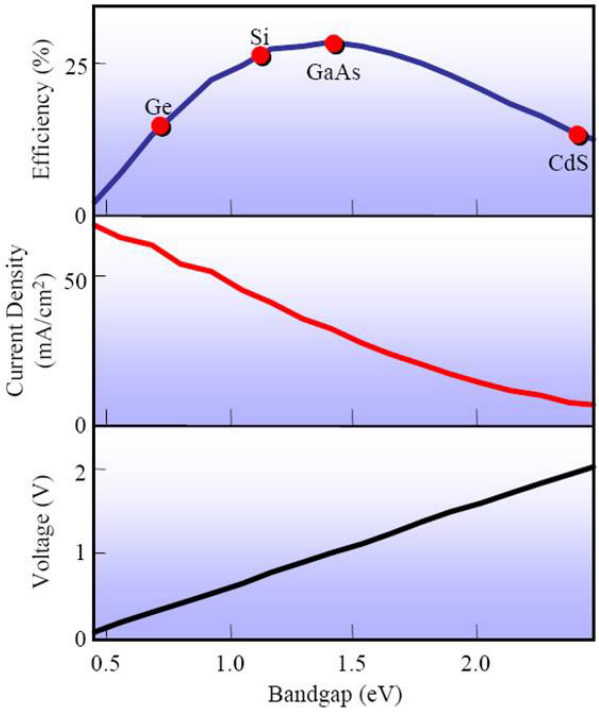

Figure 2.7: V_{OC}, J_{SC} and efficiency as a function of band gap with AM1.5 and T=25° C. Since as the band gap increases, current increases (absorption is enhanced) but voltage decreases (the recombination current is higher), the theoretical efficiency shows a maximum for E_g=1.37 eV.

2.3.6 Effects of parasitic resistances

In real cells power is dissipated through the resistance of the contacts and through leakage currents around the sides of the device. These effects are electrically equivalent to two parasitic resistances in series (R_s) and in parallel (R_{sh}) with the cell (Figure 2.8). For an efficient cell, R_s has to be as small and R_{sh} has to be as large as possible. When parasitic resistances are included, the diode equation (2.1) becomes:

$$I = I_{DIODE} + I_{sh} - I_L = I_0\left[e^{\frac{q(V-IR_s)}{nk_BT}} - 1\right] + \frac{V - IR_s}{R_{sh}} - I_L \qquad (2.10)$$

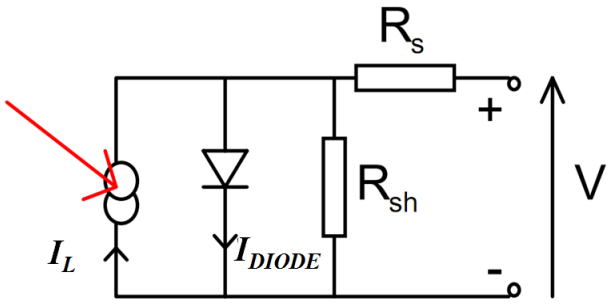

Figure 2.8: Equivalent circuit including series (R_s) and shunt (R_{sh}) resistances.

Series resistance in a solar cell has three causes: firstly, the movement of current through the emitter and the base of the solar cell; secondly, the contact resistance between the metal contact and the semiconductor; and finally the resistance of the top and rear metal contacts. The effect of the series resistance on the I-V curve is shown in Figure 2.9a. The main impact of series resistance is to reduce the fill factor, although excessively high values may also reduce the short-circuit current.

Series resistance does not affect the solar cell at open-circuit voltage since the overall current flow through the solar cell, and therefore through R_S is zero. However, near the open-circuit voltage, the I-V curve is strongly affected by the series

resistance. A straight-forward method of estimating the series resistance from a solar cell is to find the slope of the I-V curve at the open-circuit voltage point. At high current densities, for instance under concentrated light, series resistance is a particular problem and then the optimization of every single aspect of the structure has a great importance for the effectiveness of the device.

Significant power losses caused by the presence of a shunt resistance, R_{sh}, are typically due to manufacturing defects, rather than poor solar cell design. Low shunt resistance causes power losses in solar cells by providing an alternative current path for the light-generated current. Such a diversion reduces the amount of current flowing through the solar cell junction and reduces the voltage across the solar cell. The effect of a shunt resistance is particularly severe at low light levels, since there will be less light-generated current. The loss of current to the shunt resistance therefore has a larger impact in respect to R_S. In addition, at lower voltages, where the effective resistance of the solar cell is high, the impact of a resistance in parallel is large. The effect of R_{SH} on the I-V curve is shown in Figure 2.9b.

An estimation of the shunt resistance value of a solar cell can be determined from the slope of the I-V curve near the short-circuit current point.

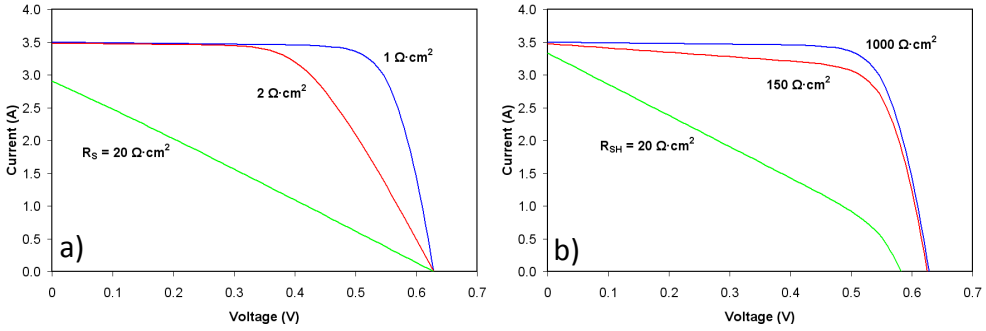

Figure 2.9: Effects of (a) increasing series resistance and (b) reducing parallel resistance on the light I-V characteristics of solar cells.

2.3.7 Two-diode model

Until now recombination loss in the depletion region was excluded, assuming a constant value for the ideality factor n. However, in real solar cells depletion-region recombination represents a substantial loss mechanism. The ideality factor is, in fact, a function of voltage across the device. At high voltage, when the recombination in the device is dominated by the surfaces and the bulk regions, the ideality factor is close to 1. However at lower voltages, recombination in the junction dominates and the ideality factor approaches 2.

For simplicity, a single-level recombination centre is assumed to be located in the depletion region, with a constant recombination rate throughout the space-charge region. The recombination in the depletion region is modelled by adding a second diode in parallel with the first and setting the ideality factor typically to 2 (Figure 2.10).

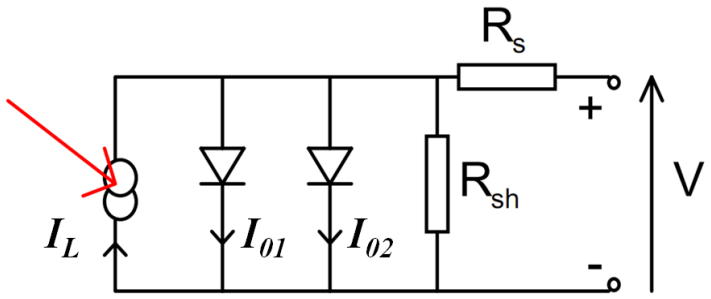

Figure 2.10: Equivalent circuit of a solar cell described by the two-diode model.

The equation of the double diode model under illumination is:

$$I = I_{01}\left[e^{\frac{q(V-IR_s)}{n_1 k_B T}} - 1\right] + I_{02}\left[e^{\frac{q(V-IR_s)}{n_2 k_B T}} - 1\right] + \frac{V - IR_s}{R_{sh}} - I_L \qquad (2.11)$$

Practical measurements of the resulting illuminated equation are difficult as small fluctuations in the light intensity overwhelm the effects of the second diode. Since the double diode equation is used to characterize the diode it is more common to look at the double diode equation in the dark.

As shown in Figure 2.11, the I-V curve can be fitted using the two diodes equivalent circuit. In practice, most measured I-V curves of solar cells can be approximated by several exponential regions in the dark forward I-V characteristic, revealing the presence of several dark current components.

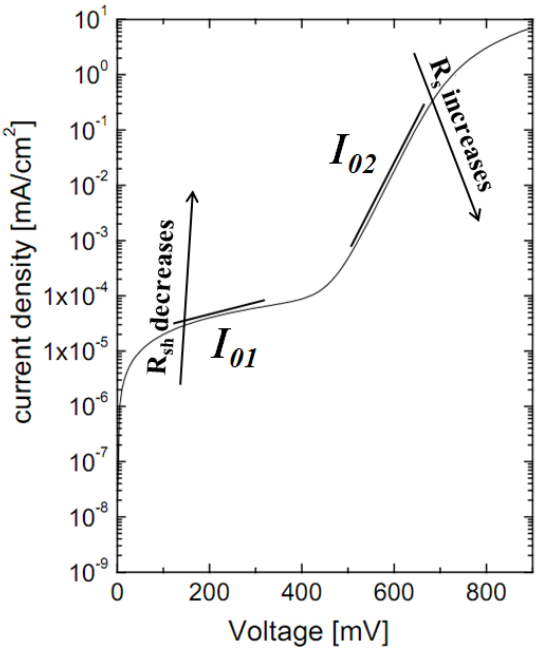

Figure 2.11: Typical dark I-V characteristics of solar cell with an exponential scale. The two slopes of the curve are given by different recombination regimes, described by I_{01} and I_{02}. The effects of R_{sh} and R_s on the low- and high-current density region, respectively, are evidenced.

References

[1] C. Honsberg and S. Bowden (http://www.pveducation.org/pvcdrom)

[2] J. Nelson, The physics of solar cells, London, Imperial College Press, 2003

[3] R. Sinton, A. Cuevas, Appl. Phys. Lett. **69**, 2510-12 (1996)

[4] M.A. Green, Solar Cells **7**, 337-340 (1982)

Chapter 3

Third generation photovoltaics

3.1 History of solar cells

The photovoltaic effect was observed for the first time by French physicist A. E. Becquerel (1820-1891), who noticed that the action of light on a silver platinum electrode, immersed in an appropriate electrolyte, produced an electric current [1]. The first solid state device dates back to 1876: in that year William Adams and Richard Day found that a photocurrent could be produced by selenium, when coated by one heated platinum contact that formed a rectifying junction. In 1894, Charles Fritts, an American inventor, prepared the first real solar cell by coating selenium with an extremely thin layer of gold, which provided both the Schottky barrier, necessary for the charge separation, and the access to the junction for the incident light. For many years, however, it was not the photovoltaic properties of some materials which drew the attention of researchers, but the photoconductivity: since the current produced was proportional to the intensity of the incident light and related to its wavelength, the most interesting applications were photographic light meters. The photovoltaic effect, due to junction barrier, was simply an added benefit, meaning that no power supply was needed. Solar cells for power generation started to be produced only in the 1950s, with the development of good quality semiconductor wafers and of

reliable methods to manufacture p-n junctions, for applications in solid state electronics. The first silicon solar cell was reported in 1954 by Bell Labs researchers Pearson, Chapin, and Fuller with a conversion efficiency of 6%, six times higher than the best previous attempts. The following year Western Electric began to sell commercial licenses for silicon PV technologies but an estimated cost of ~$200 per Watt-peak ($W_p$) made these cells not commercially appealing on a large scale for several decades. Nevertheless, these systems introduced the possibility of power generation in remote locations where fuel could not be easily delivered. The obvious applications were to satellites and space missions where the requirements of reliability and low weight pushed the cost issue of the cell into the background. During the 1950s and 60s silicon solar cells were widely developed for applications in space. In these years other material, such as gallium arsenide, indium phosphide and cadium selenide and telluride, were intensely studied for PV applications since their conversion efficiency resulted to be higher than silicon. However silicon remained, and still now remains, the foremost PV material, benefiting from the advances of the technology for microelectronic industry and from its great abundance in the Earth's crust. In the 1970s the energy crisis experienced by the western oil-dependent world, caused by the Arab-Israel Yom Kippur War of 1973 and the Iranian Revolution of 1979, led to a sudden growth of interest in alternative energy sources, attracting great funding for research and development in those application areas. A large range of strategies for producing photovoltaic devices more cheaply and with improved efficiency were explored. Routes to lower cost included alternative materials such as polycrystalline and amorphous silicon, thin film architectures and organic solar cells. Strategies for higher efficiency included tandem and multiple band gap structures. Although none of these solutions reached the commercial success, a good part of the actual understanding of the PV mechanisms comes from this period. Thanks to the strong increase of oil price, in these years began the establishment of large

photovoltaic companies, such as Solar Power Corporation, Solec International and Solar Technology International, that produced silicon solar cells for terrestrial use. These devices were still not competitive with ordinary energy sources, even if reached a price ten times lower than previously (~\$30/W_p), but were suitable for specific applications, such as stand-alone systems for meteorological stations or installations in rural regions without electrical grid.

During the last decade of the 20th century, the interest in PV expanded, along with the growing awareness of the need to search sources of electricity alternative to fossil fuels. During this period, the economics of PV improved, primarily through economies of scale. In the late 1990s the solar cell production expanded at a rate of 15-20% per year, driving a considerable reduction of cost. PV firstly became competitive in particular contexts, where conventional electricity supply is very expensive, such as in remote low power applications (navigations, telecommunications, rural locations). As prices fall, new markets are opening up.

3.2 Three generations of solar cells

The current PV market consists of a range of technologies, including wafer-based silicon and a variety of thin-film technologies. These technologies, with their possible future options, have been classified into three main generations, where the number of the generations indicate the order in which each became important, from current first generation (1G) to future third generation technologies [2].

Figure 3.1 shows the theoretical maximum efficiency achievable by each PV generation as a function of the production cost projections. Although both the efficiency and the cost values are only approximate, this figure is useful as it presents the respective positions of the PV technologies according to this two parameters.

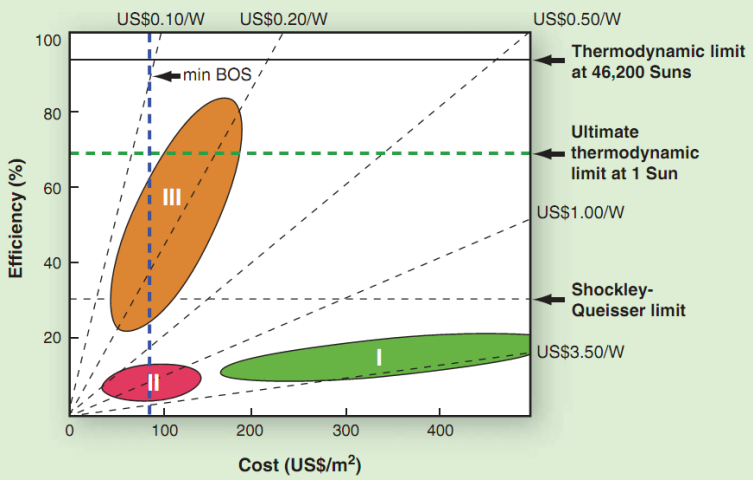

Figure 3.1: Theoretical efficiency of the three PV generation vs the production cost projections. The horizontal lines represent the main theoretical efficiency limits.

In the next page, on the other hand, the real efficiencies of the best research solar cell, from 1975 to 2010, are reported by a very famous graph, edited by the U.S. National Renewable Energy Laboratory (NREL). It is evident that the evolution of the different PV technologies leads to an optimization of the device properties.

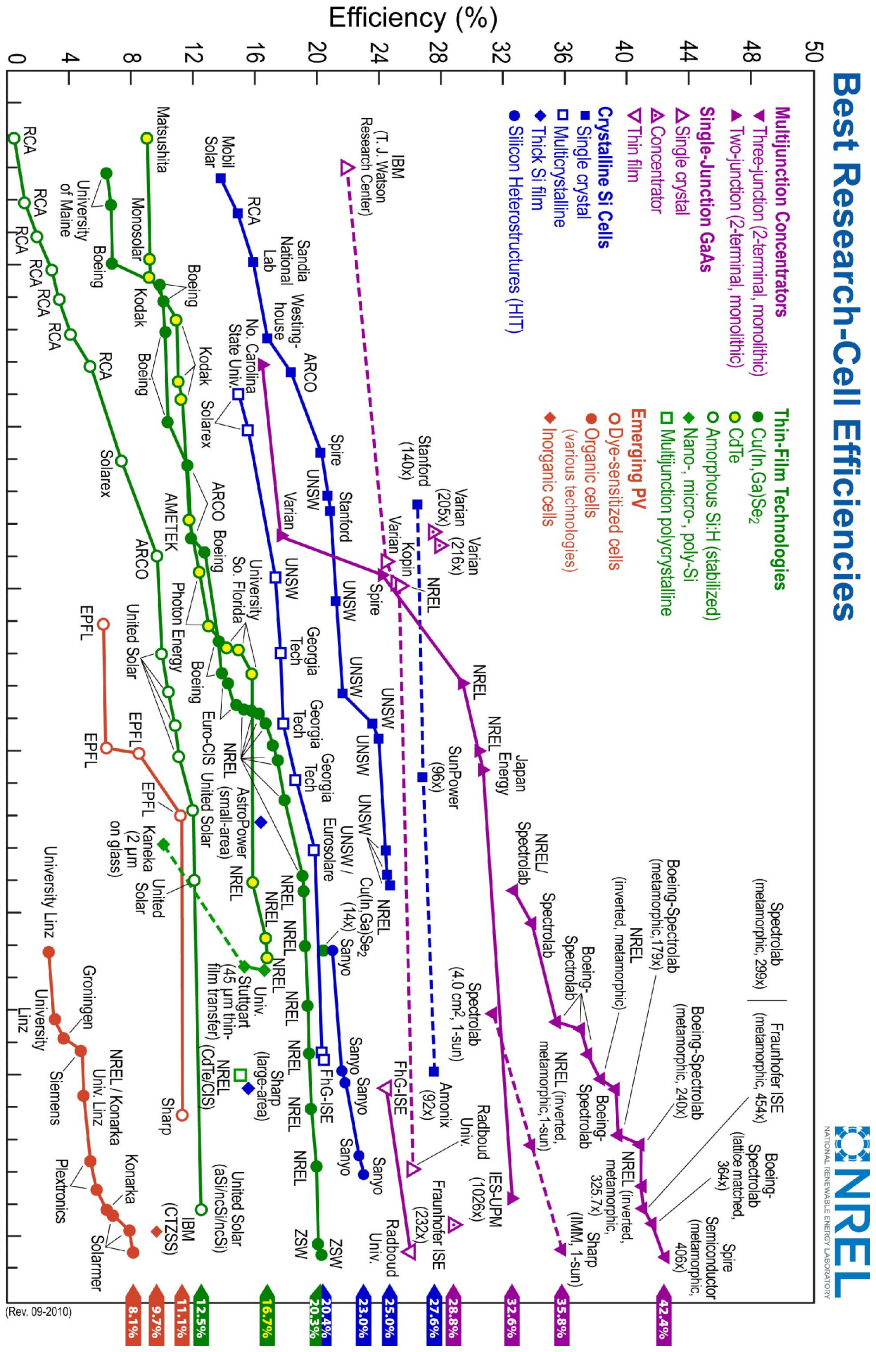

Figure 3.2: Best research solar cell efficiencies achieved in the history. Each symbol corresponds to a different photovoltaic technology (Source: U.S. National Renewable Energy Laboratory, NREL, September 2010).

The first and the second generation of solar cells are briefly described below, since the third one, which is the subject of this chapter, is deeply analyzed in the next paragraphs.

3.2.1 First generation

Current PV mass production is dominated by single-junction solar cells based on silicon wafers, including single-crystal (c-Si) and multi-crystalline silicon (mc-Si), which still represent almost the 90% of the current PV market. This type of single-junction, silicon devices is now commonly known as 1G technology, the majority of which is based on screen-printing-based devices similar to that shown in Figure 3.3.

Originally built using single-crystal wafer silicon (c-Si) and processing technology from the integrated circuit industry, 1G silicon PV benefited greatly from its symbiosis with the semiconductor industry which provided the materials, processing know-how and manufacturing tools necessary to allow a rapid move to large-scale production. The development of new device technologies is pushing commercial single-crystal wafer silicon efficiencies to the 18–21% range, offering the potential for lower $/W as a result of increased efficiencies [3]. The best research silicon solar cell reached a maximum efficiency of 25% [4], showing that commercial devices are already well optimized. Half of the price of 1G PV modules is given by the cost of the 200–250 μm thick silicon wafers. The most part of this thickness is useless in practice, since the majority of solar absorption occurs in the top few tens of microns. So reduction of wafer thickness offers a good cost-reduction potential. Production costs will also be reduced in the coming decade by the continued upscaling of production, by increased production concentration, smarter processing and shorter manufacturing learning curves.

Devices that use alternative silicon sources such as edge-defined film-fed growth [5] and string-ribbon technologies [6] are also offering cheaper wafer-like silicon, grown directly from the silicon-melt, eliminating the wastage inherent in the traditional wafering of c-Si/mc-Si ingots. In spite of much progress, 1G PV costs around 3-4 $/W, and this is still around 4 times too expensive for truly competitive commercial production. It is likely that the cost-reduction trend will reach its limit before 1G PV reaches full cost competitiveness [7].

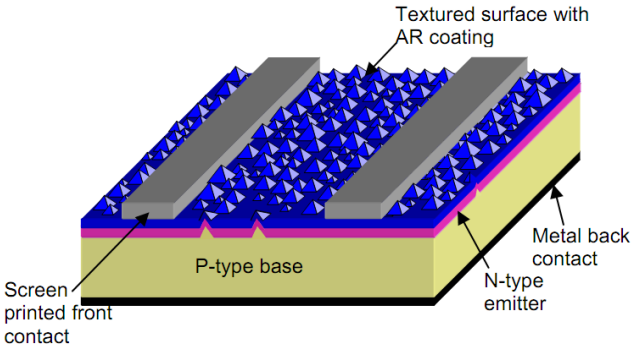

Figure 3.3: Schematic of a typical screen-printed single-crystal solar cell [7].

3.2.2 Second generation

The obvious next step in the evolution of PV and reduced $/W was to remove the unnecessary material from the cost equation by using thin-film devices. 2G technologies are single-junction devices that aim to use less material, while maintaining the efficiencies of 1G PV. 2G solar cells use amorphous-Si (a-Si), $CuIn(Ga)Se_2$ (CIGS), CdTe/CdS) or polycrystalline-Si (p-Si) deposited on low-cost substrates such as glass (Figure 3.4). These technologies work because CdTe, CIGS and a-Si absorb the solar spectrum much more efficiently than c-Si or mc-Si, thanks to a direct band gap, and use only 1-10 μm of active material. Meanwhile, in very

promising work in the last few years, p-Si has been demonstrated to produce ~10% efficient devices using light-trapping schemes to increase the effective thickness of the silicon layer (Figure 3.5) [8, 9].

2G PV offers the potential to cut costs, financial payback and energy payback times compared to 1G, just as long as efficiency and fabrication costs per unit area remain comparable to 1G technologies. Research results from leading laboratories have provided ample evidence of the potential of thin-film photovoltaics, with η=16.7% and η=19.4% for CdTe- and CIGS-based solar cells, respectively [10, 11]. However, these devices have been slow to scale-up. This is partly due to the gap between lab efficiencies (above) and the best module efficiencies of 10.9% for CdTe [12] and 13.5% for CIGS [13], caused by poor material reproducibility and uniformity over large areas [14, 15]. Though perhaps the fundamental issue for CdTe and CIGS technologies is the historical absence of symbiosis with a highly profitable industry. In comparison with silicon-wafer processes, thin-film process tools and production lines are almost exclusively bespoke tools based on in-house and proprietary know-how with correspondingly steep and expensive manufacturing learning curves. While 2G expansion is slower than expected, its potential remains to bring significant $/W cost reduction for PV large-scale production, via reduced materials usage.

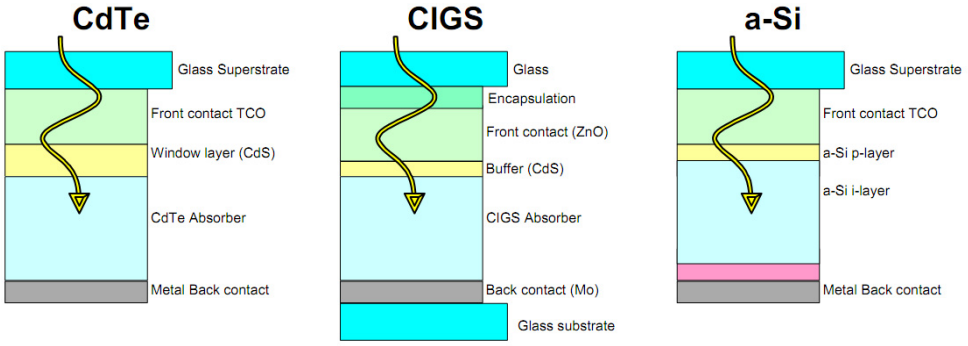

Figure 3.4: Schematic diagrams of thin-film CdTe, CIGS, and a-Si thin-film PV devices [7].

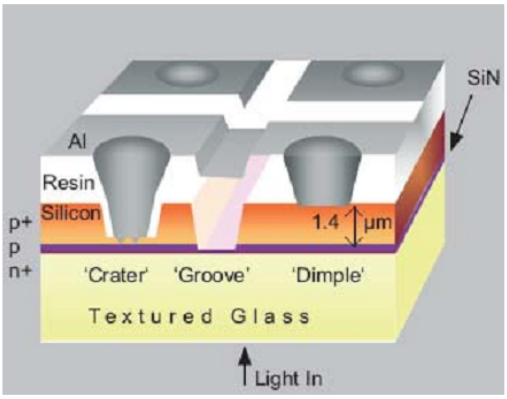

Figure 3.5: Key features of the crystalline silicon on glass (CSG) technology [9].

As 2G technology progressively reduces the active material cost with thinner films, eventually even the low-cost substrate will become the cost limit and higher efficiency will be needed to maintain the $/W cost reduction trend. The possible future is for 3G devices, which should exceed the efficiency limits of single-junction devices and lead to ultra-high efficiency for the same production costs of 1G/2G PV, driving down the $/W [1]. To continue this dissertation it is therefore essential to analyze the main efficiency losses in solar cell which lead to the theoretical efficiency limit.

3.3 Solar cell efficiency limits

3.3.1 Efficiency loss mechanisms

The Carnot efficiency of the sun-earth system puts a theoretical upper limit of 95%. In fact, by applying the second law of thermodynamics to the terrestrial energy conversion of the sun's radiation, the efficiency results:

$$\eta_{Carnot} = 1 - \frac{T_{Earth}}{T_{Sun}} = 1 - \frac{300K}{6000K} = 95\% \tag{3.1}$$

However, the maximum theoretical efficiency of a single band gap photoconverter is only about 33% at earth with AM1.5 spectrum [16]. In the next paragraph the different factors that explain a so low value in respect to the thermodynamic limit are briefly resumed.

Three main efficiency loss mechanisms occur in ideal p-n solar cells (Figure 3.6), which are responsible for this discrepancy with the Carnot efficiency limit:

1) **Absorption losses**: a strong mismatch exists between the broad solar spectrum and the effective absorption by the single band gap of the cell. The solar spectrum can be approximated by the black-body radiation spectrum at T_{Sun}=6000 K. In the ideal case, a single band gap p-n solar cell absorbs all photons with energies hν greater than the band gap (E_g) but is transparent for photons with hν<E_g, whose energy is lost. This mechanism is responsible for an efficiency loss of ~18% on the total value [17].

2) **Thermalization losses**: the photogenerated electron-hole pairs thermalize down to the band-edges, within generally a picoseconds, each giving their excess energy away to phonons [18]. Only then the carriers can be separated, before they recombine, transforming their chemical energy into

electrical energy. So the energy difference ($h\nu_{ph}$–E_g) is unavoidably lost. When thermalization occurs in such a short period of time it is not possible to separate the carriers while they are on a high excitation level. This type of efficiency loss represents the larger contribution to the total value: it reduces by 47% the theoretical maximum efficiency.

3) **Radiative losses**: for the limiting efficiency, an ideal material, without any non-radiative recombination, is considered. However, the carrier-concentration dependent radiative recombination of the photogenerated carriers is always present. This radiative recombination cannot be overcome because it is directly related to the absorption and is another definite loss. This mechanism is responsible only for an efficiency loss of ~2%.

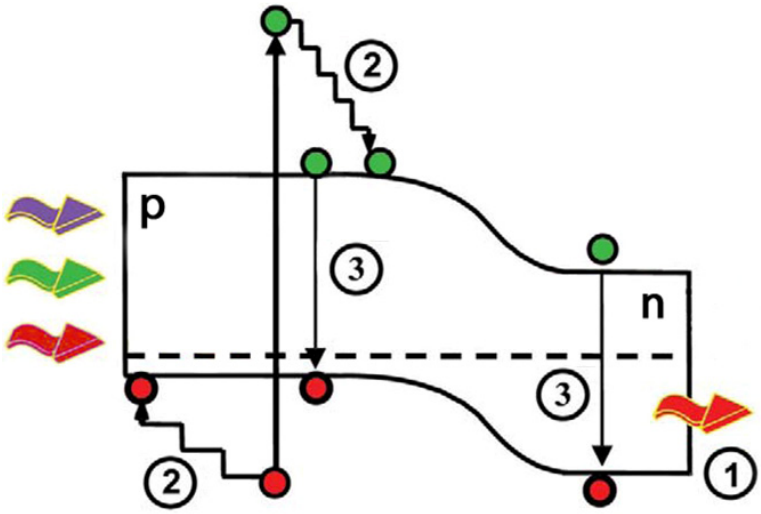

Figure 3.6: Main efficiency loss mechanisms in an ideal p-n solar cell: the transmission of low energy photons ($h\nu_{ph}<E_g$) through the cell gives a 18% efficiency loss (1); rapid thermalization of high energy electron-hole pairs is the main source of efficiency loss, with 47% (2); the loss due to the radiative recombination of photogenerated carriers is only 2%.

3.3.2 Shockley-Queisser efficiency limit (Detailed balance)

In 1961 the notion of the "Detailed Balance Limit" was conceived by W. Shockley and H. Queisser who published a pioneering work on the limit of p-n junction solar cells [19]. Instead of calculating the "theoretical" limiting efficiency using empirical values describing the cells, they based their work on the principle of detailed balance. Basically, the detailed balance theory consists in establishing that the number of electrons extracted from a cell per unit time as a current is equal to the difference between the number of photons absorbed and those emitted from the device. Since the absorbed photons can be related to the photogenerated current of the short-circuited device and the emitted photons to the operating voltage, the current-voltage relationship immediately follows and, from it, the performance properties of the solar cell. So, when the equilibrium is disturbed by absorption of light there will always remain an intrinsic correlation between generation and recombination processes, making it impossible to avoid radiative recombination completely. In calculating the ultimate limit Shockley and Queisser made the following principal assumptions which are still the basis for today's efficiency calculations, except for minor changes with respect to geometry, spectra and concentration:

a) only radiative recombination is taken into account, governed by detailed balance
b) the quasi-Fermi level[1] separation is constant and equal to the external bias
c) the sun and the cell emission spectra are approximated by Planck's blackbody emission spectra at T=6000 K and T=300 K, respectively
d) the absorption is ideal: all and only photons with energy above the band gap are absorbed

[1] Quasi-Fermi level are the new Fermi level that describes the population of each type of charge carrier in a semiconductor when their populations are displaced from equilibrium.

e) each absorbed photon generates exactly one electron-hole pair

f) all geometrical relevant factors (e.g. angle of cell to sun) are ideal.

With those assumptions the photocurrent (PC) and the ideal I-V characteristics of a diode are calculated. An analytical expression is then derived, which gives the cell's efficiency for a given band gap. Maximizing this expression leads to the ultimate limit of 30.5% at a band gap of 1.26 eV with AM0 spectrum (Figure 3.7a).

The Shockley-Queisser limit for a terrestrial AM1.5 spectrum is 33.7% and is shown in figure 3.7b with the best experimental results for single junction devices shown as red dots [20]. The optimum band gap for the AM1.5 spectrum is approximately 1.4 eV, which corresponds closely to the band-gap of 1.42 eV of GaAs.

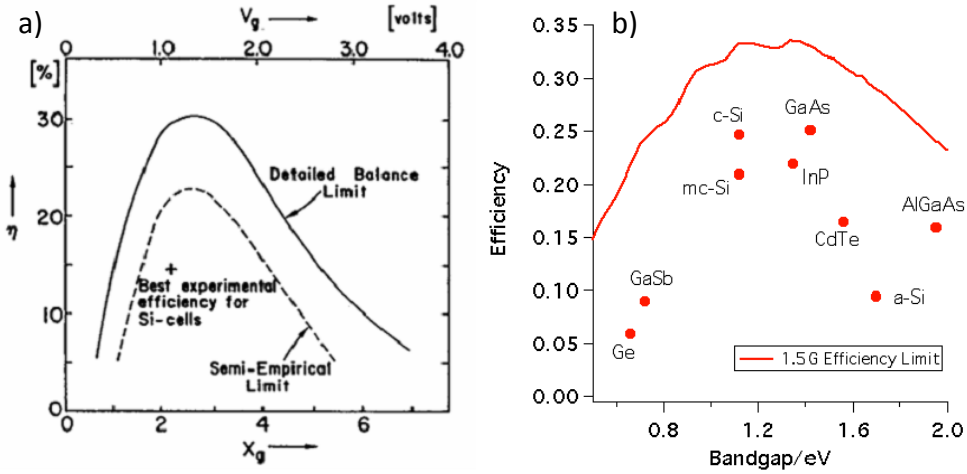

Figure 3.7: (a) The Shockley-Queisser efficiency limit for a single-junction cell published in the original Shockley and Queisser paper in 1961 for an AM0 incident spectrum [19], including the best experimental efficiency for silicon cells in 1961 and a semi-empirical curve thought to be the efficiency limit before the Shockley-Queisser paper was published. $V_g=E_g/q$, $x_g=E_g/k_BT_{Sun}$. (b) The Shockley-Queisser limit with an AM1.5 incident spectrum, with the best experimental results for single junction devices shown as red dots [21].

3.4 Third generation innovative concepts

Third generation photovoltaics takes advantage of many innovative concepts for the development of different solar cell structures modelled to potentially overcome the theoretical efficiency limit of single p-n junction solar cells. The main concepts that are addressed to achieve this purpose are: (i) **multiple band gap structures** (multi-junctions, quantum wells and intermediate bands), (ii) **hot carrier cells** (obtained through multiple exciton generation and selective energy contacts), (iii) the **modification of the incident spectrum** (up- and down-conversion).

Currently, several **alternative solutions**, based on organic and conductive polymer materials, aim at lowering the cost of photovoltaic devices, accepting that lower efficiencies result (Dye-sensitized and organic Solar Cells).

The only approach which is commercially exploited at present are tandem and multi-junction solar cells, but other interesting ideas, reported in the next paragraphs, have been proposed.

3.4.1 Multi-junction solar cells

Multi-junction solar cells are the current efficiency leaders and already have commercial uses, especially in powering satellites [22]. It is expected that these cells can become cost effective for terrestrial uses when combined with solar concentrators [23]. In 2003, a triple junction InGaP/GaAs/Ge cell was demonstrated with 36% efficiency (AM1.5, 100-500× concentration) [24] and since then maximum efficiency of these cells has been raised above 41% [25]. Multi-junction solar cells are able to achieve such high efficiencies by separating the absorption of the polychromatic solar spectrum into semiconductors with different band gaps. In this way, high energy photons are absorbed by the high band gap junction and lower energy photons are

absorbed by the lower band gap. This allows a large portion of the solar spectrum to be absorbed, avoiding thermalization losses from carriers relaxing to the band edges. In theory, an infinite number of junctions can be stacked for 86% efficiency under maximum solar concentration [26]. The development of these multi-junction solar cells started with double-junction cells of GaAs as the lower cell and AlGaAs or InGaP as the top cell [27].

There are two distinct approaches to combining the cells: one method is to physically separate them and use multiple contacts, while the other integrates the cells monolithically by epitaxial growth with tunnel junctions joining them in series. Figure 3.8 highlights the differences between the two approaches.

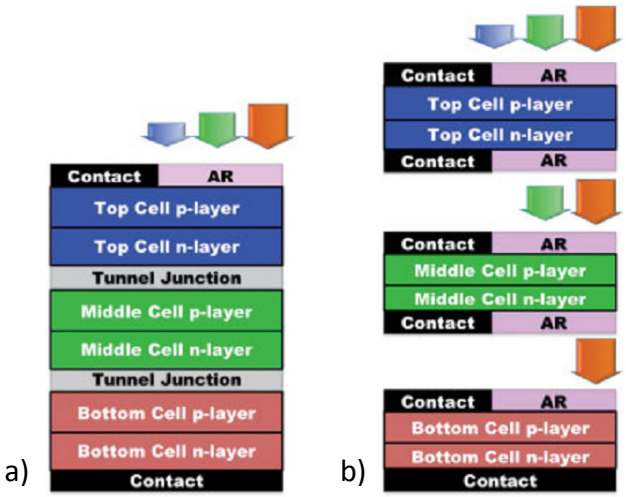

Figure 3.8: (a) Monolithic (two-terminal) multi-junction solar cell: three different band gap cells are connected in series to each other with one contact on the front and one contact on the back. (b) Mechanically stacked (multi-terminal) multi-junction cell, with contacts for each individual cell.

For monolithic multi-junction cell designs, it is important to keep the lattice mismatch between each successive layer to a minimum in order to avoid creating

misfit dislocations during epitaxial growth, which is performed by metal organic vapour phase epitaxy (MOVPE). Dislocations can severely diminish solar cell performance by creating preferential regions for carriers non-radiative recombination. For these reasons, InGaP/GaAs/Ge triple-junction cells have proven to be extremely efficient as all three layers are closely lattice matched, but on the other hand they do not have the optimum arrangement of band gaps to maximize the efficiency.

The efficiency of monolithic multi-junction cells is limited by the fact that they are electrically (as well as optically) connected in series. Therefore, the lowest current-producing subcell fixes the current of the entire cell. In the case of InGaP/GaAs/Ge, the Ge subcell produces excess current that is wasted. Therefore it would be advantageous to have different combinations of band gaps in the three layers. With Ge as the bottom cell, the optimum middle and top band gaps are 1.16 eV and 1.73 eV, respectively. This structure could theoretically achieve efficiencies over 60%, under 500× concentration [28]. These band gaps can be achieved by adding additional indium to the middle and top cells. However, to change the band gap of each layer would require moving away from the lattice matched condition. One solution to this problem comes from growing metamorphic or lattice mismatched layers on top of the Ge substrate with lower band gaps, as to reduce the excess current generated in the Ge subcell [25]. Using this approach, an efficiency of 41.1% was reached under a concentration of 454 suns. Another approach is to remove the bottom Ge subcell and replace it with a wider band gap semiconductor. This has been achieved by growing a lattice matched GaAs/InGaP on top of a GaAs substrate followed by a graded layer of $In_{1-x}Ga_xP$ and finally a layer of $In_{0.3}Ga_{0.7}As$ (Figure 3.9) [29]. The GaAs substrate is then removed and the entire device is inverted so the bottom layer is $In_{0.3}Ga_{0.7}As$. The first advantage of this technique is that the InGaAs layer has a band gap of 1.0 eV, which reduces the excess current generated by the bottom layer and increases the open circuit voltage. Moreover, the inverted growing technique is beneficial as misfit

dislocations are only created in the InGaAs layer while preserving the high quality of the InGaP and GaAs layers, which provide the highest conversion efficiency. Using this technique, an efficiency of 38.9% was achieved at 81 suns concentration.

All of the concepts previously discussed regarding multi-junction cells have assumed the cells are arranged on top of one another and hence are optically connected in series. However, it has been shown that even higher efficiencies can be achieved by splitting the incoming solar energy into separate bands of a narrower spectral distribution (Figure 3.10). In doing this, each band of light can be optimally collected with a different solar cell thereby avoiding thermalization losses [30]. Such a design has many advantages over traditional multi-junction cells, such as that each solar cell does not have to be current matched and hence all the cells can all operate at their optimal efficiency. However, the cost of the spectral splitting structure would likely be very high as each cell would be grown on a separate substrate.

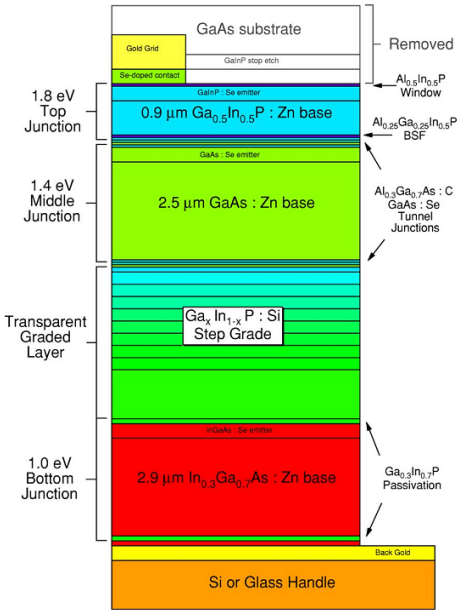

Figure 3.9: Schematic of inverted triple-junction solar cell structure. [29].

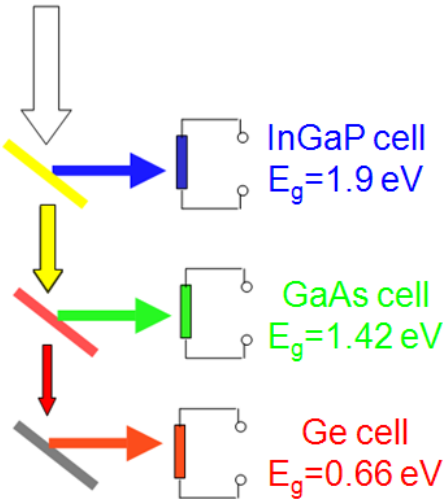

Figure 3.10: Spectrum-splitting solar cells. Three suitable materials are shown.

3.4.2 Quantum well solar cells

Quantum wells (QW) have been studied for several decades for application in electronics and photonics. Their key feature is the confinement of charge carriers in one dimension (1D confinement), creating a sheet of carriers (2D electron gas) with well-defined energy levels owing to modification of the band structure [31]..

The QWs have to be very thin (10-50 times the inter-atomic spacing) to impose quantum confinement on the electrons and holes. The quantum confined levels in decoupled QWs (thick barriers) can be calculated. In the ideal case of a in an infinite one-dimensional well, they are simply given by:

$$E_n = \frac{n^2 \pi^2 \hbar^2}{2mL^2}, \tag{3.2}$$

where m is the carrier effective mass and L is the well width.

The application of epitaxially grown and III-V compound based multiple quantum well (MQW) in photovoltaics, as quantum well solar cells (QWSC), derived from their peculiar electronic properties, which were applied to realize innovative quantum devices such as modulators, amplifiers, photo-detectors, solid-state photomultipliers and so on [32].

Instead of a p-n structure a p-i-n cell needs to be used for accommodating the QWs within the space charge region. A comparison of the electrical properties of two simple (no QWs) p-n and p-i-n diodes have shown that the insertion of an i-region has no effect on the dark current behaviour and sometimes even enlarges slightly the spectral response [33].

As shown in figure 3.11, by incorporating a series of quantum wells into a single p–i–n junction, a multiple ban gap device is created. Here, by virtue of band gap engineering, a careful control of the epitaxial growth parameters permits to properly modulate the number of wells, their depth and width, in order to optimally match the

solar radiation. In fact, the inter subband optical transitions between the quantum confined energy levels let the device to extend its absorption spectral range over the energies of the materials forming the barrier-well sequence.

Once the electron-hole pairs are photogenerated, they are thermally activated over the barrier and escape out from the wells driven by the internal electric field, going to contribute to the photocurrent and/or to the photovoltage. In order to guarantee an effective separation of the photogenerated carriers, it is very important to minimize the background doping of the intrinsic region. Otherwise the electric field profile is modified and the photovoltaic performances deteriorates (Figure 3.12).

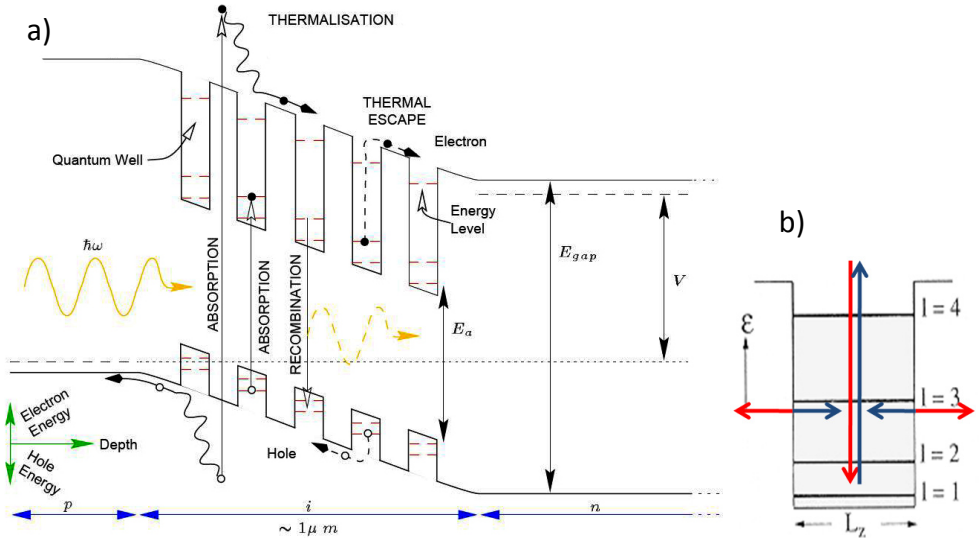

Figure 3.11: Schematic energy band diagram of a QWSC (a), with the detail of the energy shift of electronic quantized levels due to the variations in the well width (b).

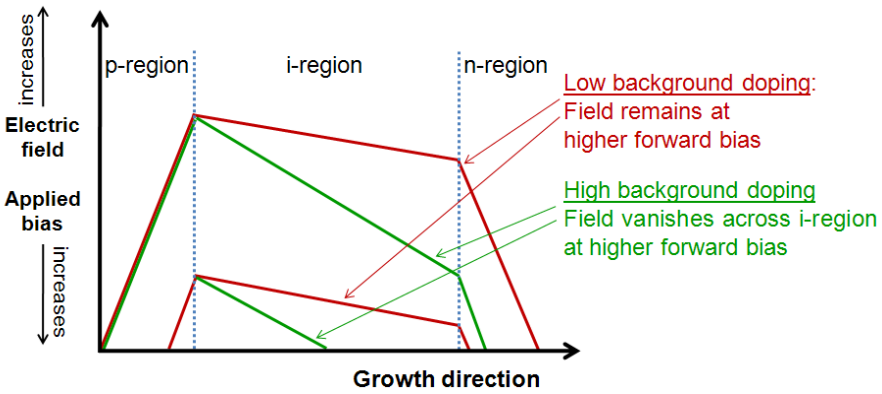

Figure 3.12: Effect of background doping of the i-region on the electric field distribution. If the background doping is too high, when the field is decreased by forward bias, it might cut off, resulting in ineffective carrier collection.

Quantum wells are typically fabricated using metal organic vapour phase epitaxy (MOVPE) or molecular beam epitaxy (MBE). These deposition processes allow precise, atomic level control of the thickness of specific alloy-layer composition. The lattice constants of the barrier and well materials should match reasonably well, even though a certain amount of balanced strain is not necessarily detrimental to the cell performance [34]. However, above a certain critical thickness of the strained material the structure relaxes resulting into a myriad of misfit dislocations, which acts as non-radiative recombination centres. This condition unfortunately restricts the choice of possible material systems (Figure 3.13).

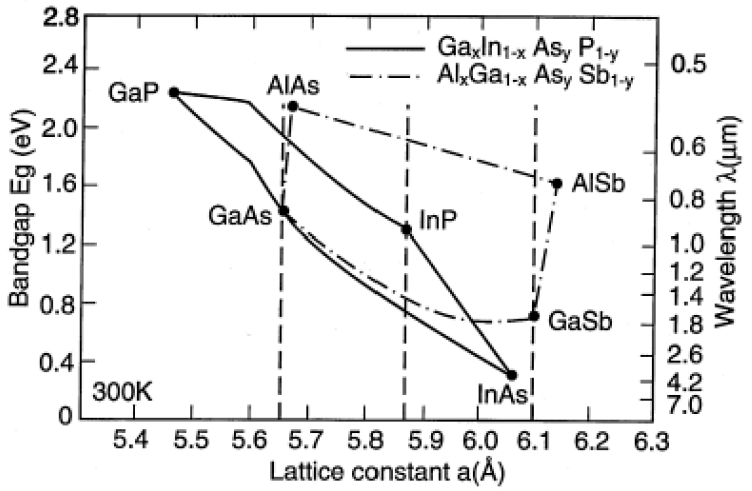

Figure 3.13: Band gap and lattice parameter data for various III-V semiconductors. Vertical lines indicate suitable materials for QWSC applications, thanks to the reduced lattice misfit with GaAs, InP or GaSb.

Owing to the relatively high cost nature of the described processes, it is expected that application of quantum well-based solar cells will be limited to space or concentrator PV systems. Nevertheless, such cells constitute a prototypical quantum confined nanostructured system, and as such are of great fundamental interest.

Barnham and co-workers were among the first to study QWSCs [32]. The reason for a potential increase in efficiency using quantum wells is that absorption in quantum wells is very high due to the carrier density obtained by quantum confinement in the plane of the well. The work by Barnham and co-workers has shown that while it is possible to obtain a short-circuit current density enhancement in such cells, there is often a corresponding reduction in the open-circuit voltage. This is associated with recombination of quantum confined charge carriers as they attempt to traverse the multiple wells, as well as defects (dislocations, etc.) that are typically present within the MQW structure. There is indeed some debate regarding the expected efficiency enhancement in QWSCs, owing to the difficulty in accurately

calculating the increase in absorption as well as the increase in radiative recombination (dark current) in these structures. Some workers have argued that it cannot be expected an enhanced efficiency for QWSCs [35], whereas others have developed detailed recombination models QWSCs [36] and calculated an enhancement of ~20% (relative) for AlGaAs/GaAs QWSCs compared to baseline GaAs cells [37]; the main difference in these approaches are the assumptions on the quasi-Fermi level spatial profile within the quantum wells. In general, when comparing single junction GaAs solar cells with ones containing MQWs, the power conversion efficiency is enhanced at high concentration though it is equal or reduced compared to planar cells under AM1.5 conditions [38]. More recent work has shown, however, that by incorporating a distributed Bragg reflector (DBR) behind the MQW, it is possible to obtain an enhanced V_{OC} compared to a planar control, leading to efficiencies above 26% under 200× concentration [39]. This is due to photon recycling that allows collection of photons that have passed through the structure to be absorbed on multiple passes.

However, regardless of whether these devices can achieve efficiencies surpassing the Shockley-Queisser limit, there is little doubt that they can have practical benefits, such as, for example, by means of band gap engineering in multi-junction solar cells, while maintaining lattice matching conditions. Triple junction cells made of InGaP/GaAs/Ge could be improved by adding InGaAs QWs to the GaAs layer creating a more efficient arrangement of band gaps.

3.4.3 Intermediate-band solar cells

The concept of multiple band gaps is also used in intermediate-band (IB) solar cells, which are an alternative way to improve the overall efficiency of solar cells with only one junction. The basic concept in these cells is that a narrow density of states within the band gap of a semiconductor can allow sub-band gap absorption while

maintaining the same open-circuit voltage of the host matrix. The key is to have three quasi-Fermi levels as shown in Figure 3.14a [40], which give the population of holes in the VB, electrons/holes in the IB and electrons in the CB, respectively. This requirement means that the occupation probability of the intermediate band is not influenced by the occupancy of the CB and VB bands of the host matrix, or, in other words, the intermediate band is decoupled from the other two. Three different absorption processes are then available in such a system: Valence Band (VB)→IB, IB→Conduction Band (CB) and VB→CB.

The first experimental basis for these cells came from introducing impurities into silicon to extend the sub-band gap response and increase efficiencies [41]. However, this approach did not show efficiency improvements and the focus switched to using quantum dots (QDs) to form the intermediate band [42]. Figure 3.14b illustrates the basic concepts of such a structure. The QDs have a lower band gap than the barrier regions and, as a result of quantum confinement, the QDs form discrete energy levels. Due to the periodic arrangement and close proximity of the QDs, the discrete energy levels overlap and form mini-bands allowing for sub-band gap absorption.

One important requirement for the operation of IB solar cells is that the IB Fermi level must reside within the IB. This allows sufficient numbers of electrons in the IB to be promoted into the CB. It is also beneficial to have no overlap in the absorption coefficients between the three transitions. If this is not the case, high energy photons that should transfer electrons between the VB and CB could be absorbed in a VB→IB transition, losing some of the energy in a similar way that a traditional single-junction cell experiences with high frequency radiation.

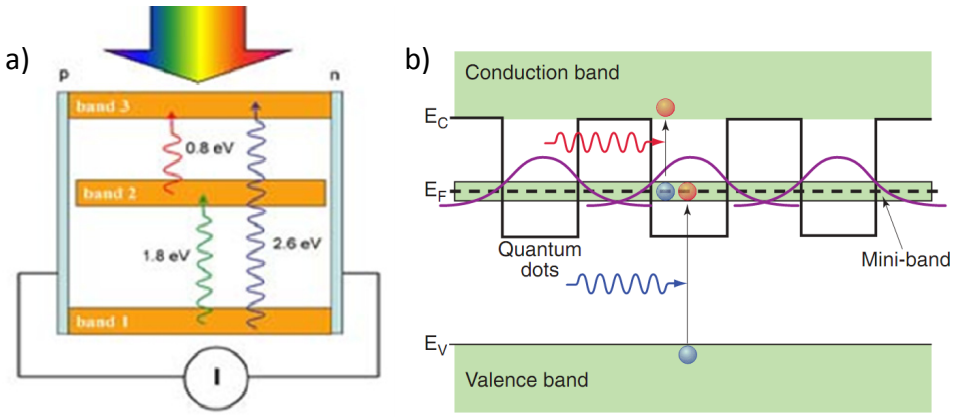

Figure 3.14: (a) Intermediate-band solar cell working principle, with the three different available absorption processes. (b) Intermediate band formation by using quantum confinement effects in quantum dots (QDs).

Test cells have been fabricated using GaAs layers with imbedded InAs QDs [43] and GaSb QDs [44]. In both cases, sub-band gap photo-response has been detected, indicating that the QDs indeed contribute to the photocurrent of the cells. All experimental cells of this kind shown to date exhibit lower overall efficiencies than cells fabricated with no QDs, due to lower open circuit voltages. However, the experiments suggest that it is possible to have three separate quasi-Fermi levels. The open circuit voltage lower than expected is attributed to non-radiative recombination between the CB and VB, suggesting that the current growth techniques introduce defects lowering the efficiency of these cells. The presence of the IB itself does not appear to increase non-radiative recombination: this is a very important result in the aim of increasing the efficiency beyond conventional single-junction cells.

One of the biggest problems with using QDs as IB solar cells is that the QDs are very small and therefore do not absorb much light. Therefore, in order to have enough QDs to significantly improve the photocurrent, it is necessary to have several layers of QDs. Unfortunately, the growth of multiple layers of QDs results in

additional structural damage, which degrades the performance. In one case, for example, it was shown that the expansion from 10 QD layers to 20 and 50 layers resulted in much lower efficiencies, which have been attributed to the creation of threading dislocations from the QDs in the intrinsic region [45]. The origin of these dislocations is the lattice mismatch between the QDs and buffer material. However, the addition of strain compensating layers between each QD layer has been shown to improve performance and even increase the short circuit current of QD IB solar cells above test cells with no QD [46]. Strain compensation layers are able to reduce the density of dislocations by counterbalancing the compressive strain between InAs and GaAs with tensile strain from InAs and GaP. Unfortunately, even in these cells, the efficiency is lower due to a decreased open circuit voltage.

3.4.4 Hot carriers solar cells

Multiple energy levels have shown to increase the efficiency of standard solar cells. However, it is not absolutely necessary to introduce multiple energy levels to go beyond the Shockley-Queisser limit: in 1982 it was recognized that it could be possible to increase solar cell efficiencies for a single junction by utilizing hot carriers [47].

In all solar cells, an incoming photon with energy in excess of the band gap produces an electron-hole pair. The electrons and holes will first interact with other charge carriers through carrier-carrier interactions to form carrier populations that can be described by a Boltzmann distribution. The temperature defining the carrier distribution is, in the very first instants, above the lattice temperature and hence the carriers are referred to as hot carriers. In a typical solar cell, the hot electrons will give off their excess energy to the lattice by producing optical phonons, which interact with other phonons, and the energy in excess is lost. In most bulk semiconductors, all of this happens in less than 0.5 picoseconds.

While at first it seems obvious that preventing carriers from thermalizing would decrease the energy lost, it is not as clear how hot carriers increase efficiencies. There are actually two different possibilities to achieve this aim: multiple exciton generation (MEG) and hot-carrier extraction. Both concepts take advantage of slowed carrier cooling phenomena but in different ways.

Multiple exciton generation (MEG)

Through MEG, the excess energy of the hot electrons is used to create additional excitons, i.e, bound electron-hole pairs. The hot electron must have the energy of at least two times the band gap to create one additional electron-hole pair, as shown in Figure 3.15. This process is explained as impact ionization (which is the opposite of the Auger process) wherein the energy of one photogenerated electron is transferred to another electron.

MEG does occur in bulk semiconductors, but the probability of this event is so low that it does not contribute much to the efficiency of the cells [48]. There are cases where hot carrier lifetimes exceed picosecond, as in many quantum systems. First, multiple-quantum wells were studied and found to have hot carrier lifetimes much larger than bulk values [49]. Hot carrier lifetimes in the hundreds of picoseconds have been observed in multiple-quantum well structures thanks to the confined nature of the QWs, which does not allow optical phonons to equilibrate with the lattice fast enough. But these effects are not typically observed without high photo-carrier densities, which are not easily achievable through sunlight illumination.

Therefore, the attention has shifted to QDs where increased hot carrier lifetimes are expected to exist under all illuminations. In this case, in fact, the electrons are confined in all three dimensions, leading to the formation of discrete energy levels: if the spacing between energy levels is greater than the optical phonon energy, hot electrons cannot thermalize without multiple-phonon processes, which are less likely

than single-phonon processes. There is experimental evidence of slowed cooling in QDs, where hot electrons exhibite lifetimes from a few picoseconds all the way up to nanoseconds [50]. PbSe and PbS QDs have been shown to have quantum yields (electron-hole pairs per photon) above 300% and even above 700% [51]. The effect has been observed in numerous other QDs including InAs [52] and Si [53].

Under AM1.5 spectrum the theoretical efficiency of a MEG-enhanced cell is over 44%. Nevertheless, there has been no demonstration of a performance increase in solar cells taking advantage of MEG in QDs.

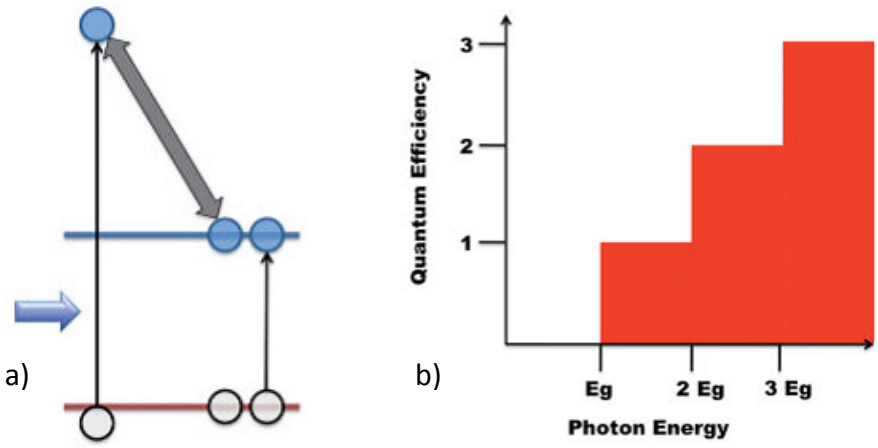

Figure 3.15: The absorption of a photon with an energy over 2 times the band gap can lead to multiple exciton generation (MEG) through impact ionization (a). Resulting step like function of MEG maximum quantum efficiency vs photon energies (b).

Hot-carrier extraction

Theoretical treatments of the hot carrier extraction have shown that efficiencies exceeding 80% are possible under fully concentrated sunlight [47]. However, it is not easy to separate hot electrons and holes to different contacts. As seen before, the entire concept behind maintaining hot carrier populations is a minimization of electron-phonon interactions. In the presence of a metal contact, it would be very easy for the hot carriers to cool to the lattice temperature through the large number of available electronic states. Therefore, in order to create an efficiency increases over traditional cells, it is necessary to extract the hot carriers through an energy selective contact (ESC) as shown in Figure 3.16. These contacts would only allow carriers at a certain energy to leave the absorbing material. Once the carriers enter the contact, they cool to the lattice temperature in the metal contact and, then, the energy that would normally be lost to entropy is instead available for additional work.

While experimental evidence for using QDs to generate MEG exists, directly extracting hot carriers through a selective energy contact has not been demonstrated. The principal requirement for such a contact is a narrow density of states (DOS) with a large band gap between the next available states. However, a narrow DOS also yields extremely low electron mobilities and therefore there must be some compromise between the DOS narrowness and maintaining high enough conductivities.

Originally it was proposed that a wide band gap semiconductor with an impurity band would satisfy this requirement, since it is believed that a periodic distribution of defects could allow for resonant tunneling over a narrow energy range [54].

Another possibility is the use of a periodic arrangement of Si QDs which could form minibands of discrete energies [55]. I-V measurements through these QDs have shown negative differential resistance at room temperature indicating that electrons have a peaked transmission through the QDs at a particular energy. While this does

not prove that the QD superlattice is a proper selective energy contact, it is a good indication that the concept is possible.

One issue that will need to be addressed before hot carrier solar cells are produced is the geometry of the cell. Even with the improved hot carrier lifetimes in quantum systems, the distance the hot carriers can travel before cooling is likely to be very short. Therefore it may be necessary to design the cell in such a way that all the electron-hole pairs are generated very close to the energy selective contacts, to ensure that the carriers do not cool before being collected. Therefore, very short absorber regions may be required to minimize the distance that the hot electrons have to travel.

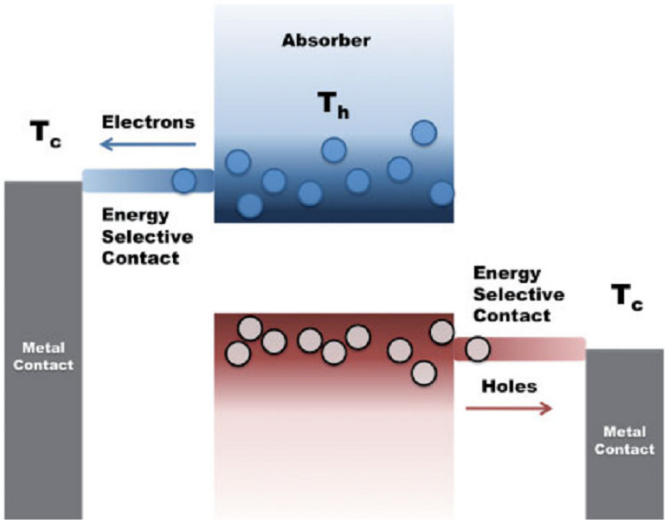

Figure 3.16: Operating principle of hot carrier extraction through energy selective contacts. These special contacts have a narrow distribution of states that only allow electrons and holes over a narrow range of energies to leave the system [48].

3.4.5 Spectrum conversion

Another approach to achieve higher solar cell efficiencies is to convert the sun's polychromatic spectrum to a spectrum more suitable for the solar cell. In this way, sub-band gap photons can be raised above the band gap in a process called up-conversion (UC) or above-band gap photons can reduced to multiple lower energy photons in a process called down-conversion (DC). Using one or both of these processes can theoretically increase the current collected in a solar cell. One of the unique advantages of this concept is that, since only the incoming solar spectrum is modified, it is compatible with many existing solar technologies [56].

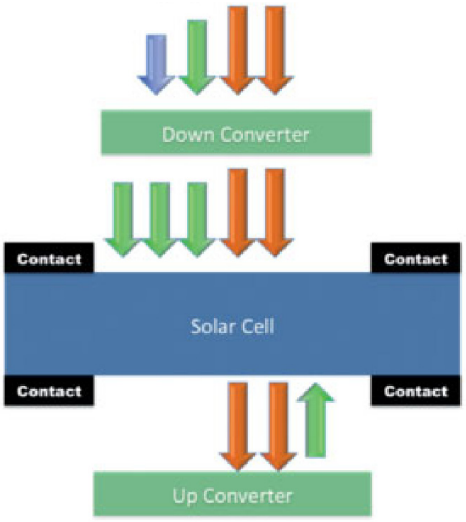

Figure 3.17: Sample structure for a spectrum conversion solar cell. Without converters only two photons (blue and green arrows in the top of the picture) would be absorbed by the solar cell. With the converters in place, four photons are absorbed (green arrows).

Up-conversion

A schematic representation of the two UC processes most frequently discussed for solar cells is shown in Figure 3.18. In the first case two lower energy photons are converted to a higher energy photon through two subsequent absorption events. This process is called ground state absorption/excited state absorption (GSA/ESA). In the other case, the absorption events happen between separate ions, where one of these non-radiatively transfers its energy to its neighbour. This process is called energy transfer up-conversion (ETU). An in-depth analysis of the concept and applicable materials has been previously reported, with the conclusion that ETU mechanisms show the most promise [57].

The UC process has been experimentally demonstrated using a substrate free GaAs solar cell on top of a vitroceramic doped with Yb^{3+} and Er^{3+} [58]. A substrate free solar cell is necessary for UC, otherwise the substrate or contacts on the back of the cell would simply absorb all the incoming below band gap radiation. Unfortunately, the efficiency improvements obtained were low as the emission of above gap photons from this device scales quadratically with respect to incoming below gap photons.

Attempts have been made to improve the efficiency of these devices. Richards has demonstrated a bifacial silicon solar cell with a back coating of erbium-doped sodium yttrium fluoride that has sensitivity in the 1480-1580 nm range [59]. While relatively high external quantum efficiencies could be feasible for this design, only about 2% of the solar spectrum is in this range.

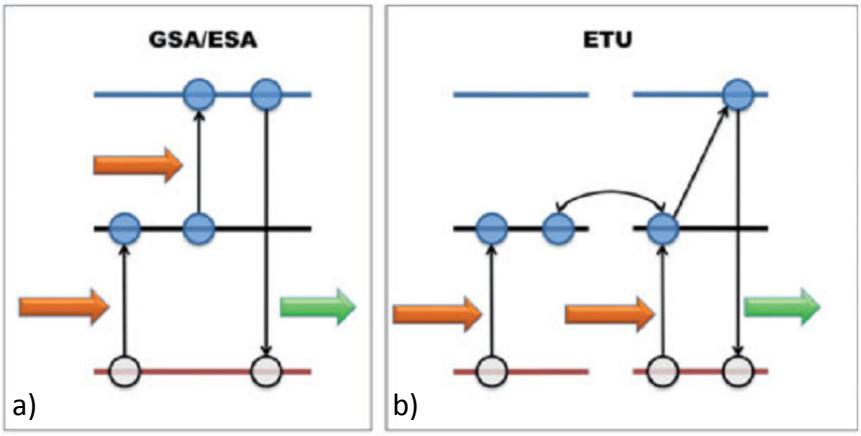

Figure 3.18: Up conversion mechanisms: (a) ground state absorption/excited state absorption (GSA/ESA) and (b) energy transfer up-conversion (ETU).

Down-conversion

In a similar way, it has been proposed that the efficiency of solar cells can be improved by adding a layer in front of the cell that down-converts one high energy photon into two above-band gap photons [60]. However, in order for this design to show large increases in efficiency, it is necessary to obtain external quantum efficiencies above 100%, i.e. at least one outgoing photon for each incoming photon. Some doped phosphors have shown internal quantum efficiencies close to 200%. However, the addition of a material on the front of solar cells would likely change the index of refraction, thereby increasing reflection losses. Given this, it will likely be difficult for these types of devices to show an effective efficiency gain [61].

3.4.6 Low cost alternatives: dye-sensitized and organic solar cells

In an attempt to ultimately decrease the $/W ratio of solar power, several photovoltaic technologies are being developed, with operating principles that differ fundamentally from a traditional silicon solar cell. These technologies include dye-sensitized solar cells (DSSCs) and organic or polymer solar cells. In this paragraph, these technologies and their potential for future cost-effective widespread implementation are examined. Ideally these technologies may provide solar cells of comparable efficiencies but significantly reduced materials and manufacturing costs relative to the crystalline silicon cells that currently dominate the market.

Dye-Sensitized Solar Cells

The simplest DSSC is represented by a piece of glass coated on one side with a 10 μm thick layer of nanocrystalline TiO_2 forming a semiconductor electrode. Since TiO_2 has a band gap of 3.2 eV, it will only absorb the shortest wavelengths of the solar spectrum, leaving most of the energy unused. For this reason, the semiconductor electrode serves mainly as a charge carrier transport mechanism leaving the actual light absorption for another part of the system [62]. The TiO_2 is then coated with a dye that has wide absorption throughout the solar spectrum. Electrons excited in the dye are transferred to the semiconductor electrode leaving the dye in an oxidized state. Only dye molecules in direct contact with the TiO_2 will transmit an electron. On a flat surface, this results in less than 1% incident phototoconversion efficiency. By making the TiO_2 from nanocrystals, a porous interpenetrating layer of TiO_2 and dye molecules can be created with over a thousand times the surface area of a flat surface [63]. In this configuration, the dye can absorb more than 45% of the solar energy flux and convert a high number of these photons to electrical current.

An electrolyte, such as I^-/I^{3-}, is placed between the semiconductor electrode and the counter electrode. An electron is transferred from the counter electrode to the electrolyte, yielding iodine from the triiodide. The oxidized dye is then reduced by the iodine, completing the cycle (Figure 3.19). The photovoltage developed in this system is governed by the difference of the Fermi level energy in the semiconductor under illumination and the Nernst potential of the redox couple, in this case I^-/I^{3-}.

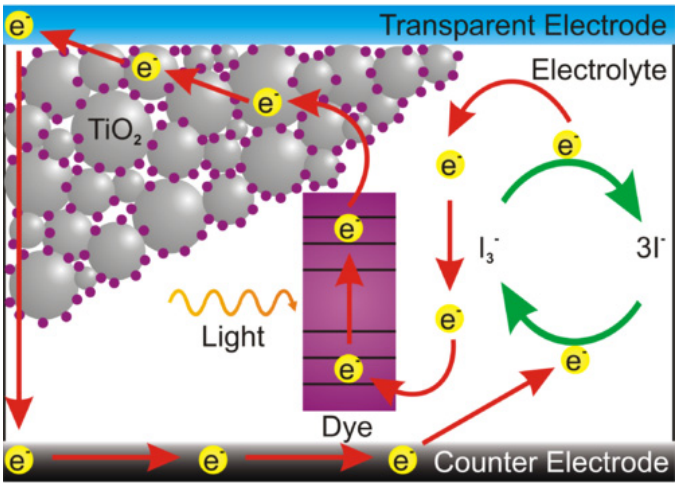

Figure 3.19: Dye-Sensitized Solar Cell structure with the operating principle: photogeneration of charge carriers in the dye, charge carrier transport through TiO_2, reduction of the dye.

In order to determine the practical significance of DSSCs, they must be evaluated in terms of producing cost, efficiency and expected lifetime. The Gratzel cell, published in 1991, was the first cell of this type to achieve practical efficiencies of almost 8% in direct sunlight and 12% under diffuse daylight. Fill factors of 0.68 and 0.76 were reported under full and low intensity sunlight, respectively. The 1991

Gratzel cell was tested after being exposed to visible light for two months and showed a change in the photocurrent of less than 10% (relative).

Recent developments have suggested that doping the TiO_2 with nitrogen would decrease dye degradation from oxidizing holes [64]. These experiments showed no photodegredation after 2000 hours of exposure and were able to maintain relatively high efficiencies of 8%. In order to see widespread implementation, DSSCs would need to be able to maintain efficiencies over 20 years of use, representing 10^8 oxidation/reduction cycles of the dye. Research in this area is focused on selecting and manufacturing electrode, dye, and electrolyte materials to have high solar absorption, low recombination rates, and high stability.

Dye-sensitized solar cells show promise in being a cost effective alternative due mainly to the fact that the expensive and energy-intensive fabrication processes involving very high temperatures and low-pressure associated with traditional semiconductor devices can be avoided. The nanocrystalline structure also make the cell less susceptible to impurities.

Organic solar cells

The low cost of organic compounds and polymers, in combination with their enormous diversity, makes organic compounds and conducting polymers good candidate materials for photovoltaics. It may be possible to find organic replacements for many of the materials traditionally used in DSSCs. While there are many organic compounds that have good absorption in the visible spectrum [65], the main challenge has been transferring this absorbed energy into electrical energy. Improving the efficiencies of organic photo voltaic cells requires separating electrons and holes before recombination. One method accomplishing this is to design the cell as a "bulk heterojunction" with an interpenetrating donor-network. The quantum efficiency of a

cell based on dissociation at a donor-acceptor interface is $\eta=\eta_A\times\eta_{ED}\times\eta_{CC}$ [66]. η_A is the absorption efficiency, which is typically very high for organic compounds. η_{ED} is the fraction of photon generated excitations that reach the heterojunction before recombining. η_{CC} is the carrier collection efficiency, i.e. the probability that a free carrier reaches its corresponding electrode. High η_{ED} rates were very hard to accomplish before the introduction of the bulk heterojunction. Since the excitation diffusion length is typically an order of magnitude smaller than the optical absorption length, by making the material thick enough to absorb a significant amount of solar flux means that most of the electron-hole pairs would recombine well before reaching the junction. In the same way nanocrystalline TiO_2 allowed enormous surface area at the TiO_2/dye junction, an interpenetrating donor-acceptor network greatly increases the exciton diffusion efficiency, η_{ED}. The bulk heterojunction is created by spin coating and solvent evaporation, causing the donor and acceptor materials to separate and creating the extremely intricate interpenetrating network. Tests show that this method can yield η_{ED} values approaching 100%, however low η_{CC} values seem to be a the limiting factor.

Organic Solar cells are now able to reach 5% overall efficiencies. An increase from 2.4% to 5.2% efficiency was achieved by aligning single crystalline nanowhiskers of 1-(3-*methoxycarbonyl*)*propyl*-1-*phenyl*-(6,6)C61 (PCBM) pointing from the anode to the cathode. This significantly increased the electron mobility. To create these crystals PCBM and *regioregular poly*(3-*hexylthiophene*) (P3HT) were bended and then spin cast on the device. Combining PCBM and P3HT created an increase in absorption in the visible spectrum [67].

Charge mobility is still the most significant obstacle to high efficiencies in organic solar cells. Many organic compounds are also susceptible to degradation under UV light. These limitations must be overcome if organic solar cells are to see wide spread use in the photovoltaic market.

References

[1] J. Nelson, The physics of solar cells, London, Imperial College Press, 2003

[2] M.A. Green, Prog. Photovol.: Res. Appl. **9**, 123-135 (2001)

[3] S.W. Glunz Advances in OptoElectronics, Article ID 97370, (2007)

[4] J. Zhao, A. Wang , M.A. Green, F. Ferrazza, Appl. Phys. Lett. **73**, 1991–1993 (1998)

[5] A. Rohatgi, D. S. Kim, K. Nakayashiki, V. Yelundur, B. Rounsaville, Appl. Phys. Lett. **84**, 145 (2004)

[6] K. Nakayashiki, B. Rounsaville, V. Yelundur, D.S. Kim, A. Rohatgi, R. Clark-Phelps, J.I. Hanoka, Solid-State Electron. **50**, 1406 (2006)

[7] M. Boreland, D. Bagnall, "Current and future photovoltaics", review article published online (2006) (http://www.bis.gov.uk/assets/bispartners/foresight/docs/energy/current-and-future-photovoltaics.pdf)

[8] K. Yamamoto, IEEE Transactions on Electron Devices **46**, 2041 (1999)

[9] M.A. Green, P.A. Basore, N. Chang, Solar Energy Materials & Solar Cells **77**, 857 (2004)

[10] X. Wu, J.C. Keane, R.G. Dhere, C. DeHart, A. Duda, T.A. Gessert, S. Asher, D.H. Levi, P. Sheldon Proceedings of 17th European Photovoltaic Solar Energy Conference, Munich, 22–26 Oct., 995–1000 (2001)

[11] I. Repins, M. Contreras, Y. Romero, Y. Yan, W.Metzger, J. Li, S. Johnston, B. Egaas, C. DeHart, J. Scharf, B.E. McCandless, R. Noufi, IEEE Photovoltaics Specialists Conference Record, 33 (2008)

[12] D. Cunningham, K. Davies, L. Grammond, E. Mopas, N. O'Connor, M. Rubcich, M. Sadeghi, D. Skinner, T. Trumbly 28th IEEE Photovoltaic Specialists Conference Record, Alaska, Sept., 13–18 (2000)

[13] Y. Tanaka, N. Akema, T. Morishita, D. Okumura, K. Kushiya, Conference Proceedings, 17th EC Photovoltaic Solar Energy Conference, Munich, Oct. 989–994 (2001)

[14] R. Noufi, K. Zweibel,. WPEC4, Hawaii (2006)

[15] A.D. Compaan, J.R.Sites, R.W. Birkmire, Electrochemical Society Symposium Proceedings, ECS99-11 (2003)

[16] C.H. Henry, J. Appl. Phys. **51**, 4494 (1980)

[17] M.C. Beard, K.P. Knutsen, P.R. Yu, J.M. Luther, Q. Song, W.K. Metzger, R.J. Ellingson, A. J. Nozik, Nano Lett. **7**, 2506 (2007)

[18] C.V. Shank, R.L. Fork, R.F. Leheny, J. Shah, Phys. Rev. Lett. **42**, 112, (1979)

[19] W. Shockley, H. Queisser, J. Appl. Phys. **32**, 510 (1960)

[20] M.A. Green, K. Emery, D.L. King, Y. Hisikawa, W. Warta, Prog. Photovolt: Res. Appl. **14**, 45–51, (2006)

[21] N.J. Ekins-Daukes, C.D.J. Calder, I. Ballard, K.W.J. Barnham, J.S. Roberts, G. Hill. Proc. 3rd World Conference on Photovoltaic Energy Conversion (2003)

[22] G.F. Brown, J. Wu, Laser & Photon. Rev. **3**, No. 4, 394–405 (2009)

[23] H. Yoon, J. Granata, P. Hebert, R.R. King, C.M. Fetzer, P. Colter, K.M. Edmondson, D. Law, G. S. Kinsey, D.D. Krut, J.H. Ermer, M. S. Gillanders, N.H. Karam, Prog. Photovoltaics **13**, 133 (2005)

[24] T. Takamoto, T. Agui, K. Kamimura, M. Kaneiwa, in: Proceedings of the 3rd World Conference on Energy Conversion, Osaka, Japan 2003, Vol. 1, pp. 581–586 (2003)

[25] W. Guter, J. Schöne, S.P. Philipps, M. Steiner, G. Siefer, A. Wekkeli, E. Welser, E. Oliva, A. W. Bett, Frank Dimroth, Appl. Phys. Lett. **94**, 223504 (2009)

[26] P. Wurfel, Physica E **14**, 18 (2002)

[27] K.A. Bertness, S.R. Kurtz, D.J. Friedman, A.E. Kibbler, C. Kramer, J.M. Olson, Appl. Phys. Lett. **65**, 989 (1994)

[28] C. Baur, A.W. Bett, F. Dimroth, G. Siefer, M. Meusel, W. Bensch, W. Kostler, G. Strobl, J. Sol. Energy Eng. **129**, 258 (2007)

[29] J.F. Geisz, S. Kurtz, M.W. Wanlass, J. S. Ward, A. Duda, D.J. Friedman, J.M. Olson, W.E. McMahon, T.E. Moriarty, J.T. Kiehl, Appl. Phys. Lett. **91**, 023502 (2007)

[30] A. Barnett, D. Kirkpatrick, C. Honsberg, D. Moore et al., Proceedings of the 22nd European Photovoltaic Solar Energy Conference, Milan, Italy (2007)

[31] R.A. Stradling, Phys. Scr. T **35**, 237 (1991)

[32] K.W.J. Barnham, G. Duggan, J. Appl. Phys. **67**, 3490–3493 (1990)

[33] B.G. Kluftinger, PhD thesis, University of London (2000)

[34] N.J. Ekins-Daukes, K.W.J. Barnham, J.P. Connolly, J.S. Roberts, J.C. Clark, G.Hill, M. Mazzer, Appl. Phys. Lett **75** 4195 (1999)

[35] G.L. Araujo, A. Martı, Sol. Energy Mater. Sol. Cell **33**, 213–240 (1994)

[36] J.P. Connolly, J. Nelson, K.W.J. Barnham, I. Ballard, C. Roberts, J.S. Roberts, C.T. Foxon: Proceedings of the Conference Records of the 28th IEEE Photovoltaic Specialists, NJ, p.1304. (2000)

[37] J.C. Rimada, L. Hernandez, J.P. Connolly, K.W.J. Barnham, Microelectron. J. **38**, 513 (2007)

[38] P. Wang, C. Klein, R. Humphry-Baker, S.M. Zakeeruddin, M. Graetzel, Appl. Phys. Lett. **86** 123508 (2005)

[39] D.C. Johnson, I.M. Ballard, K.W.J. Barnham, D.B. Bishnell, J.P. Connolly, M.C. Lynch, T.N.B. Tibbits, N.J. Ekins-Daukes, M. Mazzer, R. Airey, G. Hill, J.S. Roberts, Sol. Energy Mater. Sol. Cell **87**, 169–179 (2005)

[40] A. Luque, A. Marti, Phys. Rev. Lett. **78**, 5014 (1997)

[41] M.J. Keevers, M.A. Green, J. Appl. Phys. **75**, 4022 (1994)

[42] A.J. Nozik, Physica E **14**, 115 (2002)

[43] A. Luque, A. Marti, N. Lopez, E. Antolin, E. Canovas, C. Stanley, C. Farmer, P. Diaz, J. Appl. Phys. **99**, 094503 (2006)

[44] R.B. Laghumavarapu, A. Moscho, A. Khoshakhlagh, M. El-Emawy, L.F. Lester, D.L. Huffaker, Appl. Phys. Lett. **90**, 173125 (2007)

[45] N. Lopez, A. Marti, A. Luque, C. Stanley, C. Farmer, P. Diaz, J. Sol, Energy Eng. **129**, 319 (2007)

[46] S.M. Hubbard, C.D. Cress, C.G. Bailey, R.P. Raffaelle, S.G. Bailey, D.M. Wilt, Appl. Phys. Lett. **92**, 123512 (2008)

[47] R. T. Ross, A. J. Nozik, J. Appl. Phys. **53**, 3813 (1982)

[48] M. Wolf, R. Brendel, J.H. Werner, H. J. Queisser, J. Appl. Phys. **83**, 4213 (1998)

[49] Z.Y. Xu, C.L. Tang, Appl. Phys. Lett. **44**, 692 (1984)

[50] J. Blackburn, R. Ellingson, O. Micic, A. Nozik, J. Phys. Chem. B **107**, 102 (2003)

[51] R. Schaller, M. Sykora, J. Pietryga, V. Klimov, Nano Lett. **6**, 424 (2006)

[52] R.D. Schaller, J.M. Pietryga, and V. I. Klimov, Nano Lett. **7**, 3469 (2007)

[53] M.C. Beard, K.P. Knutsen, P. Yu, J.M. Luther, Q. Song, W.K. Metzger, R.J. Ellingson, A. J. Nozik, Nano Lett. **7**, 2506 (2007)

[54] P. Wurfel, Sol. Energy Mater. Sol. Cells **46**, 43 (1997)

[55] G. Conibeer, M. Green, R. Corkish, Y. Cho, E. Cho, C. Jiang, T. Fangsuwannarak, E. Pink, Y. Huang, T. Puzzer, T. Trupke, B. Richards, A. Shalav, K. Lin, Thin Solid Films **511**, 654 (2006)

[56] T. Trupke, M.A. Green, P. Wurfel, J. Appl. Phys. **92**, 4117 (2002)

[57] A. Shalav, B. S. Richards, M.A. Green, Sol. Energy Mater. Sol. Cells **91**, 829 (2007)

[58] P. Gibart, F. Auzel, J. Guillaume, K. Zahraman, Jpn. J. Appl. Phys. **35**, 4401 (1996)

[59] B.S. Richards, A. Shalav, IEEE Trans. Electron Devices **54**, 2679 (2007)

[60] T. Trupke, M.A. Green, P. Wurfel, J. Appl. Phys. **92**, 1668 (2002)

[61] V. Badescu, A. DeVos, J. Appl. Phys. **102**, 073102 (2007)

[62] B. O'Regan, M. Gratzel, Nature **353**, 737–740 (1991)

[63] M. Gratzel, Nature **414**, 338–344 (2001)

[64] T. Ma, M. Akiyama, E. Abe, I. Imai, Nano Letters **5**, 2543–2547 (2005)

[65] S.E. Shaheen, D.S. Ginley, G.E. Jabbour, MRS Bulletin **30** (2005)

[66] P. Peumans, S. Uchida, S.R. Forrest, Nature **425**, 158–162 (2003)

[67] G. Li, V. Shrotriya, Y. Yao, Y. Yang, J. Appl. Phys. **98**, 043704 (2005)

Chapter 4

Metal organic vapour phase epitaxy

4.1 Introduction

Metal organic vapour phase epitaxy (MOVPE) is an epitaxial growth technique based on the use of metal-organic precursors, which belongs to the wider class of chemical vapour deposition (CVD) methods. MOVPE distinguishes itself from metal organic chemical vapour deposition (MOCVD), since the latter relates in general to the deposition of thin films. Epitaxy, on the other hand, is specifically the growth process of a solid film on a crystalline substrate in which the atoms of the growing film mimic the arrangement of the atoms of the substrate [1].

MOVPE technology, developed during the 1970s, immediately revealed to be suitable for the growth of a wide range of III-V, II-VI and IV-VI compound semiconductors. In the last decades, MOVPE has been increasingly used in industrial and commercial production, up to become the main current technique for the large scale production of optoelectronic devices, such as leds [2], lasers [3] and high efficiency multi-junction solar cells [4]. The main features that allowed MOVPE to gain its industrial leadership are its high speed growth, large deposition areas and adaptability in several types of materials.

The MOVPE deposition process takes place with the passage by a vapour phase to a solid one in a growth chamber, in which, under opportune pressure and temperature

conditions, chemical reactions occur. The precursors that have been transported into the chamber undergo homogeneous reactions in the vapour phase and heterogeneous reactions with the substrate, forming the solid compound. The process pressures are usually set to 10-100 mbar, while the temperatures range is from 500 to 700° C.

The main alternative method for semiconductor epitaxial growth is molecular beam epitaxy (MBE), which exploits a molecular beam of the depositing species, produced under ultra high vacuum (UHV) conditions. This beam is supplied from special holders, called "Knudsen cells", containing solid element sources heated by Joule effect. When the shutters of the cells are opened the beam can be formed, arriving on a heated substrate where the deposition occurs. The presence of ultra high vacuum guarantees the growth of high purity samples and makes possible the use of in-situ analysis techniques during the growths, like reflection high energy electron diffraction (RHEED). The advantage of having a rapid source control, since the shutter can be opened and closed in terms of tenths of a second, allows a high compositional control and good, sharp interfaces, enhanced by a lower temperature growth than in MOVPE, usually around 450-550° C or even lower. On the other hand, in terms of costs, the maintenance of an UHV system is one of the biggest disadvantages of this technique compared with MOVPE. Moreover, the deposition is normally available on smaller areas, limiting the use of MBE systems on a large industrial scale. Another disadvantage of this method is faced in the case of epitaxial growth of phosphides, due to the strong phosphorous memory effect connected to the difficulty of cleaning a contaminated MBE chamber.

4.2 MOVPE operating principle

A typical MOVPE system is schematized in Figure 4.1. The growth mechanism is based on the transport of the chemical species present in metal-organic precursors onto the susbstrate, which is heated at high temperature to activate the cracking of the precursor molecules that leads to grow the layers of the desired compounds.

A precursor-rich flow is obtained by fluxing the carrier gas, usually H_2, inside proper stainless steel cylinders (bubblers), kept under stable temperature and pressure conditions, which contain the precursors, in liquid or gaseous form. The carrier gas is saturated with the metal-organic vapours, in order to supply a controlled precursor quantity into the chamber. For this purpose it is fundamental to control the pressure and the temperature of the precursors inside the bubblers. Indeed, the partial pressure of the reactant in chamber (p_{MO}) depends on the thermodynamic conditions through the following equation:

$$p_{MO} = \frac{\Pi_{MO}\Phi_{MO}p_{TOT}}{\Phi_{TOT}K_{MO}}, \tag{4.1}$$

where Π_{MO}, Φ_{MO} and K_{MO} are the vapour pressure, the flux and the pressure of the precursors in the bubblers, respectively, p_{TOT} and Φ_{TOT} being the total pressure and the total flux in the reaction chamber. By controlling the fluxes Φ, it is thus possible to modulate the partial pressure of the component in the chamber.

The reagents that undergo pyrolysis (thermal dissociation) processes react together and with the substrate, to form a new solid phase on the substrate surface. These processes can be described as follows:

$$R_3\text{-III}_{vap} + H_3\text{-V(or R'-V)}_{vap} \Rightarrow \text{III-V}_{sol} + 3\text{R-H}_{vap}, \tag{4.2}$$

where R and R' are generic alkyl radicals, III and V the third and fifth group elements, respectively.

The reagents are conveyed by the carrier gas, with a flow rate between 0.1 and 1 m/s, toward the reaction chamber, where the growth occurs on a crystalline substrate, with a growth rate that is usually around 1 μm/h. As mentioned above, MOVPE is the most used growth method in the optoelectronic industry: for these purposes planetary reactors able to contain up to 60 two-inch substrates or 15 four-inch substrates, such as that shown in Figure 4.2, are employed [5].

In order to understand the growth mechanisms, it is important to analyze the different processes from the thermodynamic, kinetic and fluid dynamic point of view. While thermodynamics is connected to the driving force of the process, kinetics determines the reaction velocity. On the other hand, fluid dynamics, controlling the speed and the material transport at the interface, influences the deposition rate. The study of these three aspects is the subject of the next paragraphs.

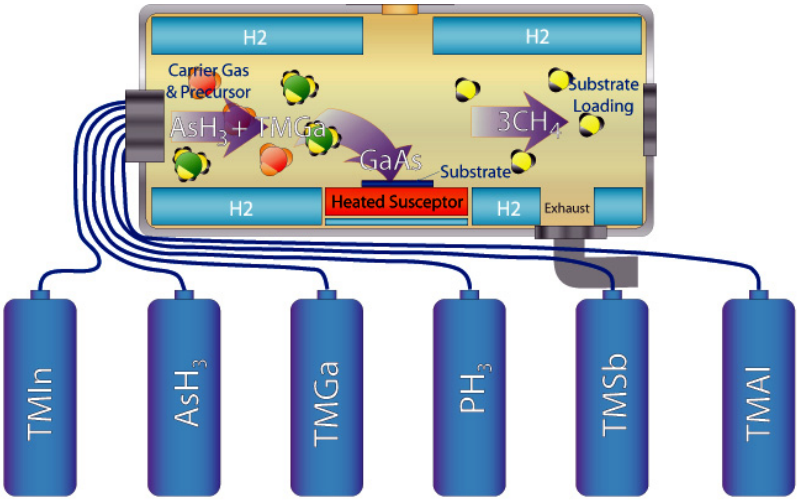

Figure 4.1: Sketch of a MOVPE system. The bubblers containing the metal-organic precursors (in the bottom of the picture) are connected through special stainless steel gas pipes to the reactor chamber, where chemical reactions lead to the formation of the semiconductor layer.

Figure 4.2: Planetary reactor in 60x2" substrate configuration (Source: Aixtron Corporation [5]).

4.3 Thermodynamics

III-V semiconductors are very stable from the chemical point of view, with sp^3 covalent bond and zinc-blende crystal structure. This property allows to employ a large range of experimental conditions for the vapour phase growth, where each gives the compounds with the desired stoichiometric composition, avoiding the creation of secondary phases. The main condition for the growth of III-V compounds is that the V/III ratio, which is the ratio between the partial pressures of group V and III elements in the gas phase, is higher than 1. This requirement is caused by the higher volatility of the group V elements with respect to the group III ones. This difference involves an incongruent evaporation during the growth, determining a lower incorporation of the elements of the fifth group into the layer.

The relationship between the composition of vapour and solid at the solid/vapour interface can be approximated by assuming the thermodynamic equilibrium condition, which is well known and connected to the minimum of the Gibbs energy. The latter is given by:

$$G = E + PV - TS \tag{4.3}$$

In this case we have a 2 phases system and then:

$$G^{TOT} = G^{\alpha} + G^{\beta} \tag{4.4}$$

If the two phases α and β are in equilibrium, the exchange of mass between the two phases in respect to the number of moles i that goes from one to the other, does not alter G^{TOT}:

$$\left(\frac{\partial G}{\partial n_i}\right)^{\alpha}_{T,P,n_j} = \left(\frac{\partial G}{\partial n_i}\right)^{\beta}_{T,P,n_j}, \tag{4.5}$$

where $\left(\frac{\partial G}{\partial n_i}\right)^{X}_{T,P,n_j}$ is the chemical potential of the i-species in the X phase, at constant pressure and temperature. Since the derivative of the Gibbs energy is defined as the chemical potential, the latter equation can be expressed as:

$$\mu_i^{\alpha} = \mu_i^{\beta}, \tag{4.6}$$

where μ_i depends on the partial pressure p_i through the following equation:

$$\mu_i = \mu_{0i} + RT \ln\left(\frac{p_i}{p_{0i}}\right), \tag{4.7}$$

where the index 0 stands for an arbitrary reference state and p_i is given by the product between the molar fraction of the i-species and the total pressure. In the real case, for non-ideal solutions, the partial pressure ratio can be substituted by the activity. In a MOVPE process, the precursors A_i, supposed to be the completely pyrolyzed, react each other giving the crystalline material M_{cryst} and the sub-products B_j. The growth can be expressed by the following general relation:

$$\sum_i a_i A_i \Leftrightarrow M_{cryst} + \sum_j b_j B_j \tag{4.8}$$

The growth process is defined by an equilibrium constant K_p, which depends on the partial pressures of both precursors and sub-products at the thermal equilibrium:

$$K_p = \exp\left(-\frac{\Delta G_r}{RT}\right) = \frac{\prod_j \left(p^e_{B_j}\right)^{b_j}}{\prod_i \left(p^e_{A_i}\right)^{a_i}} \tag{4.9}$$

Equation (4.6) can thus be modified in:

$$\mu_{cryst} = \mu^e_{vap} = \sum_i a_i \mu^0_i - \sum_j b_j \mu^0_j - RT \ln K_p \tag{4.10}$$

The deposition on the substrate occurs under supersaturation conditions, when the equilibrium in the reaction (4.8) is continuously displaced to the right, i.e. when the chemical potential of solid species is minor than that of the gas ones. The driving force of the process is then given by the difference between the chemical potentials of the single phases:

$$\Delta\mu = \mu_{vap} - \mu_{sol} \tag{4.11}$$

If $\Delta\mu>0$ the layer can growth on the substrate. From equations (4.9) and (4.10), $\Delta\mu$ can be expressed as a function of the partial pressures of precursors and sub-products:

$$\Delta\mu = RT \ln\left(\frac{K_p(T)\prod_{j=1}^{n} p^{a_j}_{A_j}}{\prod_{i=1}^{m} p^{b_i}_{B_i}}\right) = RT \ln\left(\frac{\prod_{j=1}^{n}\left(\frac{p_{A_j}}{p^{eq}_{A_j}}\right)^{a_j}}{\prod_{i=1}^{m}\left(\frac{p_{B_i}}{p^{eq}_{B_i}}\right)^{b_j}}\right) \tag{4.12}$$

$\Delta\mu/RT$ is defined supersaturation (σ). The growth occurs in positive supersaturation conditions, which are achieved by the elimination of the reaction sub-products or by saturating the incoming flux of the reagents. The MOVPE process is

endothermic: the deposition occurs with heating absorption. This means that to grant the crystal growth, beyond the supersaturation conditions, heat has to be supplied to the system.

4.4 Kinetics, mass transport and fluid dynamics

The process steps that occur both outside and inside the reactor are sketched in Figure 4.3, from the precursor transport to the layer deposition.

In the pressure range of 10-1000 mbar, mass transport is governed by convection and diffusion. Near the substrate the convective flow is near 0 and diffusion is dominant. The adsorbed species on the solid surface start to diffuse above it, until they are incorporated into the lattice sites. On the other hand, the species that are not adsorbed, or the reaction sub-products, are removed or desorbed and pushed away by the carrying gas flow.

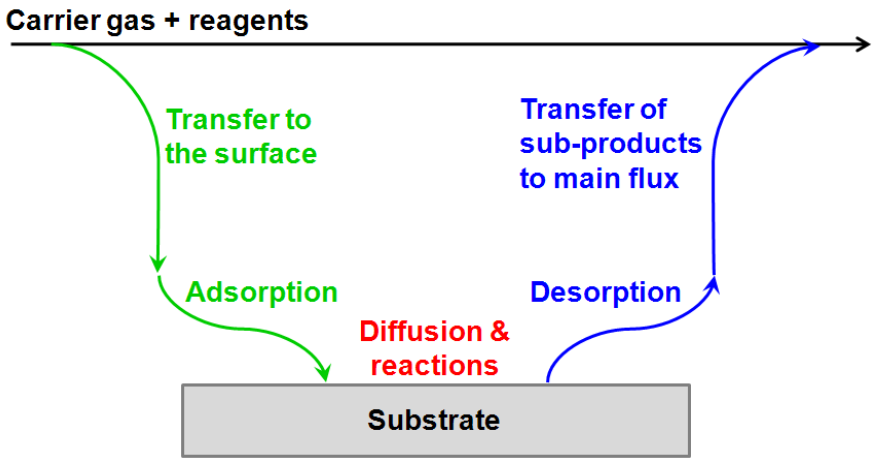

Figure 4.3: Transport and diffusion mechanisms during a MOVPE process.

4.4.1 Heterogeneous reactions

The reaction kinetics depends on the type of reactions involved. In fact the homogeneous reaction rate is proportional to the first power of the species concentration, but when the solid phase participates, the adsorption must be considered. With the purpose to study the atomic adsorption from a quantitative point of view, the Langmuir model can be useful. It is based on the concept that the surface is composed by a fixed number of sites, whose fraction Θ_i is occupied. A simplified assumption is that the activation energy of the adsorption is the same for each site. A chemical bond between the adsorbed atom from the vapour phase and the surface is established through two steps: the atom is at first physically adsorbed, through a weak attraction with the surface, due to van der Waals force; then the atom or the molecule can be desorbed, or find another superficial site, with which a new chemical bond, stronger than the physical one, can be formed. In this latter case a chemical adsorption takes place. The adsorption rate can be expressed, for a given temperature, by:

$$\Theta_i = \frac{k_a p_i}{\left(k_d + k_a p_i\right)}, \tag{4.13}$$

where k_a and k_b are the adsorption and desorption coefficient, respectively. When $\Theta_i << 1$, for low surface recovers, Θ_i is a linear function with the partial pressure. For high temperature and low pressure $\Theta \sim 1$.

The rate of heterogeneous reactions (r) is proportional to Θ_i and Θ_j:

$$r = K\,\Theta_i \Theta_j \tag{4.14}$$

The rate, in function of the partial pressures, can be expressed by:

$$r = K \frac{\beta_i \beta_j p_i^{1/n} p_j^{1/m}}{\left(1 + \beta_i p_i^{1/n} + \beta_j p_j^{1/m}\right)^2}, \tag{4.15}$$

where n and m are the superficial sites for the different species, β the ratios between adsorption and desorption constants and K the constant expressed by an Arrhenius-type equation.

4.4.2 Homogeneous reactions

The MOVPE process starts from a gas mixing, including the carrier gas and the molecular components of the elements that have to be incorporated. The choice of the precursors depends on the desired deposition alloy. The most common are TMGa (trimethylgallium) for gallium, TMIn (trimethylindium) for indium, AsH_3 (arsine) for arsenic and PH_3 (phosphine) for phosphorous. The last two can be replaced, because of their elevate toxicity, by the safer TBP and TBAs (terbutylphosphine and terbutylarsine). The metal-organic precursors, in high temperature conditions, undergo a thermal decomposition, pyrolysis, that makes available the atomic species of the elements to be deposited. During the growth process, different reactions take place. Those that occur entirely in the vapour phase are called homogeneous, those that occur on the solid surface are called, instead, heterogeneous. Both can be divided into unimolecular, in the case that only a molecule is involved, or bimolecular when the reaction is activated in the presence of two reactive species. The most important unimolecolar and homogeneous reaction, for a $M(CH_3)$ species, is the pyrolysis, with the subsequent production of methyl radicals. In the case of precursors formed by longer radical chains (ethylic, propylic and buthylic), also the hydrogen beta-eliminations reaction, with the formation of alkenes and M-H bonds molecules, is induced. In the case of TBAs, the beta elimination produces one C_4H_8 and one AsH_3 molecule [6].

The pyrolysis reactions involve cationic or anionic sources:

Pyrolysis Reaction for a cationic source

Homolytic Fission: $M(CH_3)_n = M(CH_3)_{n-1} + CH_3$

Hydrogenolysis: $H_2 + M(CH_3)_n = CH_4 + HM(CH_3)_{n-1}$

Radical reactions: $CH_3 + M(CH_3)_n = CH_4 + CH_2M(CH_3)_{n-1}$

$H + M(CH_3)_n = CH_4 + M(CH_3)_{n-1}$

In the case that R is a buthylic, propylic, ethylic group a β-elimination reaction occurs:

$MR_n = HMR_{n-1}$ + alkenes

Pyrolysis Reaction for an anionic source

In the case of anionic precursors, homolytic dissociations and hydrogenolysis occur and, with respect to the beta elimination, reactions are faster and more favoured.

Dissociations of the X-H bond are therefore observed: $XH_3 = H_2 + XH$

So as α-eliminations of a H_2 molecule: $RXH_2 = RH$ (alkane) + XH

4.4.3 Growth regimes

Two mechanisms limit the growth rate: one is the gas transport (mass transport), carrying the precursors towards the substrate, the other is determined by the interface reactions that take from the precursors the metallic elements able to form the layer. The two mechanisms have a completely different dependence on the temperature. As said above, the mass transport regime, in a pressure range between 10 and 1000 mbar, is governed by convection and diffusion. Nearby the substrate, the convection flux is practically close to 0 and the diffusion results therefore dominant; in the temperature range typically between 550 and 750° C, the diffusion is slightly temperature dependent.

The situation is very different when the growth rate is limited by chemical reactions (kinetic regime). In this case, in fact, the growth rate depends exponentially on the temperature. To achieve more control on the growth rate and a better quality of the grown layer, the mass transport limited regime is convenient. In almost all the III-V alloys, for example, the growth rate shows a linear dependence on the supplied III group element.

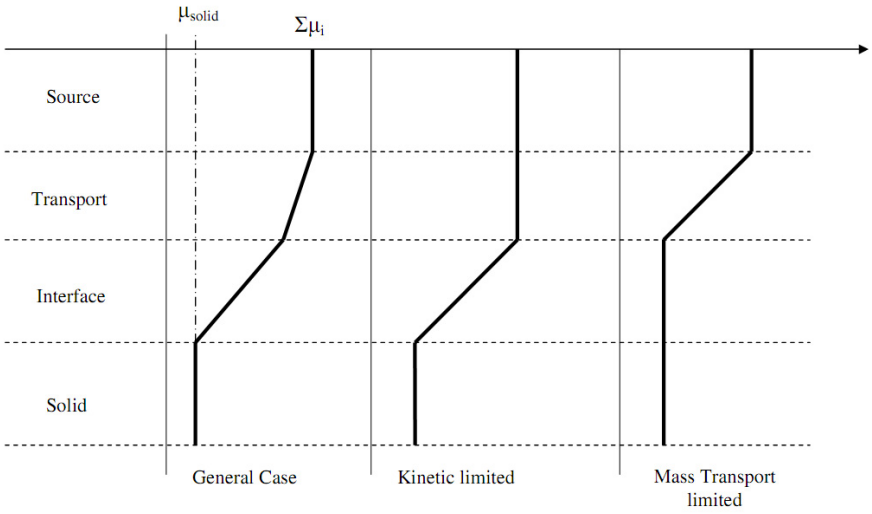

Figure 4.4: Profile of the chemical potential in different regimes.

The growth rate dependence on the temperature is connected to Figure 4.4, where the chemical potential profile in the different regimes is described. The total difference in chemical potential is the driving force for the growth, in the general case the chemical potential is partly consumed for the transport as well as for the reactions at the interface. In case the transport is fast the potential drops mainly at the interface and growth is called reaction limited or kinetically limited. This situation occurs at low temperatures and large partial pressures of the precursors. Just the temperature then

determines the growth rate, which displays exponential behaviour following from the reaction rates (region 1 in Figure 4.5). At high temperatures and low partial pressures the reactions are fast and the mass transport is the limiting factor. The corresponding temperature-independent growth rate is shown in region 2 of Figure 4.5. A decreasing growth rate is finally observed generally at very high temperatures (region 3). This could be expected from desorption of the growing species from the surface, in reality it might be caused also from an enhanced pre-deposition on the reactor walls or on the susceptor because of an extended temperature increase throughout the reactor [1].

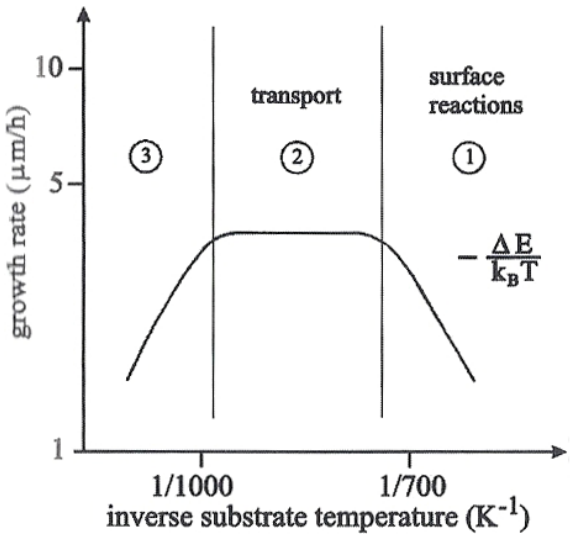

Figure 4.5: Three main regimes of temperature dependence of the growth rate in MOVPE [1].

4.4.4 Fluid dynamic aspects

The most common geometry used in the MOVPE technology is represented by horizontal reactors, formed by quartz walls, cooled by the flux of the same carrier gas. The chosen geometry is very important for the aim to obtain a lateral homogeneous

growth, exploiting a gas flux as laminar as possible. The horizontal chamber, with rectangular and constant section, appears to be ideal for this goal (Figure 4.6).

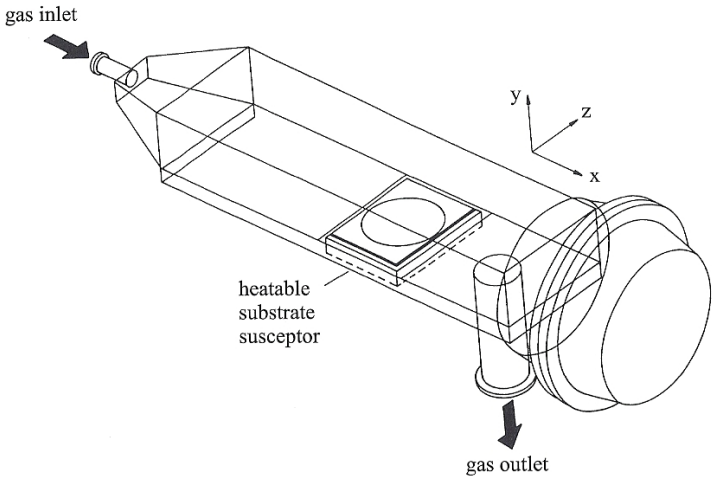

Figure 4.6: Horizontal cold wall quartz reactor with rectangular section [1].

The study of the fluid dynamic aspects, which are highly influenced by the reactor configuration, requires the solution of complex equations, such as the three-dimensional continuity equations for mass, momentum and energy. The continuity equation for each species can be expressed as follows:

$$\frac{\partial \rho_i}{\partial t} = -\nabla\left(\rho_i \vec{v} + \vec{j}_i\right), \tag{4.16}$$

where j_i is the diffusive flow relative to the average velocity of the species $\vec{v}_i$, ρ_i is the mass density of the i species and t is the time. The continuity equation states that the rate with which the material is accumulated in a given volume element is equal to the difference between the incoming and the outgoing fluxes.

The conservation of the linear momentum for each component is described by the Navier-Stokes equation, deduced by the Newton's second law [7]:

$$\frac{\partial \rho \vec{v}}{\partial t} = -\left[\nabla\left(\rho \vec{v}\vec{v} + \vec{\Pi}\right)\right] + \sum_i \rho_i \vec{g}_i \,, \tag{4.17}$$

where ρ is the total density, $\vec{v}\vec{v}$ the dyadic product (second order tensor in which the matrix elements are the products of the two vector components), $\vec{\Pi}$ is the force tensor (i.e. the matrix deriving from the sum between the pressure tensor and the friction forces) and $\vec{g}_i$ is the sum of the external forces per mass unity on the i component.

The conservation of energy condition arises from the first law of thermodynamics:

$$\frac{\partial \rho\left(E + v^2/2\right)}{\partial t} = -\nabla\left\{\rho\left(E + \frac{v^2}{2}\right)\vec{v} + \vec{q} + \left[\vec{\Pi} \cdot \vec{v}\right]\right\} + \sum_i \left(\vec{n}_i \cdot \vec{g}_i\right), \tag{4.18}$$

where E is the internal energy per mass unity, $\vec{q}$ is the heat flux and $\vec{n}_i$ is the total mass flux of the i component. The solution of the continuity and Navier-Stokes equations gives the partial pressure and the flux speed distribution, while the temperature distribution in the reaction chamber can be derived from the conservation of energy equation.

The three abovementioned equations need the border conditions, employed into the model of the boundary layer in a laminar flow, to be solved. In these conditions, the gas velocity onto the substrate and the reactor walls is zero, because of the viscous friction forces. At the same time, also the component perpendicular to the reactor walls is zero, due to the laminar flow. As a consequence, the parallel component of the flux vector is progressively damped, approaching the surface. While leaving the surface, it increases up to the main flux velocity and nearby the walls each flux component is zero again, assuming therefore that deposition occurs above the walls. The thick of the boundary layer, defined as the distance from the growing surface where the x component of the flow speed v is equal to the 99% of the incoming speed, is given by:

$$\delta(x) \cong 5\sqrt{\frac{v_x(x,y)x}{v_0}}, \tag{4.19}$$

where v_o is the non-perturbed gas flow velocity.

In Figure 4.7 the velocity distribution of the gas flow in the reaction chamber, is sketched for the boundary layer model. This model is useful since in the low velocity region the inner forces overcome the viscous ones and therefore the gas can be considered ideal. In the boundary layer the mass transport occur only by diffusion.

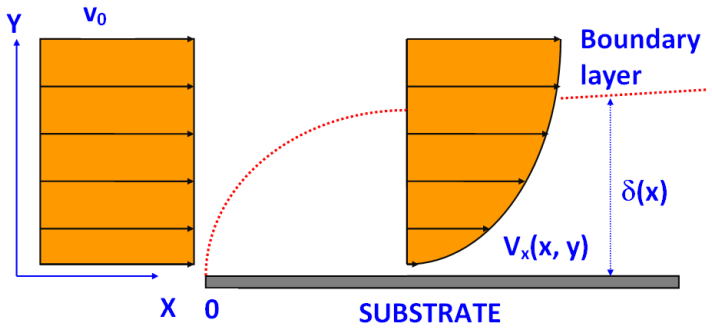

Figure 4.7: Boundary layer model. When the gas flow encounter the susceptor, the velocity profile is modified by the viscous friction forces. The thickness δ of the boundary layer depends on the distance x covered by the gas flow on the substrate.

4.5 Metal-organic precursors

As already described above, before entering the reaction chamber, the carrier gas is enriched with the metal-organic vapours by flowing into the bubblers (sketched in Figure 4.8). The metal-organic sources feature relatively high vapour pressures, around 100 torr at the working temperatures, and are highly reactive with oxygen and water. The most used are trimethyls, because of their high stability [8]. Depending on the group of the metallic element, different chemical properties are presented.

The group II precursors are MR_2 molecules, as dimethylzinc or dimethylcadmium. The elements of the second group have 2 electrons in the s type orbital, in the external shell: to provide two covalent bonds, an sp hybridization occurs, which forms two sp linear orbitals. The so built molecules are electron acceptors, thanks to the not completed p orbitals. In the case of the group III precursors, a sp^2 hybridization takes place (Figure 4.9), with the formation of a trigonal planar molecule, characterized by 3 ligands, separated by 120°. In this way, after the formation of 3 covalent bonds, the p orbital, perpendicular to the molecule plane, remains unoccupied, making the molecule electrophile. Differently, in case of group V metal-organics, where 3p and 2s electrons are present, the formation of 3 covalent bonds and a sp^3 hybridization occurs with tetragonal configuration. They form bond angles around 109.5° with 2 unbound electrons. The present electron pair makes the molecule an electron donor or Lewis basis. The VI group precursors have two s and 4p electrons. Two covalent bonds occupy two of the tetrahedral sp^3 positions.

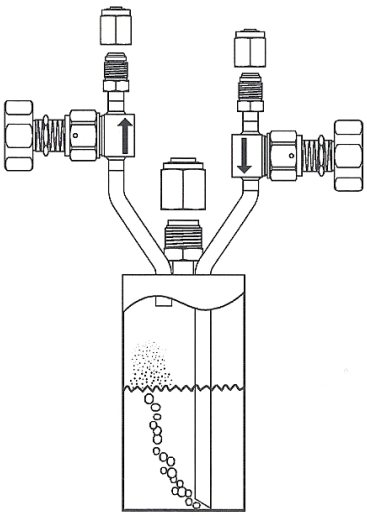

Figure 4.8: Cross section of a bubbler, which allows the carrier gas to pick up the vapours of the liquid precursors [1].

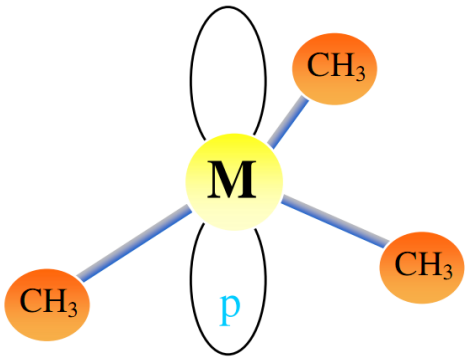

Figure 4.9: M-$(CH_3)_3$ structure of group III precursors (TMIn and TMGa).

In general, the metal-organic precursors must have specific properties in the way to be suitable for the growth: a low pyrolysis temperature, the absence of pre-reactions in the gas phase, a high purity (electronic grade) and low toxicity. TBAs (terbutylarsine) and TBP (terbutylphosphine), whose composition is illustrated in Figure 4.10, satisfy quite well these requirements, in particular by showing a low toxicity and a reduced dissociation temperature [6]. They present very suitable features for the MOVPE process, such as proper vapour pressures, equal to 286 torr (RT) and 96 torr (T=10°C) for TBP and TBAs, respectively. With respect to arsine and phosphine, which are the gaseous precursors most usually employed in MOVPE systems, one of the metal-hydrogen bonds is replaced by a metal-carbon bond: this makes for TBP and TBAs liquid at RT and much less toxic than arsine and phosphine. It is indeed demonstrated that the high toxicity of As and P is connected with the number of V-

hydrogen bonds that are present in the molecules. By substituting one hydrogen atom with an alkyl group, both the toxicity and vapour pressure decrease by an order of magnitude (Figure 4.11) [9]. Moreover, this substitution reduces the cracking temperature of the molecules (Figure 4.12), which entails the possibility to use lower growth temperatures and V/III ratios (with typical values between 1 and 100, compared with 1000 of the hydrides). The compositional control and the homogeneity of the layers are therefore enhanced.

Another advantage due to TBAs and TBP is the reduction of oxygen incorporation in the growing layer, as shown in Figure 4.13, which is extremely convenient for the growth of Al-based alloys [10].

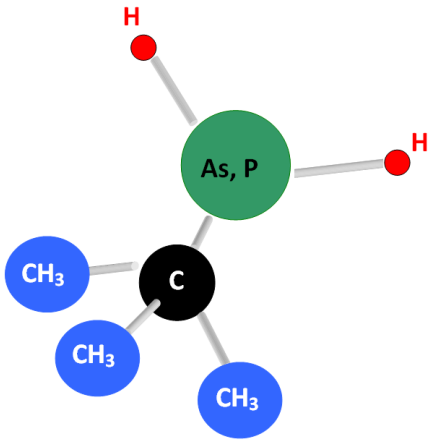

Figure 4.10: $VH_2C(CH_3)_3$ structure of alternative group V precursors (TBAs and TBP).

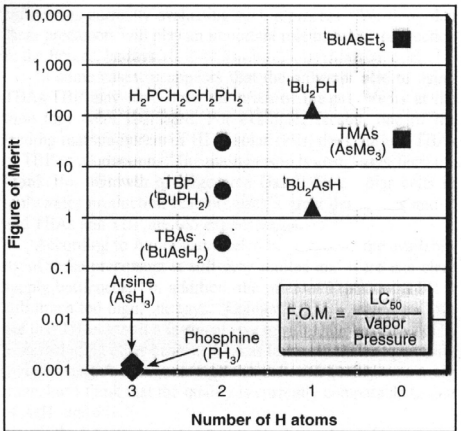

Figure 4.11: Comparison between the toxicity of group V precursors as a function of hydrogen atoms in the molecules. TBAs and TBP present a toxicity reduced by 2 order of magnitude in respect to arsine and phosphine.

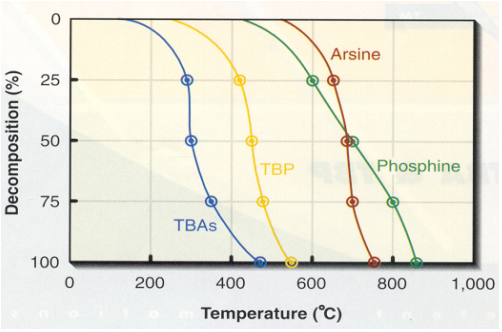

Figure 4.12: Decomposition percentage of traditional (AsH_3, PH_3) and alternative (TBAs, TBP) group V precursors as a function of the temperature.

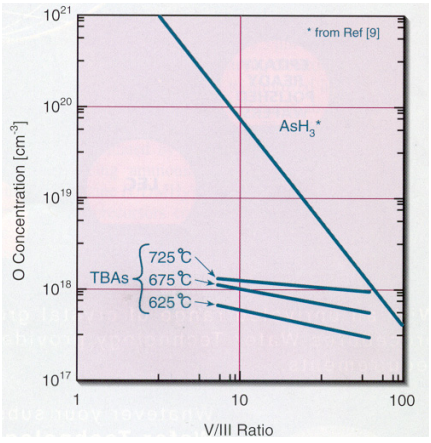

Figure 4.13: Oxygen incorporation in $Al_{0.85}Ga_{0.15}As$ layers grown by arsine or by TBAs.

Finally, for the growth of doped layers of III-V InGaAsP-type semiconductors, zinc and silicon are generally used for the p- and n-doping, respectively. The most common zinc precursors is dimethylzinc (DMZn) that undergoes the 50% of the pyrolysis at a temperature of only 250° C. Silicon in general is supplied by a gas source, such as disilane (Si_2H_6), which is diluted by the carrier gas.

4.6 MOVPE system at Parma SEMLABS

The MOVPE reactor operating at the SEMLABS group of the Parma University is an horizontal AIX200 reactor by Aixtron Corporation, working at low pressures (p>1mbar).

This system, which was used to realize the structures that are the subject of this thesis, is constituted by 4 main parts, as shown in Figure 4.14:

1. A **control panel** for the management of (i) electro-pneumatic valves and mass flow controllers and of (ii) the pressure and temperature conditions in the reactor chamber. All these operations are controlled by a PC, interfaced with the system, for a complete automatic handling of the epitaxial growths.
2. A **gas mixing cabinet**, where the metal-organic sources, which are contained in stainless steel bubblers cooled by thermostatic baths, are diluted by the carrier gas. The mixing of the gas is controlled by electro-pneumatic valves and mass flow controllers.
3. A **horizontal quartz reaction chamber**, where the gas flows converge through stainless steel pre-printed gas lines. The rotating sample holder (gas foil rotation) is sited on a graphite susceptor, which is heated by a system based on IR lamps until a maximum temperature of 850° C.
4. A **glove box** with ultra-pure nitrogen for the substrate loading.

The vacuum system is based on a acid/base resistant rotary pump and a throttle valve for the control of the pressure in the growth chamber. The sub-products of the chemical reactions are neutralized by a two-stage (basic and acid) system for the chemical abatement of harmful gasses, called scrubber. The global safety of the processes is ensured by a sophisticated alarm system and monitoring of harmful gasses, in particular for hydrogen, TBAs, TBP and disilane.

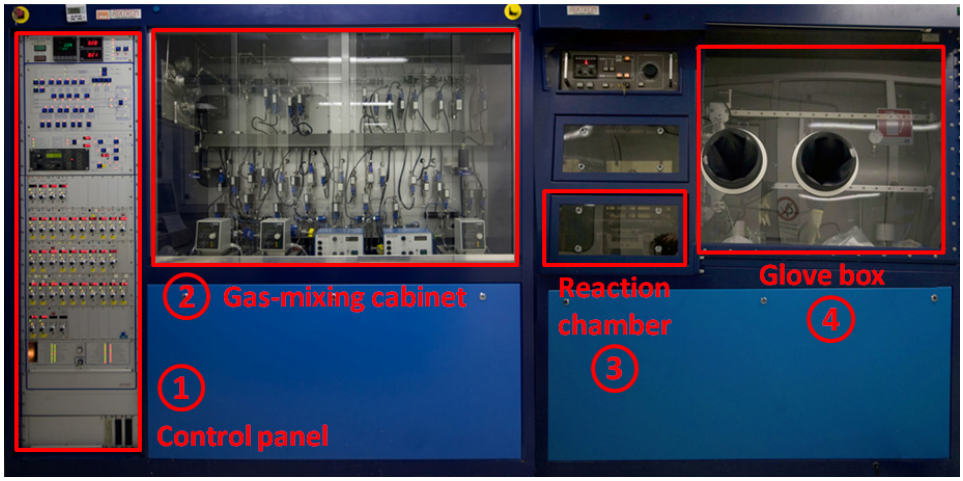

Figure 4.14: SEMLABS AIX200 MOVPE system with its main parts: (1) control panel, interfaced with a pc, (2) gas-mixing cabinet with the precursor bubbler, (3) horizontal quartz reaction chamber, (4) glove box for the substrate loading.

The available precursors are: DMZn (Dimethylzinc) for p-doping, TMIn (trimethylindium), TMGa (trimethylgallium), TMAl (trimethylaluminum) for group III elements, TBP (terbuthylphosphine) and TBAs (terbuthylarsine) for group V elements. For n-doping, gaseous disilane is diluted at 200 ppm in pure hydrogen.

With the aim to obtain a high purity level, indispensable for microelectronic application, all the gasses are ultra-pure and flow in electro-polished pipes. The working gasses are hydrogen and nitrogen with 7.0 and 6.0 purity grade, respectively. During the growth processes, hydrogen is used as the carrier gas because it favours the precursor pyrolysis and can be highly purified: in fact, the hydrogen flux undergoes a further purification through a palladium cell filter, operating at 400° C, which reduces the impurity concentrations below 0.1 ppm. Nitrogen is used in service/standby conditions, for security reasons.

The growth chamber is a cylinder shape pipe with a rectangular section, made of pyrolytic quartz (Figure 4.15). The susceptor, on which the rotating sample holder is placed, is made of graphite. The sample holder rotation is induced by a hydrogen flux operating on the bottom side of the susceptor, which is heated by 5 couples of IR lamps placed beneath, and the temperature is measured by a thermocouple sited inside the susceptor. The rectangular section chamber is contained in an external cylinder: in the gap between the external cylinder and the chamber a hydrogen flow cools down the walls of the internal chamber.

Finally, a proportional-integral-differential (PID) system permits to control the set substrate temperature with an accuracy of a few tenths of degrees Celsius. The hydrogen fluxes control occurs through mass flow controllers, MFC, with a precision of 1% with respect to the full scale value. The bubblers temperature is controlled by thermostat baths, within an error of 0.1° C that makes the sensitivity on the fluxes entering the reactor lower than 2%.

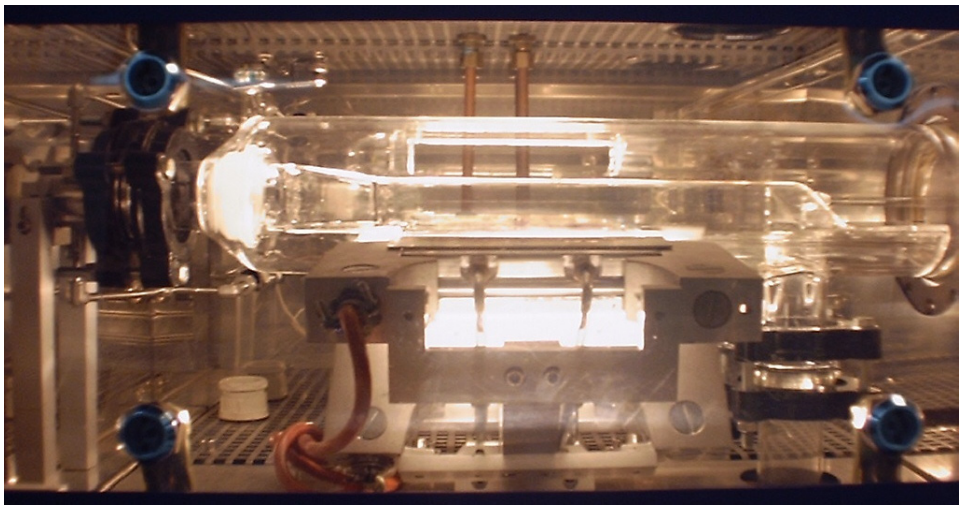

Figure 4.15: The horizontal quartz reaction chamber, enlightened by the IR lamps.

References

[1] M.A. Herman, W. Richter, H. Sitter, "Epitaxy", Springer, Verlag (2003)

[2] A.L. Fischer, "MOCVD systems meet LED demand" Photonics Spectra, published online (2010) (http://www.photonics.com/Article.aspx?AID=41612)

[3] M. Chacinski U. Westergren, B. Stoltz, L. Thylen, IEEE Electron Dev. Lett. **29** 1312 (2008)

[4] S.J.C. Irvine, V. Barrioza, D. Lamba, E.W. Jonesa, R.L. Rowlands-Jones, J. Cryst. Growth **310**, 5198-5203 (2008)

[5] Aixtron production systems (http://www.aixtron.com)

[6] G.B. Stringfellow, "Organometallic Vapor-Phase Epitaxy: Theory and Practice" Academic Press (1989)

[7] D.J. Tritton, "Physical Fluid-Dynamics", Oxford University Press (1988)

[8] J.W. Mattews, A.E. Blakeslee, J. Cryst. Growth **27**, 118 (1974)

[9] W. Stoltz, T. Whithaker, Compound Semiconductors **5**, 29 (1999)

[10] H. Tanaka, T. Kikkawa, K. Kasai, J. Komeno, Jpn. J. Appl. Phys. **28**, 901 (1989)

Chapter 5

InGaP/GaAs MQW structures

5.1 Introduction

The lattice-matched $In_{0.48}Ga_{0.52}P$/GaAs heterostructure is generally recognized as a very interesting system for microelectronic and optoelectronic applications. In particular, it represents a valid alternative to the AlGaAs/GaAs heterostructure, thanks to (i) lower oxidation tendency, (ii) higher mechanical stability, (iii) reduced DX centres and (iv) lower interfacial recombination velocity [1, 2]. These properties open the door to a broad-spectrum of applications, such as heterojunction field effect transistors (HFETs) [3], heterojunction bipolar transistors (HBTs) [4], high power lasers [5] and solar energy conversion devices [6]. Referring to the latter one, InGaP/GaAs heterostructures can be inserted in a multilayer structure to obtain a better matching of the solar spectrum through an enhanced light absorption and then to improve photovoltaic device performances. The quantum well solar cells (QWSC) technology, in fact, appears to be a potential candidate to achieve high conversion efficiency devices, as discussed in chapter 3. The crucial technological requirements for the modelling, realization and test of prototypal photovoltaic devices based on low-dimensional systems, include: (i) as sharp as possible superlattice interfaces, (ii) control of residual lattice strain and structural disorder, (iii) high regularity of the QW periodicity and good correspondence between modeling and experimental

determination of the band gap profile, (iv) reduction of background impurity and deep level density. Nevertheless, the required monolayer abruptness of the InGaP/GaAs interfaces is not easily obtainable by MOVPE, owing to both the As/P intermixing and the In memory effect, which are deeply influenced by the adopted gas switch sequence (GSS) during the interface growth [7]; moreover, In surface segregation effects can induce In-rich InGaP surface layers and In incorporation in GaAs-on-InGaP layers [8]. As a consequence, unintentional $In_xGa_{1-x}As_yP_{1-y}$ intermediate layers are formed at the direct GaAs-on-InGaP interface, so that the optical properties of the InGaP/GaAs/InGaP QWs are affected by undesired, low-energy features and the QW emission is dramatically reduced with photoluminescence (PL) line-shape broadening [9].

At Parma SEMLABS different sequences of unintentionally doped GaAs/InGaP MQWs, confined within InGaP cladding layers, were grown by low pressure MOVPE. Single QWs, as well as MQWs, with different periods, variable well size, gas switching sequence at the interfaces and indium concentration in the InGaP alloy were prepared. An accurate study, aimed at the improvement of the interface sharpness and the optical response of QWs, was conducted by investigating different GSSs and intentional interlayers (IL) between QW and barriers. In this sense, the insertion of a GaAsP IL at the direct GaAs-on-InGaP interface revealed to be very successful, limiting As/P intermixing and In interdiffusion [10]. The PL spectra (Figure 5.1) indicate that the insertion of the IL evidences the emission from QW, while in identical samples without the GaAsP layer the emission is observed at a lower energy than the GaAs band gap. The role of the IL is confirmed by the fair agreement between experimental and theoretical XRD profiles (Figure 5.2), which also give evidence in favor of the high quality of the structure and the good control of the lattice match at the InGaP/GaAs interface. The latter result is particularly valuable, considering that the growth of matched heterostructures requires extremely precise

conditions, such as indium content in InGaP of 48.4%. The modified GSS of the MOVPE process is reported in Figure 5.3.

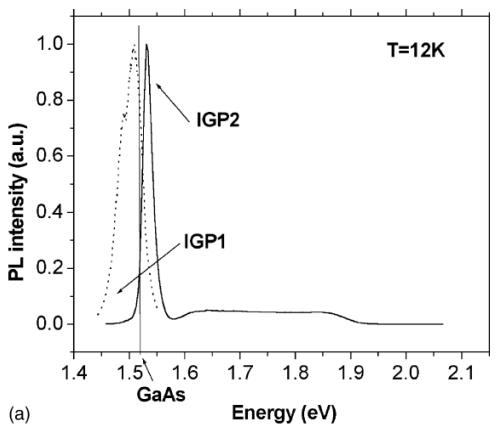

Figure 5.1: T=12 K. PL spectra of two QW structures having the same well width (8 nm); when the IL is absent (IGP1, containing 20 GaAs wells) the emission is observed at a lower energy than the GaAs band gap (low energy peak, dotted line); when the IL is inserted (IGP2) the confinement energy is evidenced (continuous line).

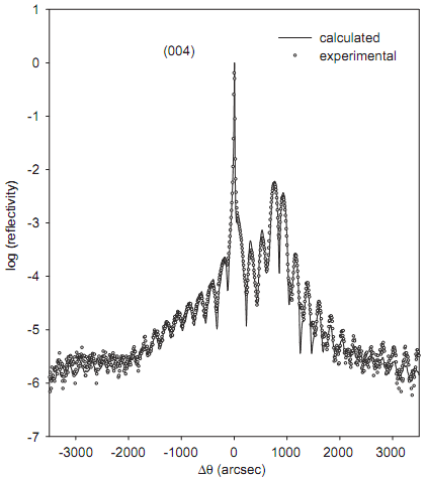

Figure 5.2: XRD 004 experimental (dot) and calculated (line) profiles of a single QW structure (IGP2) in which a GaAsP interlayer (IL) was inserted at the direct interface.

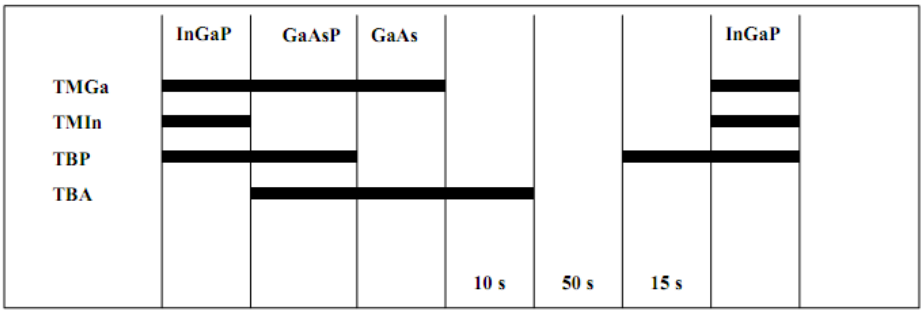

Figure 5.3: Modified GSS employed to insert a GaAsP IL at the direct interface; an opening time of 4 seconds corresponds to ~4 MLs. A 50 seconds hydrogen purge was also performed during the growth of the indirect interface.

The assessment of the growth parameters was exploited for the design and realization of $p^+/MQW/n^+$ junctions, which represent the basic structure for novel photovoltaic devices (QWSCs), in collaboration with professor Keith Barnham, chief of the Quantum Photovoltaics Group of the London Imperial College. The samples, composed of a lattice matched and nominally undoped GaAs/InGaP MQW region interposed between a n^+ GaAs (001) substrate and a p^+ GaAs cap layer, were grown at SEMLABS by AIX 200 RD reactor at the growth temperature T_g of 600° C (see details in paragraph 4.6). The undoped MQW region, consisting of 25 to 40 periods of L_W(GaAs)=8 nm and L_B(InGaP)=12 nm, was protected from the impurity diffusion from the cladding layers, by the interposition of proper intrinsic spacer layers. The most interesting structure, called IGPCELL1, presents 30 periods of GaAs QW in the intrinsic region of a InGaP p-i-n junction (Figure 5.4).

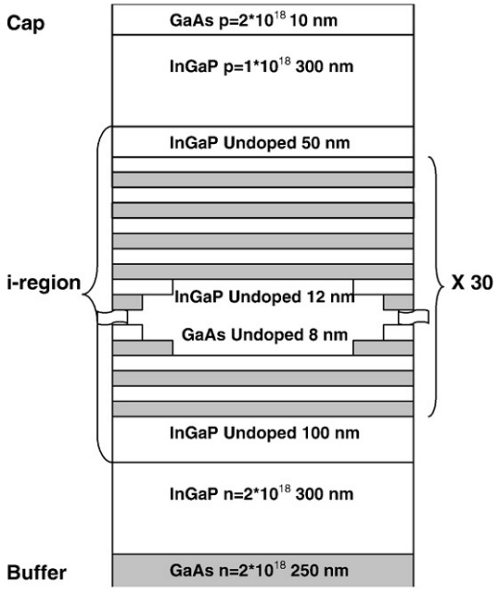

Figure 5.4: Structure and main features of IGPCELL1, an InGaP p-i-n structure based sample containing 30 stacked GaAs/InGaP MQWs.

A very high optical quality of the sample appears from the low-temperature (12 K) FFT–PL spectrum. The intense emission peak at E=1.530 eV shown in Figure 5.5 corresponds to the energy calculated for a radiative recombination between the n=1 electron and heavy hole levels (hh_1-e_1 transition). The full-width at half-maximum (FWHM) of 12 meV suggests a negligible presence of compositional or structural disorder. Actually, the QW localization effect, increasing the wavefunction overlapping, makes the radiative recombination channel more effective. The energy peak position was also confirmed by a CL investigation, indicating a good reproducibility over all the samples prepared with the same modelling parameters.

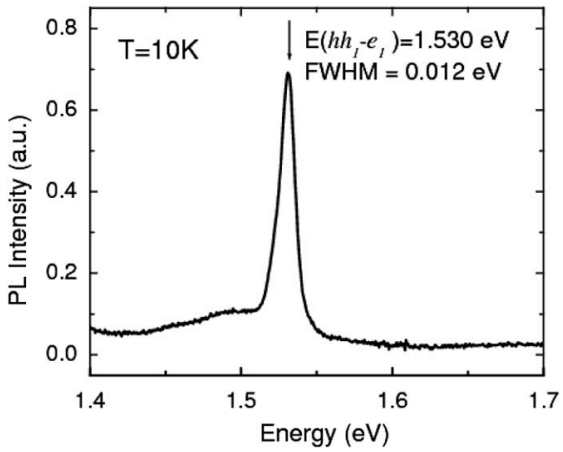

Figure 5.5: FFT–PL spectrum at T=10 K of IGPCELL1.

The dark I–V curves at 300 K of small area diodes are shown in Figure 5.6. The ideality factor is 1.25, showing a minor contribution of generation-recombination transport mechanisms across the heterojunction.

The rectification ratio is about 10^{10} at 1.2 V, while the reverse characteristic exhibits a current lower than 10^{-11} A at 7 V. The deviation from the straight line observable at high forward current is usually attributed to the series resistance, in this case probably

due to the limiting effect on the transport of the QWs. The dark current (I_d) reduction in MQW samples is consistent with the value lying between those expected for two p-n junctions formed by the well and the barrier materials: in particular, we observe that the dark current densities at 1 V bias vary from 0.28 A/m^2, to 0.18A/m^2, to 11.4 A/m^2, as the inserted MQWs are 0–10–30, respectively. Such values are in reasonable agreement with the results of Ref. [11] for an analogous InGaP/GaAs QWSC, containing 40 MQWs. Table 5.1 resumes the results of the characterization with a solar simulator of a large area cell with the same structure of IGPCELL1 (called IGPCELL3) and of a control cell obtained by substituting the QW region with an undoped InGaP layer of equivalent thickness (called IGPCELL4). Although it appears that the presence of the 30 QWs yields a slight increase of the fill factor, the conversion efficiency turn out to be quite limited, because of a poor photocurrent and unexpectedly low V_{OC} values. The reason of this behaviour is almost certainly related to an undesired background doping of the nominally intrinsic InGaP alloy in the MQWs, which shows *p*-type conductivity with net acceptor density in the 10^{16} cm^{-3} range. In fact, according to Osborne [12], if the background doping level inside the intrinsic region overcomes the value of 10^{15} cm^{-3}, the electric field profile can significantly vary through the intrinsic region and degrade the performance of the solar cell. In this way the transit time of the photocarriers which could be swept out by the internal electric field before recombining is reduced [13]. A smaller thickness of the MQW region could favour a more uniform distribution of the electric field along the structure, but the efficiency would be in this case penalized by a too thin active layer in the device , as can be deduced by the comparison reported in figure 5.7. The relatively high background impurity concentration in the undoped InGaP layers resulted independent of the carrier gas; anyway, in one of the few reported attempts for the lattice-matched InGaP/GaAs MQWSC, a similar problem with the background doping in the 10^{16} cm^{-3} range was faced [12]. We suppose that the

contribution to the native acceptor concentration is related to the incorporation of carbon during the MOVPE growth, which is both present in the methyl and terbutyl radicals of the metalorganic precursors. Although MOVPE grown InGaP usually exhibits an n-type conductivity with electron concentrations around 10^{15} cm^{-3}, also when TBP is used [14], our growth conditions seem to enhance the tendency of the amphoteric carbon impurity to induce acceptor levels. Malacký et al. [15] reported of a high concentration of native acceptors, likely carbon, in InGaP MOVPE grown by phosphine at 560° C; to date, no other acceptor sources could be identified in our InGaP layers.

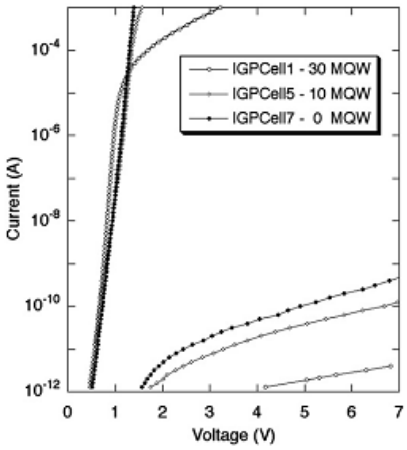

Figure 5.6: Dark I–V curves at RT from 500 micron diodes of IGPCELL1.

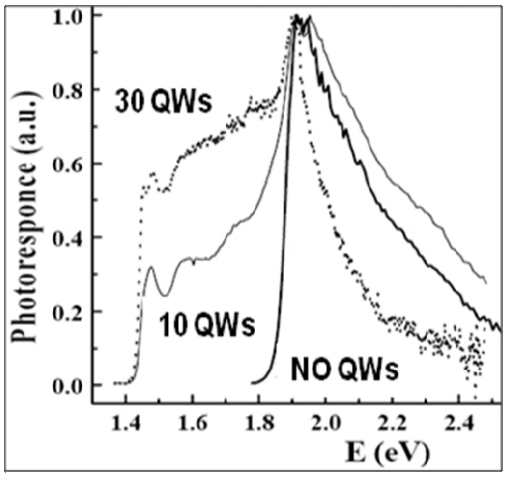

Figure 5.7: Spectral response at RT of different InGaP/GaAs MQW structures having 0–10–30 QWs.

Table 5.1
Photovoltaic characteristics for large area cells obtained with a solar simulator.

Sample	Cell area (cm^2)	I_{SC} (mA)	V_{OC} (mV)	FF (%)
IGPCELL3	4	5.416	839.76	0.46
IGPCELL4	4 (control cell)	6.836	984.76	0.38

The effect of the undesired background doping on the built-in electric field profile across the MQW region was exploited by using admittance spectroscopy (AS) [16]. Moreover these measurements let us to determine the valence band (VB) offset of the InGaP/GaAs heterostructure, A synthesis of this study is reported in the next paragraph, while the second part of the chapter deals with an accurate photoelectric spectroscopy study of IGPCELL1 sample, carried out to investigate the optical absorption properties and the transport mechanisms of the structure. At different temperatures and excitation modulation frequencies, a peculiar behaviour in the photoelectric response was observed, which was attributed to the same resonance phenomenon highlighted by the admittance analysis.

5.2 Admittance spectroscopy

The conduction and valence band offsets ΔE_C and ΔE_V play a major role on the interface properties of a heterojunction and heavily influence the modelling and the performance of any related devices. Consequently, a detailed knowledge of the energy band alignment is highly desirable. In spite of that, the measured band discontinuities at the InGaP/GaAs interface spread over a wide range of data, with experimental uncertainties ranging from 5% up to 30% or more [17-20]. Such a wide spread of data is often ascribed to different growth methods and growth conditions or different measurement techniques. More specifically, the difficult control of the InGaP composition required for the lattice matching to GaAs, the intermixing effects at the interface and the uncontrolled formation of ordered domains in the cation sublattice are expected to play a major role in affecting the band offsets. Amongst electrical methods, admittance spectroscopy of MQWs has been proven to be very accurate. Its advantage is that the band offset is derived through a straightforward analysis of the

temperature dependence of an easily measurable resonance frequency, rather than through cumbersome simulations of current-voltage or capacitance-voltage curves, as required in other electrical methods.

The undesired band bending configuration of the MQW region is qualitatively sketched in Figure 5.8 together with the equivalent circuit of the structure, as proposed in Ref. [21] for the interpretation of admittance measurements in GaAs/AlGaAs MQW structures. C_1 is the capacitance of the depleted MQW region, whereas R and C_2 are, respectively, the resistance and the capacitance of the undepleted flat band part of the MQW region. The measured conductance G(ω) and capacitance C(ω) obey the equations:

$$\frac{G(\omega)}{\omega} = \frac{(\omega/\varpi)[C(0) - C(\infty)]}{1 + (\omega/\varpi)^2}$$
$$C(\omega) = \frac{C(0) - C(\infty)}{1 + (\omega/\varpi)^2} + C(\infty) \qquad (5.1)$$

Here $\omega=2\pi f$ is the angular frequency of the small amplitude test signal, C(0) and C(∞) are the measured capacitances in the low and high frequency limit, respectively, related to C_1 and C_2 by the equations:

$$C(0) = C_1 \qquad C(\infty) = \frac{C_1 C_2}{C_1 + C_2} \qquad (5.2)$$

while ϖ is the resonance angular frequency given by

$$\varpi = \frac{1}{R(C_1 + C_2)} = \frac{C(0) - C(\infty)}{RC^2(0)} \qquad (5.3)$$

Experimental C(ω) and G(ω)/ω curves taken at different temperatures are shown in Figure 5.9, where the step behavior of C(ω), with inflection point at ϖ, and the peak shape of G(ω)/ω, with maximum at ϖ, are clearly evidenced.

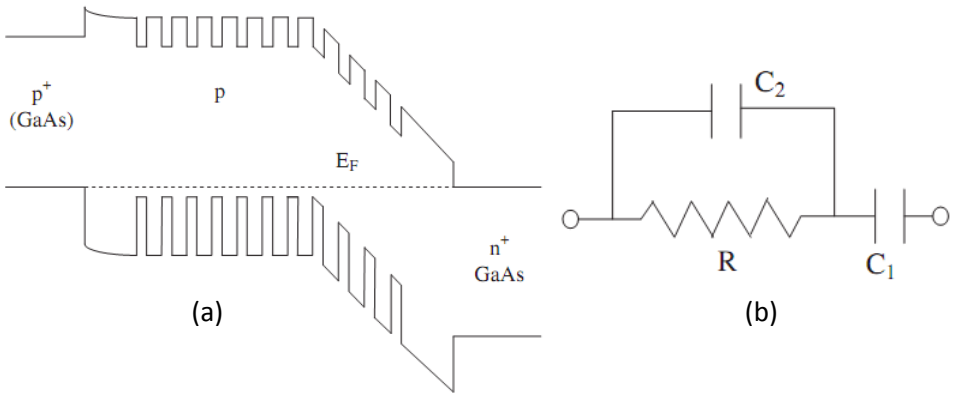

Figure 5.8: Equilibrium band bending diagram of the $p^+/MQW/n^+$ structure (a) and the equivalent electrical circuit (b).

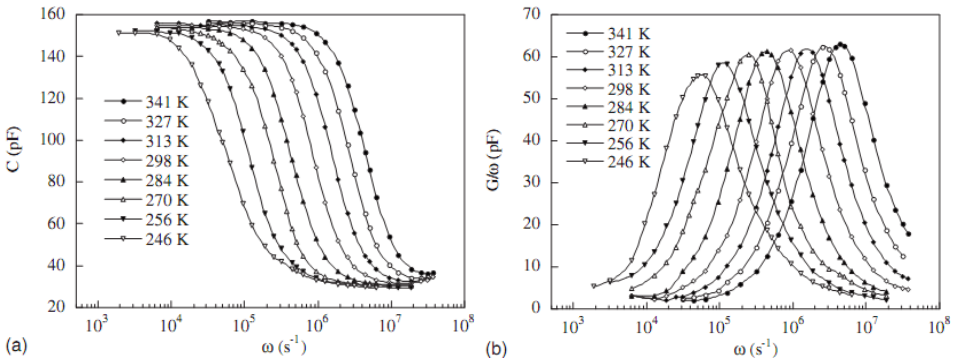

Figure 5.9: Experimental C(ω) (a) and G(ω)/(ω) curves taken at different temperatures in the investigated $p^+/MQW/n^+$ structure.

The admittance of the whole structure, at the extreme limits of low and high frequencies, has a particular physical meaning. The high frequency capacitance is related to the geometrical thickness L of the undoped region, that is, $C_\infty=S(\varepsilon/L)$, where S is the junction area, and depends on the temperature only through the dielectric constant ε. In the explored temperature range, C_∞ can be considered a constant value, equal to 29.5 pF: if a mean dielectric constant $\varepsilon=12\varepsilon_0$ is used, this

value is consistent with a thickness of the nominally intrinsic region equal to L=721 nm; this latter value should be compared with the expected one of 783 nm, calculated by adding the thickness of 30 stacked periods of barrier-well sequence to that one relative to the two undoped InGaP top and bottom spacers. A small discrepancy in these evaluations of L is not surprising if the following comments are accounted for: i) the compositional non-uniformity of the QW region imposes the assumption of an empirical mean dielectric constant between the two compounds, giving an uncertainty in the estimation of L; moreover, ii) a significant Zn diffusion from the p-type cladding layer into the adjacent nominally undoped InGaP spacer layer cannot be excluded, resulting in a shorter effective L value. Concerning C_0, which is the measured capacitance in the low frequency limit, it is equal to $C_1=S(\varepsilon/L_{dep})$ and exhibits a non-negligible decrease with temperature: this is also evidenced by the reduction in temperature of the $G(\omega)/\omega$ peak intensity, which is given by $[C_0-C_\infty]/2$. An estimation of the depleted region thickness of $L_{dep}=135$nm can be obtained by $C_1=155$pF at T=313K. Since C_∞ is constant and C_0 is only weakly dependent on temperature, the observed increase of ϖ with temperature can be mainly ascribed to a decrease of the series resistance R.

The temperature dependence of the R^{-1} conductance of the undepleted p-type MQW region is found by considering that at high temperatures the perpendicular conduction is due to thermoionic emission of holes over the InGaP barriers. Owing to arguments quite similar to those in Ref. [21], the thermoionic current J can be written as:

$$J=\text{const}\times T^2\exp\left(-\frac{E_F-E_{VB}}{K_BT}\right)\left\{\exp\left(\frac{qV}{2K_BT}\right)-1\right\} \quad (5.4)$$

where E_F is the Fermi energy, E_{VB} the valence band top of the InGaP barrier, V is the applied voltage dropping on a single QW, q is the absolute value of the electron

charge and K_B the Boltzmann constant. For small voltages, such as $qV<<K_BT$, equation (5.4) reduces to:

$$J = \text{const} \times T\,V \exp\left(-\frac{E_F - E_{VB}}{K_B T}\right) \tag{5.5}$$

So that:

$$\varpi = \text{const} \times R^{-1} = BT \exp\left(-\frac{E_F - E_{VB}}{K_B T}\right) \tag{5.6}$$

where B is independent of temperature. Introducing E_1^{hh} as the lowest energy level for the heavy holes confined in the QW (Figure 5.10), we have $E_F - E_{VB} = (E_F - E_1^{hh}) + (E_1^{hh} - E_{VB})$ and consequently:

$$\ln\left(\frac{\varpi}{T}\right) = \ln B - \frac{(E_F - E_1^{hh})}{K_B T} - \frac{(E_1^{hh} - E_{VB})}{K_B T} \tag{5.7}$$

Owing to this equation the energy difference $(E_1^{hh} - E_{VB})$ can be obtained by analyzing the temperature dependence of $\ln(\varpi/T)$ if the temperature dependence of the Fermi energy is known. In the limit of a not degenerate two-dimensional hole gas populating only the lowest heavy hole subband one easily gets:

$$(E_F - E_1^{hh}) = K_B T \ln(C K_B T) \tag{5.8}$$

where C is a constant with temperature. In this case, equation (5.7) takes the simpler form:

$$\ln \varpi = \ln\left(\frac{B}{C K_B}\right) - \frac{(E_1^{hh} - E_{VB})}{K_B T} \tag{5.9}$$

and, consequently, the Arrhenius plot of $\ln \varpi$ vs $(K_BT)^{-1}$ gives $(E_1^{hh} - E_{VB})$ (see Figure 5.11). The sheet hole density in a single QW resulted in the range $(0.7–1.3)\times10^{11}$ cm^{-2}, implying that more hole subbands are significantly populated; however, their

occupancy is well described by the Boltzmann statistic, so that the inclusion of the higher subbands mainly affects the absolute value of the Fermi level, without important variation of the temperature dependence. The use of equation (5.9) to obtain ($E_1^{hh}-E_{VB}$) is therefore again justified, as a first order approximation, with a different meaning of the constant coefficients: we get ($E_1^{hh}-E_{VB}$)=336±5 meV. The valence band offset is $\Delta E_V=(E_1^{hh}-E_{VB})+(E_{VW}-E_1^{hh})$, where E_{VW} is the top of the GaAs valence band. Since the calculated confinement energy of the heavy holes ($E_{VW}-E_1^{hh}$) for a well depth of 340 meV is 10 meV, we have ΔE_V=346±5 meV. The above value for ΔE_V can be compared with the published experimental values, which spread in the rather wide range of 300–400 meV.

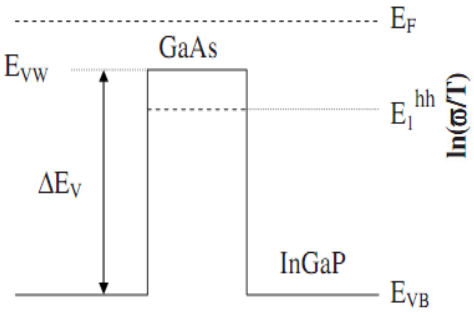

Figure 5.10: Energy levels and valence band profile for a QW in the undepleted p-type MQW region. E_F is the Fermi energy. E_{VW} and E_{VB} are the valence band top in the GaAs well and in the InGaP barrier, respectively. E_1^{hh} is the deeper energy level for the confined holes.

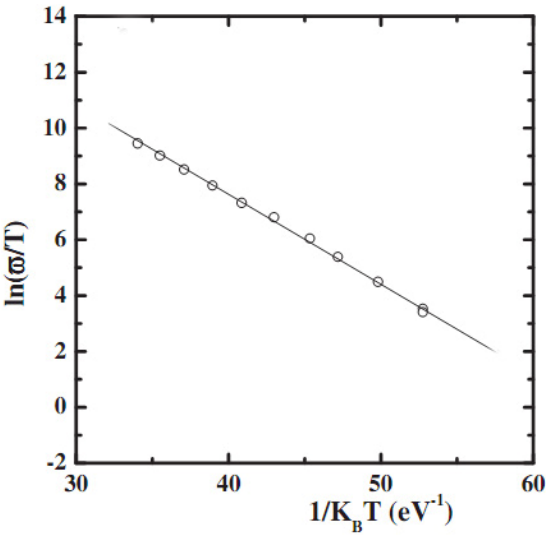

Figure 5.11: Arrhenius plot of $\ln(\varpi(T)/T)$ vs. $(K_BT)^{-1}$. The slope gives ($E_1^{hh}-E_{VB}$)=(336 ± 5) meV.

5.3 Photoelectric spectroscopy

Photoelectric spectroscopy (PES) measurements on semiconductor structures consist in recording, as a function of the wavelength of the exciting light, the electrical signal (current or voltage) produced by the optically generated excess charge carriers. In particular, PES is based on different requirements:

i. a threshold energy for the optical absorption of the incident light, controlled by the fundamental absorption edge of the material. The absorption coefficient $\alpha(\lambda)$ determines the light penetration depth, which is proportional to $1/\alpha(\lambda)$, where λ is the light wavelength;

ii. the generation of excess charge carriers, whose steady state density results from the solution of a continuity equation which takes into account the different processes driving the non-equilibrium carriers dynamics (drift, diffusion, generation and recombination). The excess carriers modulate the built-in voltage either resulting in a related photovoltage (PV) at open circuit, or inducing a photocurrent (PC) in a short circuit configuration. Both the signals are measurable as a function of λ, the temperature T, the photon flux density and the modulation frequency of the excitation light.

iii. the presence of an internal electric field (built-in voltage), induced by the alignment of the Fermi level at the interface of a p-n junction (or heterojunction), which contrasts majority carrier diffusion across the junction, leading to the formation of a depleted region: in case of a p-i-n diode, the electric field can extend along the whole nominally intrinsic i-region, or only along a part of it, depending on the background impurity concentration, for an assigned *i*-region thickness;

Photocurrent spectroscopy (PCS) and photovoltage spectroscopy (PVS) have been largely employed in the characterization of quantum wells to investigate the optical transitions between quantum confined states, as well as the perpendicular transport of carriers through the structure [22-26]. These processes have a direct influence on the performances of quantum photodevices, such as solid state photomultipliers, high speed optical modulators, quantum cascade lasers etc. In particular, the temperature dependence of the photoelectrical (PE) signals is mainly related to both generation and recombination rate and to the activation of the carrier escape out of the QWs [27-29]. Generally, the transport process involves different physical parameters (carrier transit time, carrier lifetime and carrier mobility) which determine the modelling of quantum devices. In p-i-n structures, where a sequence of undoped QWs is inserted in the intrinsic region, the internal electric field is determined by the alignment of the Fermi levels of the two p- and n-cladding materials. Thus, the carriers photogenerated into the QWs are swept out by the electric field more or less rapidly depending on the competition between drift, diffusion and recombination processes in the structure.

In order to study the photoelectric response of IGPCELL1, both the PC and PV spectra were acquired, exhibiting the features expected from the theory of optical transitions between quantum confined energy states. The line-shape analysis of the spectra allowed to compare nominal to effective geometrical parameters of the structure. In addition, particular attention has been reserved to the analysis of the temperature dependence of PC and PV intensity: the behaviour of both the signals in the range of 30 to 300 K is analyzed by keeping note of the frequency at which the incident light beam intensity is modulated. The differences observed in the temperature dependence of PC and PV, ascribed to a not fully depleted SL region, are discussed accounting for a prominent role of the undepleted region, which strongly limits the photocarrier collection at the electrodes.

5.3.1 Experimental setup

The experimental setup was based on a standard optical table for photoelectrical measurements. The radiation source consisted in a 100 W halogen lamp, set at ~63W (9 V x 7 A) during the acquisition of the spectra. The intensity of the light was modulated by a mechanical chopper operating at a frequency ν_{ch}, ranging in the 13-700 Hz interval. The modulated light beam was then focused into the entrance slit of a SPEX monochromator (0.5 m focal length), with a spectral resolution better than 2 meV, producing a narrow band exciting beam which impinges on the sample. Internal reflections of the light at the several interfaces of the structure are expected to guarantee the illumination of the sample also in the volume under the opaque metallic contact, as it is suggested by the results of photocapacitive investigations of light-induced persistent phenomena, performed in Schottky diodes having contacts of similar size and shape [30]. The sample was kept at a controlled temperature (10-300 K) into a He-closed cycle cryostat, supplied by a temperature controller which guarantees a typical uncertainty in the temperature equal to ±0.1 K.

The induced electrical signals were finally revealed by a lock-in amplifier, using as a reference the TTL signal supplied by the mechanical chopper, and then properly corrected for the spectral response of the experimental set up, recorded by using calibrated Si and PbS photodetectors.

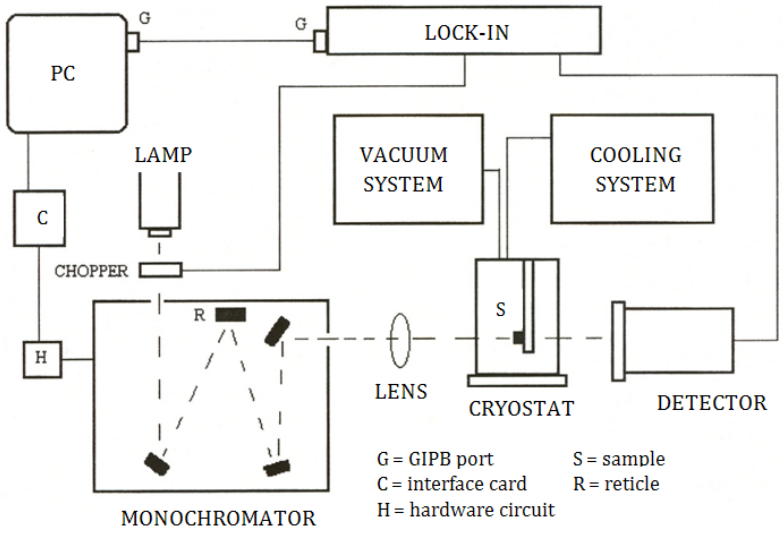

Figure 5.12: Sketch of the photoelectrical apparatus.

5.3.2 The photoelectric signal

At a given temperature, the steady state intensity I_0 of the PC signal, induced by the uniform front illumination of a diode where the depletion layer is fully extending over one side of an asymmetrical planar junction, can be expressed by the simplified formula [24, 27]:

$$I_0 = A \cdot J_0(\lambda) = A \cdot \frac{eP(\lambda)}{hc/\lambda}(1 - R_S)\eta\{1 - \exp[-\alpha(\lambda)W]\} \qquad (5.10)$$

where J_0 is the steady state photocurrent density; A is the area of the junction; $P(\lambda)$ is the incident optical power density at a given λ (for unit area); R_S is the front-surface reflectivity of the sample, whose λ dependence can be generally neglected; $\alpha(\lambda)$ is the absorption coefficient; h and c are the Planck constant and the light speed, respectively; W is the total thickness of the depleted region which can be considered uniformly illuminated, in the spectral region here investigated. It follows that

$1/\alpha(\lambda) >> W$ and consequently $\alpha(\lambda)W << 1$. Assuming negligible any recombination processes within W, the photocurrent density $J_0(\lambda)$ becomes simply proportional to $\alpha(\lambda, T)$ if the factor η is assumed as a constant. Actually, η is the *internal quantum efficiency*, defined as the number of electron-hole pairs generated per absorbed photon; it is nearly equal to unity. The main assumption of this simple approach, which neglects any recombination process within the *W* region, is fairly corrected if the transit time t_t of the excess carriers through *W* is competitive with respect to their recombination time τ, that is for $\tau >> t_t$. Here, τ is determined by the radiative and non-radiative processes; for low dimensional III-V systems it can assume a value generally ranging in the wide interval 10^{-7}-10^{-12} s [31]. The transit time is given by $t_t = W/\mu E$, where μ is the mobility of the excess carriers and E is the electric field across the thickness *W*, where carriers can be swept out. By applying the Einstein's relation $L_d = \sqrt{D\tau} = \sqrt{(K_B T/q)\mu\tau}$, where L_d is the diffusion length of the excess carriers, the condition $\eta \approx 1$, which is satisfied for $\tau >> t_t$, implies that $L_d^2 > (W^2 K_B T/q)/V_b$, where $V_b = EW$ is the built-in voltage across the depleted region. In our case, $W = L_{dep} = 135$ nm, where L_{dep} is the thickness of the depleted region, and V_b resulted of about 1.5 V from capacitance-voltage measurements at RT. Therefore it results $L_d > 10$ nm, which appears a condition reasonably achievable if compared with the width (20 nm) of one well-barrier period of the SL here studied.

In addition, in an ideal p-i-n junction device, at low injection level, the steady state open-circuit photovoltaic signal, V_{PV}, gives information equivalent to the steady state short-circuit photocurrent I_{PC}. In fact, according to the relation $V_{PV}=k_BT/q\times \ln(I_{PC}/I_R+1)$, where I_R is the reverse saturation current of the diode, in the limit of low

illumination intensity (I_{PC}<<I_R), the two photoelectrical signals are expected to be proportional each other through the factor k_BT/qI_R.

5.3.3 Spectral response

The *RT* photocurrent (thick continuous black line) and photovoltage (blue line and symbols) spectra taken as a function of the photon energy, by chopping the light at a frequency ν_{ch} =162 Hz, are shown in Figure 5.13. Here the low energy features are due to the two clearly resolved excitonic transitions between n=1 quantum confined states, related to heavy (hh_1-e_1) and light (lh_1-e_1) holes; the weak broadened knee, visible at intermediate energies (at about 1.55 eV), is attributable to the unresolved second order transitions. At higher energies, the intensity enhances, owing to the InGaP three-dimensional (3D) exciton transition. In order to justify the strong raising up of the PC signal at these wavelengths, it is worth to recall that the total InGaP thickness is much larger than the total GaAs thickness in the SL region and that also carriers photo-generated into the thick InGaP layers within a distance from the depleted region comparable to the diffusion length have high probability to reach the latter before to recombine, so contributing to the signal. Finally, at energies over the InGaP band gap, the strong light absorption in the InGaP front-cladding layer generates carriers too far from the depleted region with respect to their expected diffusion length, and the signal lowers to negligible values. When the temperature is decreased, the intensity of the whole spectrum decreases, as shown in the same figure (thin continuous black line). In particular, the reduction of the signal is stronger at low energy, in the spectral range of the absorption between the quantum confined states.

As concerns the PV data, similar features are exhibited by the RT spectrum, as reported in Figure 5.13 (blue line and symbols); however, in our samples the detection of the whole PV spectrum by a standard lock-in technique, becomes unreliable below T~200 K, owing to a significant change of the phase of the signal during the

measurement. Such unusual behaviour, investigated in depth in the following paragraphs, is related to the peculiar band alignment of these p-i-n junctions, in which the SL region results only partially depleted.

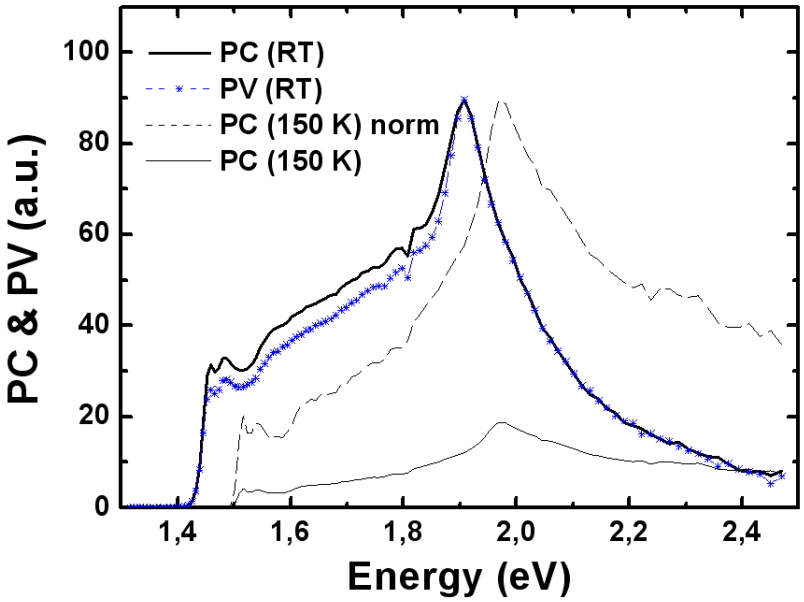

Figure 5.13: Photocurrent (thick continuous black line) and photovoltage (blue line and symbols) spectra taken at RT, in arbitrary units. PC at 150 K (thin continuous black line) is also reported normalized to the RT InGaP peak (dashed black line) to evidence the variation with the temperature of the spectrum shape.

Figures 5.14a and 5.14b, respectively, show PC and PV spectra in the spectral range of the GaAs n=1 excitonic resonances, taken at different temperatures and at fixed modulation frequency of the light (ν_{ch}=162 Hz). A comparison of the two series of spectra shows a weaker temperature dependence of the PC intensity.

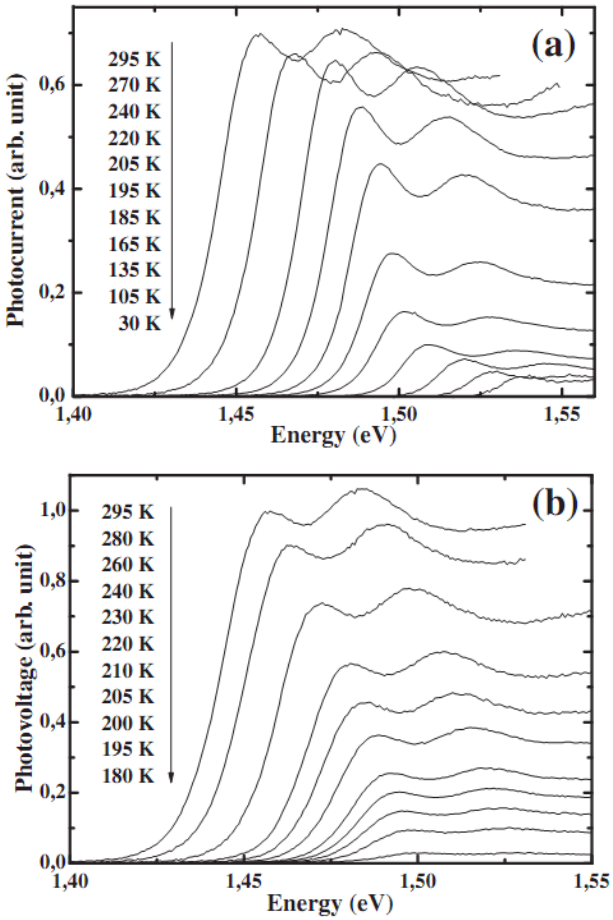

Figure 5.14: Low energy photocurrent (a) and photovoltaic (b) spectra taken at different temperatures and modulation frequency ν_{ch}=162 Hz.

5.3.4 Line-shape analysis

The line-shape of the spectra given in Figure 5.14 can be analysed by applying the approach proposed by Chemla and generally followed for absorption spectra [32, 33]: the hh_1-e_1 and lh_1-e_1 contributions were resolved by assuming the superposition of two gaussian shaped peaks and two Sommerfeld factors, which account for the transitions above the two-dimensional (2D) subband edges (continuum edge), where excitons are

ionized. Figure 5.15 shows an example of the analysis relative to the PC data taken at T=10 K. However, at any temperature, the Gaussian peak representing the hh_1-e_1 exciton transition coincides very well with the experimental one, whereas the experimental peak related to the lh_1-e_1 exciton shifts toward higher energy with respect to its gaussian simulation owing to the superposition of the hh_1-e_1 continuum. The free parameters in the fits were: (i) the energies of two excitonic peaks, (ii) the intensities of excitonic resonance and continuum for the heavy hole exciton, and (iii) the binding energy of the hh_1-e_1 exciton (that is the energy shift between such peak and the relative continuum), assuming the binding energy of the lh_1-e_1 exciton a few meV higher, according to the literature [33]. In addition, we assumed the following constrains: (a) equal widths for the two gaussian curves and (b) $I_{lh1}/I_{hh1}=(1/3)\ (\mu_{lh}/\mu_{hh})$. Here μ_{hh} (μ_{lh}) is the reduced mass of the 2D exciton related to the heavy- (light-) hole.

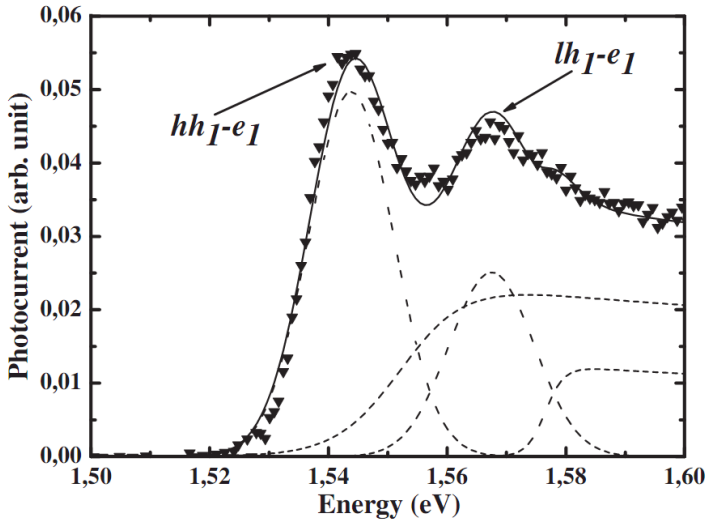

Figure 5.15: Line-shape analysis of the photocurrent spectrum at T=10 K. Symbols: experimental data; continuous line: fit. Each contribution (the resolved excitonic resonances and the continuum contributions of the hh_1–e_1 and lh_1–e_1 transitions) is separately plotted with dashed lines.

The transition energies and the half-width Γ of the hh_1-e_1 peak, resulting from the fit, are reported as a function of the temperature in Figure 5.16. The peaks shift to higher energies as the temperature is decreased, by following the decrease of the GaAs gap, as generally expected. By assuming a thermal broadening due to polar optical phonons, the Γ(T) data were fitted, obtaining an intrinsic half width at half maximum (HWHM) value Γ_0~7 meV, fairly satisfactory with respect to the values currently reported for the InGaP/GaAs QWs system. The experimental and calculated energies of the heavy- and light-hole excitonic transitions were then compared by assuming: (i) the limit of T=0, (ii) parabolic bands, (iii) barrier height consistent with the band offsets previously evaluated in Ref. 16. The experimental energies agree, both in absolute values and in relative separation, if the calculation assumes a 8.5 nm wide rectangular QW. Such an estimated well width is only slightly larger than the nominal one (8 nm) and agrees, within the experimental uncertainty, with the results of a transmission electron microscopy investigation on similar samples [34].

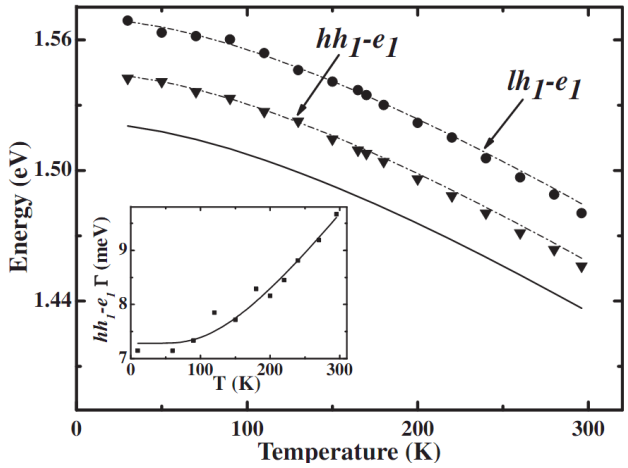

Figure 5.16: Temperature variation of the hh_1–e_1 and lh_1–e_1 peak energy (symbols), compared to the GaAs E_g thermal shrinkage (continuous line). The dashed lines are only guides for the eyes. Insert: T-dependence of the half-width Γ of the gaussian peaks (symbols) and standard fit (line), performed by assuming an inhomogeneous broadening of the peak due to polar optical phonons.

5.3.5 Modulation frequency dependence of PE signals

In a different procedure of the photoelectrical investigation, the PE signals were measured as a function of the modulation frequency of the optical excitation; this investigation is complementary to the AS one (see paragraph 5.2), since it can operate in a considerably lower frequency range, where the AS becomes less reliable. In this context, we measured the isothermal dependence of both the short-circuit PC and the open circuit PV signals on the modulation frequency ν_{ch} of the exciting light, in the 13–700 Hz range. At each temperature, the measurements were taken by changing the chopper frequency step by step, and, at each step, by maximizing the lock-in signal through the phase-shift regulation. Therefore, at each frequency both intensity and phase-shift data were obtained. Before to be focused on the sample, the chopped light beam was tuned, by the monochromator, to the energy of the hh_1-e_1 excitonic resonance depending on the temperature of the experiment. The signal was then corrected by the response of the experimental setup at the proper wavelength. Peculiar frequency dependence behaviours were measured at temperatures within the range 170–200 K, as shown in Figure 5.17, where the data are plotted as a function of the angular frequency $\omega=2\pi\nu_{ch}$. Outside this temperature range, the PC signal exhibits a ω-independent behavior, whereas the PV signal decreases with frequency as $1/\omega$; differently, within the mentioned restricted T-range, peculiar decrease in both the PC and PV signals with the frequency increase are superimposed to the simple trends described above. In additions, a peculiar frequency dependence was observed also for the phase angles measured by the lock-in, as it will be discussed later. However, we notice that this quantity gives the phase shift between the detected signal and the TTL reference signal produced by the chopper and coupled to the lock- in, which differs for an arbitrary constant value φ_0 from the phase shift between the measured photoelectrical signal and the modulated optical signal illuminating the sample.

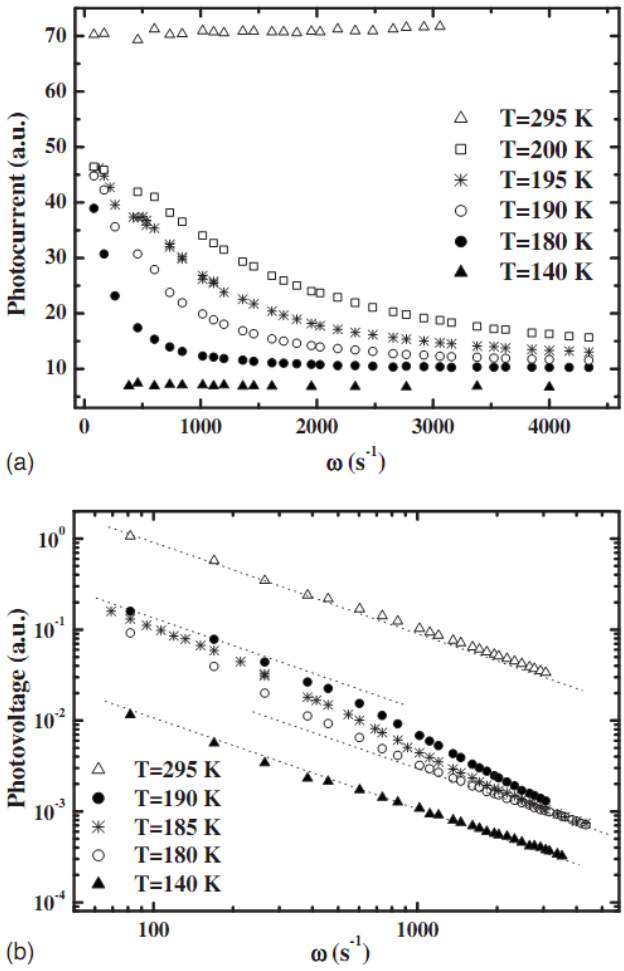

Figure 5.17: PC (a) and PV (b) intensities taken as a function of the chopped light angular frequency, at different temperatures. The dashed lines in (b) follow the $1/\omega$ behavior. Slight anomalies around the 50 Hz frequency have instrumental origin.

PC and PV equivalent circuit analysis

PC

In the discussion of the ω-dependence of the PC and PV intensity, we refer to the equivalent simplified schemes reported in Figure 5.18, by assuming for C_1, C_2, and R the same physical meaning given in the AS measurements. The ideal short-circuit condition implies the connection of the two end points of the equivalent structure shown in Figure 5.8b; the modulated light source is here represented by an ideal alternating current source having amplitude I_0, connected in parallel to the C_1 capacitance, by approximating that only in the depleted region the inner electric field efficiently drives the generated charge carriers toward the contact (cladding) layers. For such an equivalent scheme, we calculate the current I_{PC} flowing in the external branch of the circuit, out of the depleted region, as a function of the angular frequency: it results to be a complex quantity, having amplitude proportional to I_0:

$$I_{PC}(\omega) = I_0 \frac{\sqrt{\omega^2 R^2 C_2^2 + 1}}{\sqrt{\omega^2 R^2 (C_1 + C_2)^2 + 1}} = I_0 f_{PC}(\omega) \qquad (5.11)$$

where $f_{PC}(\omega)$ is a coefficient correcting the photocurrent signal I_0, which depends on the angular frequency of the signal. The phase shift φ_{PC} of the PC with respect to I_0 is given by:

$$\varphi_{PC}(\omega) = \arctan \frac{-\omega R C_1}{\omega^2 R^2 C_2 (C_1 + C_2) + 1} \qquad (5.12)$$

or, if expressed in terms of ϖ,

$$\varphi_{PC}(\omega) = \arctan \frac{-(\omega/\varpi) C_1}{(\omega/\varpi)^2 C_2 + (C_1 + C_2)} \qquad (5.13)$$

In the low frequency limit ($\omega << \varpi$), I_{PC} is expected to display the same amplitude and zero phase shift with respect to I_0, whereas in the high frequency limit ($\omega >> \varpi$),

the PC maintains the same phase of I_0 but reduces its amplitude according to $I_{PC}=I_0C_2/(C_1+C_2)=I_0C_\infty/C_1$. At intermediate frequencies, I_{PC} amplitude varies monotonically between the two mentioned limits, whereas φ_{PC} exhibits an extreme at $\omega_m = \varpi\sqrt{(C_1+C_2)/C_2}$.

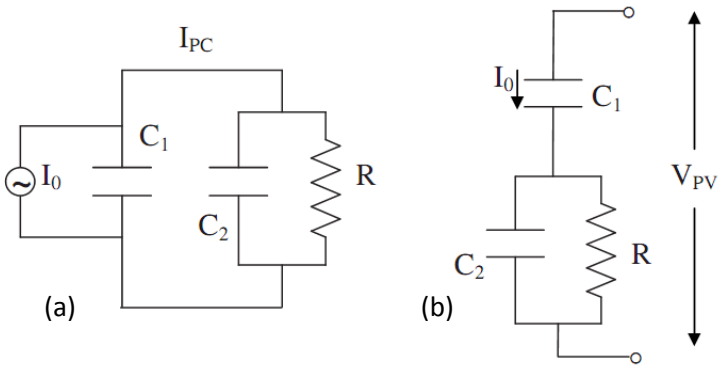

Figure 5.18: Equivalent electrical circuits used in the PC (a) and PV (b) measurements

PV

In the PV experiment, the photoelectrical signal V_{PV} equals the open-circuit voltage drop V_{OC} at the end of the whole structure and is mainly originated by the charges photogenerated in the MQW region, which can undergo the action of the inner electric field. Here a phenomenological description is tentatively given for the PV signal, using the experimental data as a guide. As demonstrated in Ref. 16, the flat band MQW region can be considered as an additional p-type layer, contiguous to the depleted region and working as a capacitance C_2 in parallel to a resistance R. For this reason, it can accumulate charge depending on the time constant RC_2: by modulating the optical excitation at a certain angular frequency ω, this region should behave as a pure resistive layer when $\omega<<1/RC_2$ because, between any light pulse and the subsequent one, the capacitance C_2 is rapidly charged and discharged, so that this

undepleted region appears nearly equipotential during each light pulse. On the other hand, in the opposite limit of $\omega >> 1/RC_2$, the charge state of C_2 has no chance to follow the variations in the light beam amplitude and varies with opposite phase (therefore opposite polarization) than C_1. This picture is consistent with the variation in frequency of the experimental phase shift between the PV signal and the PC pulse; in fact, such a phase shift spreads between $\pm\pi/2$ in the explored ω range; then the frequency at the inflexion point should be related to the time constant RC_2. To quantify these observations, accounting for also the displayed dependence on $1/\omega$ of the PV signal, we suppose the latter to be proportional to the voltage between the depleted region, $V_0(\omega)=-I_0(\omega)/i\omega C_1$, where i is the imaginary unit, I_0 is the modulated current of carriers photogenerated in the depleted region, which acts as an active circuit element, so that the voltage drop at its ends has opposite sign with respect to $I_0(\omega)$. Moreover, the dynamic effect of the undepleted region (represented by the RC_2 circuit) on the voltage detected at the end of the whole structure is accounted for by the phenomenological complex factor $\xi=(1+i\omega RC_2)/[1-i\omega R(C_1-C_2)]$, which is the ratio between the impedance $-1/i\omega C_1$ of the depleted region and the impedance of the whole structure $Z=R/(1+i\omega RC_2)-1/i\omega C_1$, and multiplies $V_0(\omega)$. The dynamic behaviour of the PV signal results then to have an amplitude proportional to the current amplitude I_0, expressed by the formula:

$$V_{PV}(\omega) = I_0 \frac{\sqrt{\omega^2 R^2 C_1^2 + \left(1-\omega^2 R^2 C_2 (C_1 - C_2)\right)^2}}{\omega C_1 \left(\omega^2 R^2 (C_1 - C_2)^2 + 1\right)} = I_0 f_{PV} \quad (5.14)$$

We point out that, in the limit of $\omega << \varpi$, the modulus of the corrective factor ξ is unity and the amplitude of the PV signal is $V_{PV}=I_0$; in the opposite limit of $\omega >> \varpi$, $|\xi|$ is less than unity and $V_{PV}=(I_0/\omega C_1)/[C_2/(C_1 - C_2)]$, according to a non-negligible

effect of the capacitive role of the undepleted region. The phase shift φ_{PV} between the PV signal and the ideal $I_0(\omega)$ current is given by:

$$\varphi_{PV}(\omega) = \arctan\left[-\frac{1}{\omega R C_1} + \frac{\omega R C_2 (C_1 - C_2)}{C_1}\right] \qquad (5.15)$$

φ_{PV} is $-\pi/2$ in the low frequency limit, $+\pi/2$ in the high one, and exhibits an inflexion point at the angular frequency $\omega_{flex} = \sqrt{1/\left[R^2 C_2 (C_1 - C_2)\right]}$ or also $\omega_{flex} = \varpi (C_1 + C_2)/\sqrt{C_2 (C_1 - C_2)}$, if ω_{flex} is written in terms of ϖ, a value comparable to $1/RC_2$, as expected.

Discussion of the results

The experimental data $I_{PC}(\omega)$ and $V_{PV}(\omega)$ were fitted by equations (5.11) and (5.14) using ϖ, C_1, and I_0 as free parameters, whereas C_2 was expressed through C_1=C_0 and C_∞ using the relation:

$$C_2 = \frac{C_0 C_\infty}{C_0 - C_\infty} = \frac{S\varepsilon}{L_{und}} \qquad (5.16)$$

Because C_1, C_2, and R were supposed to have equivalent physical meanings in PV, PC, and AS measurements, the high frequency capacitance was taken equal to C_∞=29.5 pF in all the experiments. To better evidence the behaviour of the photoelectrical (PC and PV) response near the resonance frequency, the $1/I_{PC}$ and $1/(\omega V_{PV})$ experimental data were both plotted as a function of ω, as illustrated in Figure 5.19(a) and 5.20(a), respectively, where continuous lines are the best fitting curves. As appears in Figure 5.19(b), the PC phase curves have always the same sign and exhibit a weak maximum at an angular frequency interpreted as ω_m, at which the

model predicts an extreme for the phase shift $\varphi_{PC}(\omega)$. The PV phase-shift data of Figure 5.20(b) spread from $-\pi/2$ at low frequency to $+\pi/2$ at high frequency, with respect to a value, shifted from zero of $+\pi/6$, which is the phase shift φ_0 between the TTL reference signal and the ideal current I_0, which is assumed to be in phase with the light pulses. The intercepts between the experimental curves and the $\varphi=\pi/6$ line were interpreted as ω_{flex}.

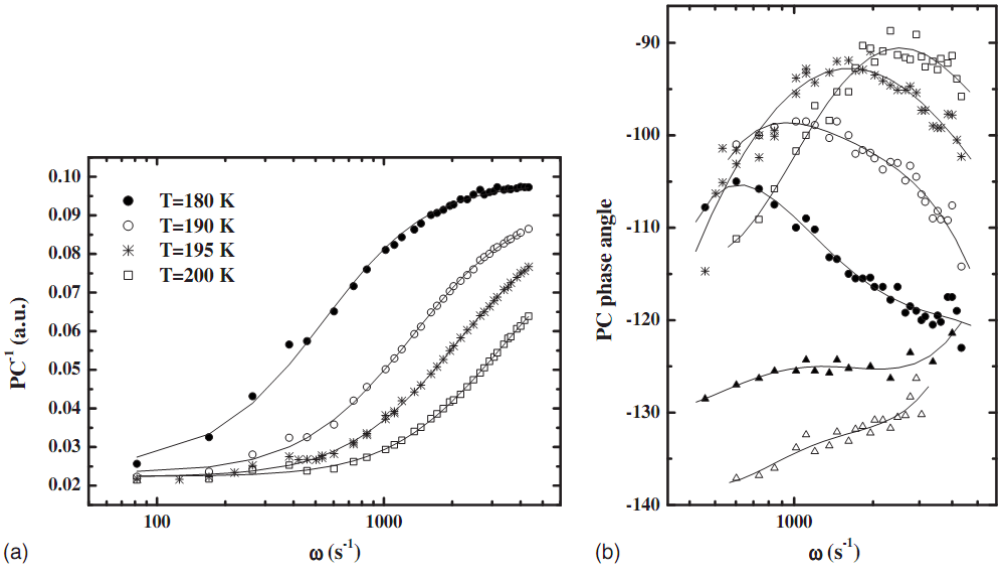

Figure 5.19: (a) 1/PC signal amplitude vs. chopper angular frequency ω (symbols) at different temperatures T, by tuning the exciting light to the 2D hh_1e_1 excitonic transition and best fitting curves (continuous lines); (b) experimental phase shift between the PC signal and the TTL reference vs. ω at different T: the symbols are the same of (a). Moreover, Δ refer to RT and ▲ to T=140 K data; the continuous lines are only guides for the eyes.

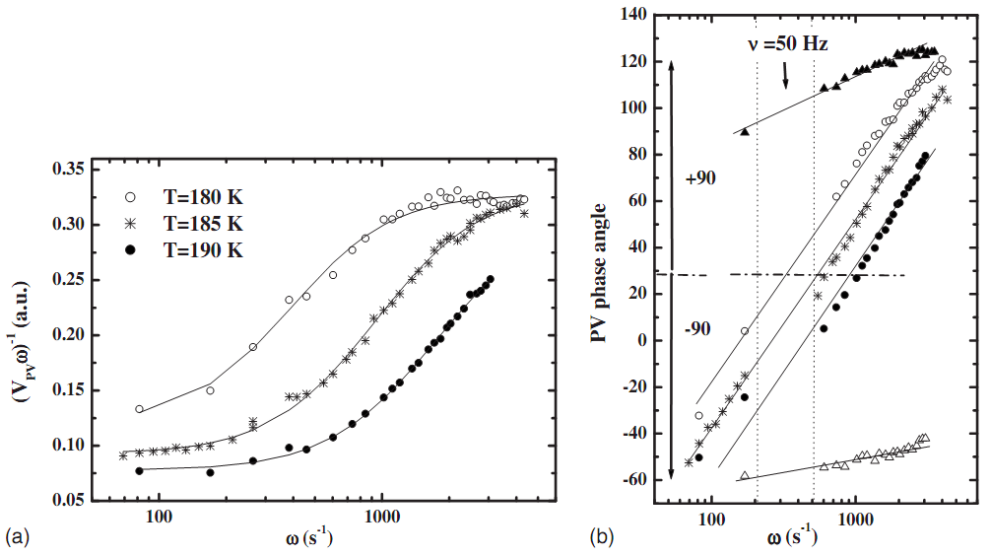

Figure 5.20: (a) Symbols: $(\omega PV)^{-1}$ amplitude as a function of the chopper angular frequency at different temperatures T by tuning the exciting light to the 2D hh_1e_1 excitonic transition; continuous lines: best fitting curves. (b) Experimental phase shift between the PV signal and the TTL reference vs ω at different T: the symbols are the same of (a). Moreover, Δ refer to RT and ▲ to T=140 K data; the continuous lines are only guides for the eyes; data lying between the two dot lines around 50 Hz frequency are excluded due to instrumental anomalies.

As a result of the fit of the $V_{PV}(\omega)$ and $I_{PC}(\omega)$ functions and by using the formulas given for ω_m and ω_{flex} (see data in table 5.2), it was possible to estimate the resonance frequency ϖ for each temperature and to plot $\ln(\varpi/T)$ vs $1/K_BT$ in Figure 5.21: the full and open triangles are related to the ϖ values given by the fitting of the amplitudes of PC and PV signals, while the stars indicate the values obtained by the analysis of the phase-shift data. The *resonance* frequency values obtained by AS are also reported for comparison. The self-consistency of the results confirms that the peculiarities of the PE data are due to the same phenomenon of *resonance* pointed out through the AS measurements, and also reinforces the assumption that capacitances

and resistances defined in this approach represent equivalent physical quantities in all the frameworks. In particular such a conclusion is appropriate for the equivalent resistance *R*, whose temperature dependence dominates the ϖ(T) curve.

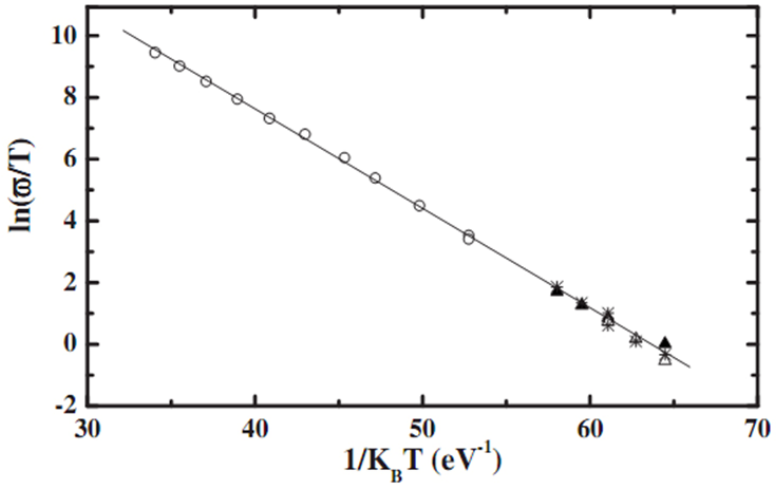

Figure 5.21: ln(ϖ(T)/T) function vs. $(K_BT)^{-1}$. Open circles: AS data; full and open triangles: values obtained by the fitting of PC and PV data, respectively; stars: values obtained by both PC and PV phase-shift data vs. angular frequency, as explained in the text; continuous lines is only a guide for the eyes.

Table 5.2
Additional values of ϖ at different *T*, calculated from the experimental values of ω_{min} and ω_{flex}; the uncertainty on the estimation of the data is less than ±10%. κ is the ratio between ω_{min} (ω_{flex}) and ϖ in PC (PV) measurements.

T (K)	ω_{min} or ω_{flex}	κ	ϖ	Signal
200	2.5×10^3	0.51	1300	PC
195	1.5×10^3	0.5	750	PC
190	1.0×10^3	0.5	530	PC
180	5.2×10^2	0.51	260	PC
190	1.1×10^3	0.33	350	PV
185	6.0×10^2	0.34	200	PV
180	3.7×10^2	0.35	130	PV

Figure 5.22 shows the temperature dependence of the C_1 capacitance, obtained by PE and AS measurements. The wide spread of data here observable evidences that, notwithstanding the same physical meaning, C_1 should not be expected to have the same value in all the experiments; in particular, the data obtained in PV measurements are always higher than the others. This result is consistent with the fact that in PV, rather than PC and AS measurements, the structure is subjected to a weak mean forward bias, which reduces the depleted thickness. However, all the C_1 data exhibit a general tendency to decrease with decreasing temperature. Both the PE and AS data don't exhibit any hysteretic behaviour with the variation of the experimental procedure, thus excluding a non equilibrium occupancy of the permitted energy levels; the reason of the observed behaviour has rather to be searched in the particular temperature dependence of the built-in potential between the *n* and *p* cladding layers: in fact, at the p-side of the p-MQW-n structure, the contact region includes the fraction of superlattice given by the undepleted QWs, where the Fermi level significantly varies with the temperature.

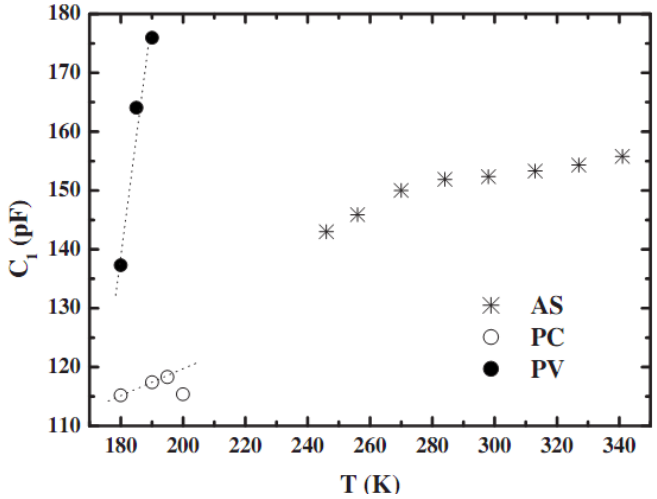

Figure 5.22: Temperature dependence of the capacitance $C_0=C_1$ given by AS measurements (stars), PV (full circles) and PC (open circles) measurements; the dot lines are only guides for the eyes.

A comment on the reliability of the PE data taken at low temperatures, around and below the *resonance* region, is finally dutiful. Concerning the PV signal, we recognized that it is originated by a polarization of the superlattice, driven by a light excitation whose intensity is modulated with variable frequency through a chopper. In such framework both the amplitude and the phase of the PV signal depend on the impedance of the structure and follow its variation with the wavelength of the exciting light λ. As a consequence, differences in the phase-shift φ_{PV} depending on the behaviour of the RC_2 circuit can be expected, with respect to the present case, in particular when the wavelength is decreased enough to cause a strong photon absorption in the front InGaP layer. In fact, in this case, an increase of the generation rate of the excess carriers may induce high injection condition with a consequent variation of the conductance $1/R$ of the flat band MQW region. The value of the *resonance* frequency ϖ is then modified. However, when at the temperature of the experiment the $\omega << \varpi$ condition occurs, the undepleted region behaves as a resistive layer and no significant phase-shift is expected when λ varies: a standard spectroscopic acquisition of the signal can be reliably performed, where the PV intensity is detected as a function of the photon wavelength with a fixed value of the phase during the detection (see Figure 5.13, blue line). On the contrary, when $\omega >> \varpi$ is verified at the temperature of the experiment, the record of a spectrum like the one given in Figure 5.13 becomes unreliable. In the latter case, the spectral variation of the PV intensity can be measured only by changing the photon wavelength step by step, and maximizing the signal at each step (through a phase adjustment). This behaviour has been really observed in the PV spectra below T~200K.

A similar behaviour could be expected, in principle, also in short-circuit configuration; however, the circuit model discussed previously and the experimental results of Figure 5.19(b) suggest that the phase-shift between I_{PC} and I_0 is significant only around the *resonance* condition. Therefore, variations of R with the photon

wavelength can have only weak effects on the phase of the signal, and in a restricted *T*-range, where the peculiar features of the *resonance* appear. The standard spectroscopic acquisition of the PC intensity was then fairly reliable in the whole temperature range.

5.3.6 Temperature dependence of PE signals

The variation with the temperature of the short-circuit (I_{PC}) and open-circuit (V_{PV}) PE signals were separately measured for various modulation frequency of the exciting light (ν_{ch}=13-500 Hz) by following a particular procedure, for each selected modulation frequency: (i) the temperature of the sample was stabilized at a given value, (ii) the wavelength of the exciting light beam was tuned to the energy of the hh_1-e_1 excitonic peak, (iii) the resulting PE signal was maximized by adjusting its phase-shift with respect to the reference signal, (iv) intensity and phase-shift were recorded, with the former corrected by the response of the experimental set up.

The temperature dependence of the PC and PV intensities is shown by their Arrhenius plots drawn in Figure 5.23; here, each curve was normalized to its own RT value, although such a normalization obscures the expected dependence of the PV signal on $1/\nu_{ch}$. Figures 5.24 report the corresponding phase-shift between the measured PE signal and the TTL reference signal.

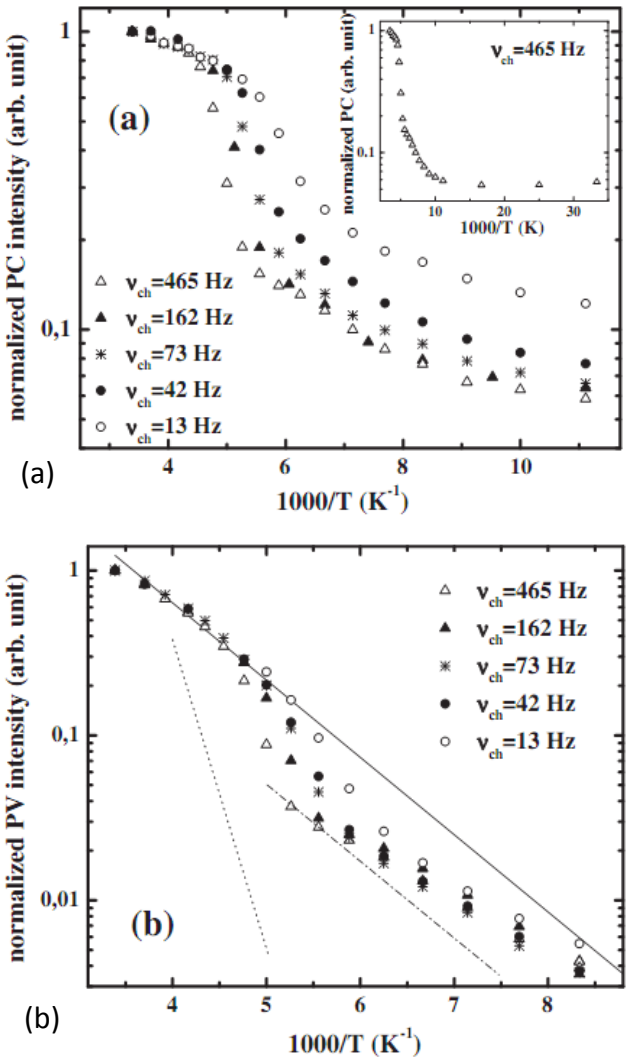

Figure 5.23: (a) Intensity of the PC signal as a function of the temperature T taken at different chopper frequencies ν_{ch}, tuning the energy of the exciting light to the n=1 2D excitonic transition: the data are normalized to the RT value. To evidence the features around T~200 K the data are reported in a restricted range of temperature. Insert: PC data taken at ν_{ch}= 456 Hz in the whole range of temperature explored. (b) PV signal vs. 1000/T in the same conditions of (a); continuous line: probability of thermoionic emission of electrons over the QW barriers, normalized to unity at RT; a dashed-dot line of equal slope is also reported shifted in intensity of a factor ~0.2; dot line: thermal emission rate of *heavy holes* over the barriers in the QW valence band for comparison.

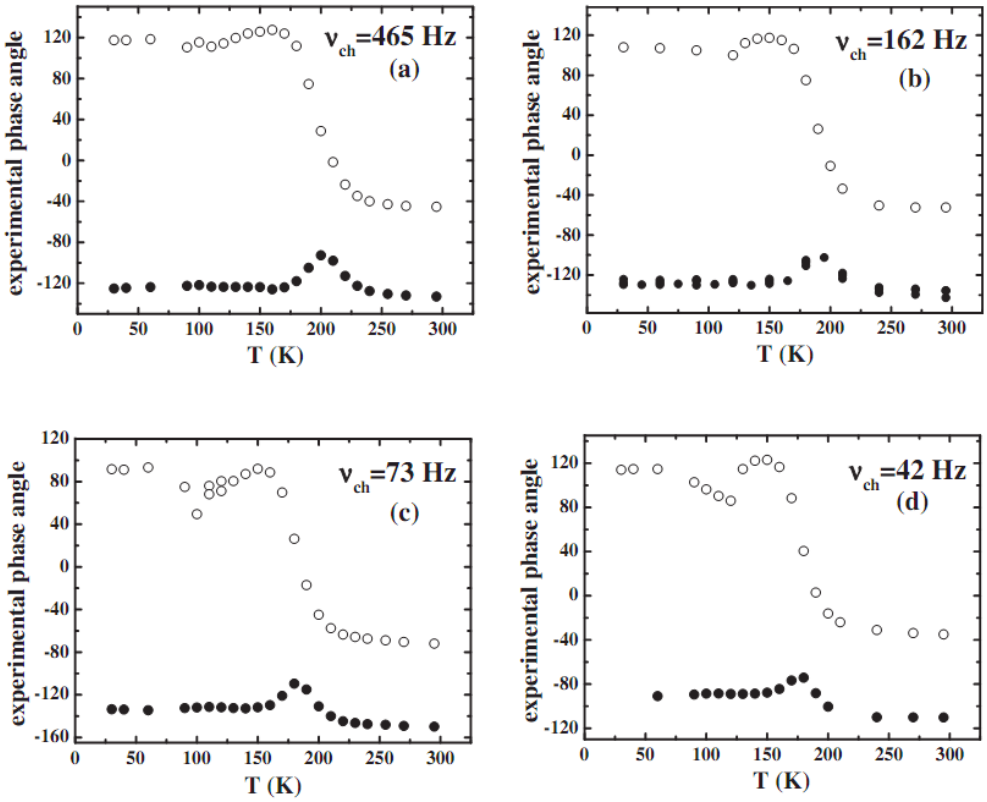

Figure 5.24: Phase angle relative to PC (full circles) and PV (empty circles) signal as a function of the temperature for different frequency of the chopped light: (a) ν_{ch}=456 Hz, (b) ν_{ch}=162 Hz, (c) ν_{ch}=73 Hz, (d) ν_{ch}=42 Hz: at any ν_{ch} the extreme in the PC phase is about at the same temperature T_{res} of the inflexion point in PV phase.

PE intensity at the resonance conditions

The *T*-dependence of the phases shown in Figures 5.24 is the more convincing fingerprint of the crossing of the *resonance*. At the *resonance* frequency, for a constant T, an extreme and an inflexion point in the ω-dependence of the PC and PV phase,

respectively, has been shown (Figures 5.19b and 5.20b), according to the models describing the phenomenon. Alternatively, if the temperature is varied at fixed ν_{ch}, the same features in the phases should be expected at a characteristic temperature T_{res}, at which the *resonance* condition is verified. This behaviour is really observable in the PC and PV phase data of Figure 5.24, so that a set of (T_{res}, ν_{ch}) pairs can be obtained for selected ν_{ch} chopper frequencies. The relationships between ν_{ch} and the corresponding *resonance* angular frequencies are given by the same models and result: $\varpi = 2\pi\pi_{ch}\sqrt{C_2/(C_1+C_2)}$ for PC data, and $\varpi = 2\pi\pi_{ch}\sqrt{C_2(C_1-C_2)/(C_1+C_2)^2}$ for PV data. The so-obtained ϖ frequencies are reported in Table 5.3, resulting in further (T_{res}, ϖ) pairs, which are fitted by the same line of Figure 5.21. The consistency of all the results is evident and supports the interpretation of the model.

Table 5.3

Additional pairs of (T_{res}, ϖ) data obtained by the curves of figures 6.24

T_{res}	ν_{ch}	$\varpi/(2\pi\nu_{ch})$	$(k_B T_{res})^{-1}$	ϖ	$\ln(\varpi/T_{res})$	Signal
182	73	0.5	63.76	229.22	0.231	PC
182	73	0.35	63.76	160.45	-0.126	PV
192	162	0.5	60.44	508.68	0.974	PC
189	162	0.33	61.40	335.73	0.575	PV
179.5	42	0.5	64.65	131.88	-0.308	PC
179.5	42	0.35	64.65	92.32	-0.665	PV
202	465	0.5	57.45	1460.1	1.978	PC
197	465	0.32	58.52	934.46	1.557	PV
166.5	13	0.3	69.70	24.49	-1.917	PV

As concerns the intensity of the PE signals, we focus the attention on the sudden steps appearing at T~170-200 K in the PC and PV data of Figures 5.23, where the intensities reduce abruptly of about a factor 0.2; such a feature appears in a range of

temperature which depends on ν_{ch}, and is placed around the T_{res} value obtained for the corresponding phase angle data. We attribute such steps to the *resonance* condition. With reference to the PC data, we recall the discussion in "PC and PV equivalent circuit analysis" paragraph, where the *T*-behaviour of I_{PC} was interpreted as a superimposition of a monotonic reduction of $I_0(T)$ with the temperature decreasing and a modulation of the signal intensity through the ω-dependent coefficient f_{PC}. However, at temperatures around RT, f_{PC} is expected to be unity because ϖ is much higher than any ω used in the experiment (low frequency limit). On the other hand, at sufficiently low temperatures when ϖ is lower than ω (high frequency limit), such a coefficient is predicted to tend again to a ω-independent value, equal to $C_2/(C_1+C_2)$, lower than unity. By assuming C_1~115 pF and C_2~40 pF, a reduction factor of about 0.25 is calculable for f_{PC} between the two limits, in fair agreement with the reduction of the experimental intensity across the step. Therefore the latter can be interpreted as due to the crossing of the *resonance* condition. Similar considerations can be extended to the PV data, the reducing factor for f_{PV} being in this case $C_2/(C_1-C_2)$ with C_1~160 pF, C_2~35 pF.

We point out the usefulness of our efforts finalized to avoid erroneous or doubtfully interpretations, by trying to separate intrinsic and extrinsic contributions: the data of Figure 5.23a are only apparently similar to other results reported in the literature, where the T-dependence of the PC signal, although qualitatively comparable to the present one, is fully ascribed to the temperature dependence of recombination, escape or tunnelling processes [35].

PE intensity far from the resonance conditions

In the following we will discuss the temperature dependence of the PE intensities far from the *resonance*, that is in the range in which f_{PC} and f_{PV} are ω-independent. We separately consider the different behaviours of PC and PV intensities vs T, at a fixed modulation (chopper) frequency. In these T-ranges the main contribution to the temperature dependence of the signal is expected by the carrier transport through the MQW, and possible recombination processes. The PV signal can be detected till to 80 K if performed step by step (with adjustment of the phase-shift at each step); at lower temperatures it becomes negligible under our experimental conditions. The T-dependent continuous line drawn in Figure 5.23b, which approximate well the high temperature PV behaviour, represents the calculated $P_{th}(T)$ probability (normalized to unity at RT) of the thermoionic *electron* emission from the most confined quantum state within the wells to the continuum of the conduction band (CB) states over the barriers. $P_{th}(T)$ is given by the formula [36]:

$$P_{th}(T) = en_c\sqrt{\frac{K_B T}{2\pi\, m^*}}\exp\left(-\frac{\Delta E_C - E_{hh_1-e_1}}{K_B T}\right), \qquad (5.17)$$

where ΔE_c and $E_{hh_1-e_1}$ are, respectively, the CB offset and the energy of the n=1 confined *electron* state, by assuming a rectangular QW, 8.5 nm wide and having height equal to ΔE_c [16]; m^* and n_c are the electron effective mass and the 2D density of the states in the CB, respectively. The agreement between experimental and calculated data then suggests that the *electron* escape from the QWs can be the process dominating the T-dependence of I_0 above T_{res}, and that possible recombination processes occurring in the depleted region have only negligible effects on such a dependence. We notice that the electron escape is favourite with respect to the hole one, owing to the lower energy barrier for the emission of electrons (about 90 meV, from the n=1 CB quantum level) with respect to holes (about 346 meV, from the n=1

VB quantum level); the trend predicted for the *heavy hole* thermoionic emission over the VB barriers (from the n=1 VB quantum level) is also reported for comparison in Figure 5.23b with a dashed line.

To complete the picture, we finally notice that, at $T < T_{res}$, when f_{PC} becomes again ω-independent, the experimental data are expected to follow the trend $V_{PV}(T) \propto P_{th}(T) C_2 / (C_1 - C_2)$. A rigid shift into a line parallel to the high-T data should be observed for T-independent C_1 and C_2 capacitances, according to the dashed-dot line in Figure 5.23b. Differently, at low T, the experimental data gradually tend to the $P_{th}(T)$ curve. This result is consistent with the progressive reduction of C_1 with T shown in Figure 5.22; in fact, if C_1 diminishes, consequently C_2 enlarges (although C_1 remains greater than C_2) and the ratio $C_2/(C_1 - C_2)$ tends to increase. Such a behaviour also implies a progressive attenuation of the *resonance* step with the decreasing of T_{res}, as effectively observed in the experimental data for decreasing ν_{ch}. The more simple physical interpretation of the latter results should be a gradual increase of the undepleted region with the temperature lowering; however, other features could be accounted for to give a conclusive explanation of this behaviour.

Concerning the PC data of Figure 5.23a, their T-dependence is significantly weaker than the PV one, with a trend which departs (for I_R decreasing with the temperature) from the simple relation $I_{PC}/I_R \sim qV_{PV}/k_BT$ expected for weak illumination (see paragraph 5.3.2). We attribute such a deviation mainly to a different occupancy of possible trap states for the two circuit configurations, which is related to the different band bending in the depleted region. Such a hypothesis is supported by the curves, shown in Figure 5.25, giving the isothermal time evolution of the PV intensity, which are measured starting from the opening of the circuit (switch from PC to PV set-up). Because the time transients were taken by tuning the illumination energy to the hh_1-e_1 exciton transition at each T, in practice, the curves give the isothermal time variation

of the hh_1-e_1 PV peak during the relaxation of the band alignment in the MQW region from the short circuit (PC configuration) to the steady-state open circuit (PV configuration). This is highlighted in the insert of the same figure: here, the PV values taken at the beginning of the time transients exhibit the same temperature dependence of the hh_1-e_1 PC peak (see Figure5.23a), whereas the asymptotic PV values of the time transients have the same *T*-behaviour of the hh_1-e_1 PV steady-state intensity data of Figure5.23b. Each curve was normalized to the proper RT value. In a rough analysis, a phenomenological parameter τ_s can be introduced, defined as the time required to reach the steady-state PV value, taking with care the data in the temperature range $180<T<150$ K where the *resonance* occurs: in the present case τ_s resulted to be nearly inversely proportional to T. We underline that in the explored T-range τ_s is much longer than the RC_2 time constant for the discharge of the C_2 equivalent capacitance, being always $RC_2 << 1$s, therefore the phenomenology should be rather attributed to the presence of traps with a T-dependent slow dynamic. It cannot be denied that such an hypothesis rises a doubt on the possibility to really reach the steady state value of both the PC and PV signals at the lowest temperatures.

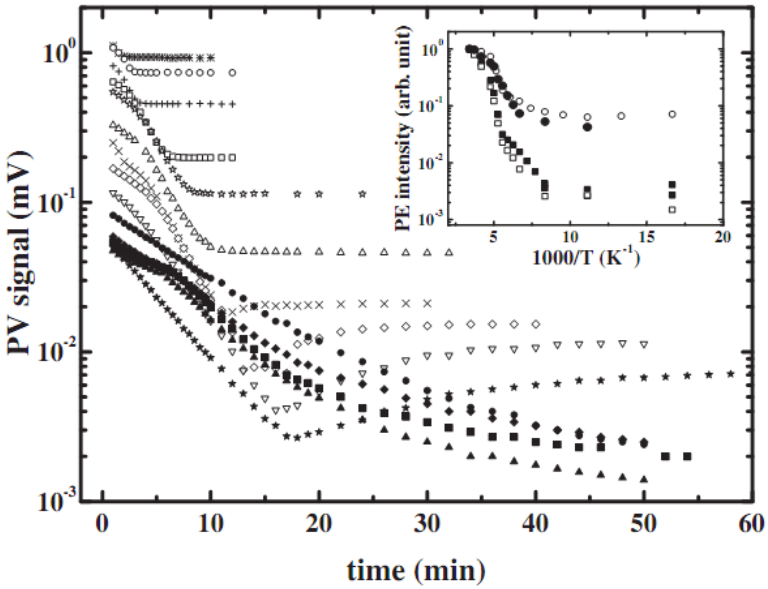

Figure 5.25: Evolution time of the PV signal intensity, taken at different temperatures T and ν_{ch}= 162 Hz, by tuning the chopped exciting light to the n=1 2D hh_1-e_1 excitonic transition. *: T=295K; ○: T=270K; +: T=240K; □: T=210K; ☆: T=200K; Δ: T=190K; ×: T=180K; ◊: T=170K; ∇: T=160K; ★: T=150K; ●: T=120K; ♦: T=90K; ▲: T=60K; ■: T=30K. Insert: T-dependence of the following photoelectrical signals, normalized to the proper RT value: intensity of the PV signal 1 min after the opening of the circuit (●); steady state PC intensity (○); asymptotic value of the PV time transient (■); steady state PV intensity (□).

5.3.7 Conclusions

At the end of paragraph 5.3, it can be useful to briefly summarize the results obtained by the photoelectric spectroscopy measurements.

The spectral photovoltaic and photocurrent responses evidenced excitonic transitions whose energy positions and temperature behaviour are consistent with the theoretical expectations, indicating a good control of the growth process and a high QW structural quality.

By varying the modulation frequency of the optical excitation, it has been demonstrated that the PV and PC signals are influenced by effects due to an uncompleted depletion of the MQW in the p-i-n structure, caused by the unintentional p-type doping of the InGaP layers. The time constant controlling the dynamical response of the structure is related to the thermoionic emission of holes over the QW barriers as in the AS spectroscopy, which revealed a maximum of the isothermal conductance over frequency $G(\omega)/\omega$ curves at the *resonance* frequency ϖ. Therefore, the PE measurements can be considered as complementary to the AS ones, by extending the possibility of a spectroscopic investigation in a different range of frequency. Some sources of misunderstanding in the interpretation of the PC and PV data was pointed out. In this sense, it is necessary to take into account that the PE signals behave as complex physical quantities so that the variations of both the amplitude and the phase of the signals must be monitored carefully, by considering also their dependence on the modulation frequency of the external perturbation.

The temperature dependence of the amplitude of the PE signals, taken by tuning the energy of the exciting light to the n=1 2D heavy-hole excitonic transition, showed an abrupt step in the T-dependence of the PE intensities, placed at the *resonance* condition, and a peculiar behaviour of the phase shift of the signals in respect to the exciting light. The analysis of these behaviours suggested that the PV intensity

is dominated by the thermoionic *electron* emission over the barriers, whereas the PC intensity is significantly influenced by the presence of generation/recombination centres, whose dynamic become slower and slower as the temperature decreases. The presence of such centres have no effects on the frequency response of the equivalent circuit investigated, owing to the characteristic time of their dynamic, very long with respect to the modulation period of the perturbing signals in such experiments. However, the centres can introduce non-equilibrium effects at low temperatures which cause the appearance of features, such as the tendency to decrease of the equivalent capacity C_1 with the temperature, or the flattening of the PC intensity; in particular the latter could be not only ascribable to the prevailing of a transport by tunnelling on the thermoionic emission, as generally supposed in similar structures at low temperatures [37].

References

[1] E. Muñoz, E. Calleja, I. Izpura, F. Garcìa, A.L. Romero, J.L. Sanchez-Rojas, A.L. Powell, J. Castagné, J. Appl. Phys. **73**, 4988 (1993)

[2] J.M. Olson, R.K. Ahrenkiel, D.J. Dunlavy, B. Keyes, A.E. Kibbler, Appl. Phys. Lett. **55**, 1208 (1989)

[3] C.K. Wang, K.H. Yu, W.H. Chiou, C.Y. Chen, H.M. Chuang, W.C. Liu, Solid State Electron. **47**, 19 (2003)

[4] W.S. Lour, J.L. Hsieh, C.Y. Lia, Superlattice Microstr. **24**, 149 (1998)

[5] L.J. Mawst, H. Yang, M. Nesnidal, A. Al-Muhanna, D. Botez, T.A. Vang, F.D. Alvarez, R. Johnson, J. Cryst. Growth **195**, 609 (1998)

[6] N.H. Karam, R.R. King, M. Haddad, J.H. Ermer, H. Yoon, H.L. Cotal, R. Sudharsanan, J.W. Eldredge, K. Edmondson, D.E. Joslin, D.D. Krut, M. Takahashi, W. Nishikawa, M. Gillanders, J. Granata, P. Hebert, B.T. Cavicchi, D.R. Lillington, Solar Energy Mater. Solar Cells **66**, 453 (2001)

[7] T. Nittono, S. Sugitani, F. Hyuga, J. Appl. Phys. **78**, 5387 (1995)

[8] M. Mesrine, J. Massies, E. Vanelle, N. Grandjean, C. Deparis, Appl. Phys. Lett. **71**, 3552 (1997)

[9] S.W. Chiou, C.P. Lee, J.M. Hong, C.W. Chen, Y. Tsou, J. Cryst. Growth **206**, 166 (1999)

[10] M. Begotti, M. Longo, R. Magnanini, A. Parisini, L. Tarricone, C. Bocchi, F. Germini, L. Lazzarini, L. Nasi, M. Geddo, Appl. Surf. Sci. **222**, 423 (2004)

[11] K. Barnham, J. Connolly, P. Griffin, G. Haarpaintner, J. Nelson, E. Tsui, A. Zachariou, J. Osborne, C. Button, G. Hill, M. Hopkinson, M. Pate, J. Roberts, T. Foxon, J. Appl. Phys. **80**, 1201 (1996)

[12] J. Osborne, InGaP/GaAs QuantumWell Solar Cells, Imperial College of Science, Technology and Medicine, London, UK, 1994 (M. Sc. Thesis).

[13] K.W.J. Barnham, B. Braun, J. Nelson, M. Paxman, C. Button, J.S. Roberts, C.T. Foxon, Appl. Phys. Lett. **59**, 135 (1991)

[14] A. Moto, S. Tanaka, T. Tanabe, S. Takagishi, Sol. Energy Mater. Sol. Cells **66**, 585 (2001)

[15] L. Malacký, R. Kudela, M. Morvic, J. Novák, H.H. Wehmann, Mater. Sci. Eng., B **44**, 33 (1997)

[16] C. Ghezzi, R. Magnanini, A. Parisini, L. Tarricone, E. Gombia, and M. Longo, Phys. Rev. B **77**, 125317 (2008)

[17] J. Chen, J.R. Sites, I.L. Spain, M.J. Hafich, G.Y. Robinson, Appl. Phys. Lett. **58**, 744–746 (1991)

[18] G. Arnaud, P. Boring, B. Gil, J.C. Garcia, J.P. Landesman, M. Leroux, Phys. Rev. B **46**, 1886–1888 (1992)

[19] A. Lindell, M. Pessa, A. Salokatve, F. Bernardini, R.M. Nieminen, M. Paalanen, J. Appl. Phys. **82**, 3374–3380 (1997)

[20] O. Dehaese, X. Wallart, O. Schuler, F. Mollot, J. Appl. Phys. **84**, 2127–2132 (1998)

[21] X. Letartre, D. Stievenard, M. Lannoo, D. Lippens, J. Appl. Phys. **68**, 116–119 (1990)

[22] F. Capasso, K. Mohammed, A.Y. Cho, R. Hull, A.L. Hutchinson, Appl. Phys. Lett. **47,** 420 (1985)

[23] R.T. Collins, K. von Klitzing, K. Ploog, Phys. Rev. B **33**, 4378 (1986)

[24] M. Whitehead, G. Parry, K. Woodbridge, P.J. Dobson, G. Duggan, Appl. Phys. Lett. **52**, 345 (1988)

[25] C. Ghezzi, D. Martin, A. Parisini, J.L. Staehli, L. Tarricone, Phys. Status Solidi (B) **152**, 101 (1989)

[26] L. Tarricone, C. Arena, A. Parisini, F. Genova, J. Appl. Phys. **72**, 3578 (1992)

[27] R.P. Leavitt, J.L. Bradshaw, Appl. Phys. Lett. **59**, 2433 (1991)

[28] H.T. Grahn, A. Fischer, K. Ploog, Appl. Phys. Lett. **61**, 2211 (1992)

[29] A.M. Fox, R.G. Ispasoiu, C.T. Foxon, J.E. Cunningham, W. Y. Jan, Appl. Phys. Lett. **63**, 2917 (1993)

[30] C. Ghezzi, E. Gombia, and R. Mosca, J. Appl. Phys. **70**, 215 (1991)

[31] D. Araùjo, M.J. Romero, F. Morier-Genoud, R. Garcìa, Mater. Sci. Eng. B **66**, 151(1999)

[32] D.S. Chemla, D.A.B. Miller, P.W. Smith, A.C. Gossard, W. Wiegmann, IEEE J. Quantum Electron. **20**, 265 (1984)

[33] C. Arena, B. Rotelli, L. Tarricone, Phys. Status Solidi B **185**, 505 (1994)

[34] M. Longo, A. Parisini, L. Tarricone, S. Vantaggio, C. Bocchi, F. Germini, L. Lazzarini, J. Cryst. Growth **311**, 4293 (2009)

[35] K.H. Herrmann, J.W. Tomm, H. Al-Otaibi, Semicond. Sci. Technol. **14**, 293 (1999)

[36] H. Schneider, K. v. Klitzing, Phys. Rev. B **38,** 6160 (1988)

[37] C. Arena, A. Satka, L. Tarricone, Mater. Sci. Technol. **11**, 827(1995)

Chapter 6

GaAs/GaSb tandem structures

6.1 Introduction

In the previous chapter was evidenced that the p-i-n InGaP/GaAs MQW structures grown in our laboratory present a non optimal band alignment, due to an high background doping of the intrinsic InGaP layers, which limit the photovoltaic conversion properties. Since a further time consuming investigation of the MOVPE growth processes has to be performed to try to get over this problem, the development of this structure was temporarily interrupted and in the second part of my PhD research I worked on the development of another structure for photovoltaic applications.

The main aim of this study was to obtain by MOVPE a p-n junction, which should be able to absorb, and efficiently convert, the long wavelength region of the solar spectrum, suitable to represent the bottom junction of a relatively simple monolithic tandem structure. The top junction of this prototype device was already grown in the past in our laboratories and consists of a p-i-n GaAs junction, with a good resulting conversion efficiency. Through the development of a n^{++}-p^{++} GaAs tunnel diode, connecting the bottom junction to the top one, the ultimate purpose of this project is to achieve, within a single MOVPE growth run, a tandem photovoltaic device entirely based on GaAs layers and a substrate (Figure 6.1).

The choice of a proper low energy radiation absorber assumes a great importance for the correct functioning of the overall structure. Low band gap semiconductors are the most suitable compounds for this purpose, considering that their main applications consist in photovoltaic (PV) and thermophotovoltaic (TPV) devices, where thermophotovoltaic energy conversion is the direct conversion process from heat differentials to electricity.

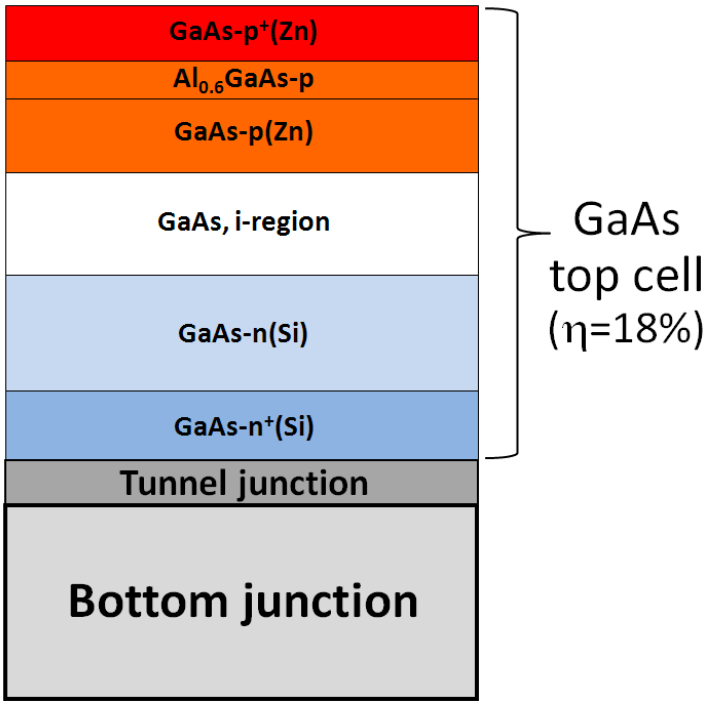

Figure 6.1: Tandem structure with the p-i-n GaAs top cell, already developed in our laboratories with a conversion efficiency η=18%, connected to the bottom junction through a tunnel diode.

6.2 Low band gap materials for PV and TPV

In the last two decades, low-band gap materials have been largely studied for photovoltaic (PV) and thermo-photovoltaic (TPV) devices, because of their capability to absorb long wavelength radiation from sun as well as from low-temperature blackbody emitters. For these purposes the most convenient materials turned out to be germanium, Ge, which has an energy gap E_g=0.66 eV at RT, and gallium antimonide, GaSb, with E_g=0.72 eV at RT.

6.2.1 Germanium

In spite of its rather poor performances as photovoltaic converter, due to the indirect band gap that limits the absorption coefficient of the material, Ge had, and still has, a great importance in the development of monolithic III-V multi-junction devices, wherein it constitutes the bottom cell material (Figure 6.2). The property that makes Ge so essential to these structures is its almost exact lattice match with (In)GaAs and InGaP, which constitute the "middle" and "top" cells, respectively (Figure 6.3); triple junction Ge-based PV devices exhibiting over 40% conversion efficiencies have been recently demonstrated [1].

On the other hand, the relatively broadened absorption edge, typical of indirect band gap materials, and the difficulties encountered in the production of efficient epitaxial Ge p-n junctions, until now, make necessary the employment, in these multi-layer devices, of thick Ge substrates, rather than thin Ge epitaxial layers grown on cheaper virtual substrates.

Moreover, Ge has a lower band gap than the optimal value (~1 eV) in monolithic devices. When integrated in a multi-junction system with InGaP and GaAs upper layers, in fact, Ge has a very large absorption spectrum, between 1.42 and 0.66 eV at

RT, producing an higher current compared with the other sub-cells: since the latter are electrically series-connected, the overcurrent produced in the bottom cell is not exploited because the overall short-circuit current (I_{SC}) is limited to the value generated by the intermediate GaAs sub-cell, which absorbs radiation between 1.9 and 1.42 eV. At the same time, the contribution of the Ge bottom cell to the global open circuit voltage (V_{OC}) is limited by the low E_g value.

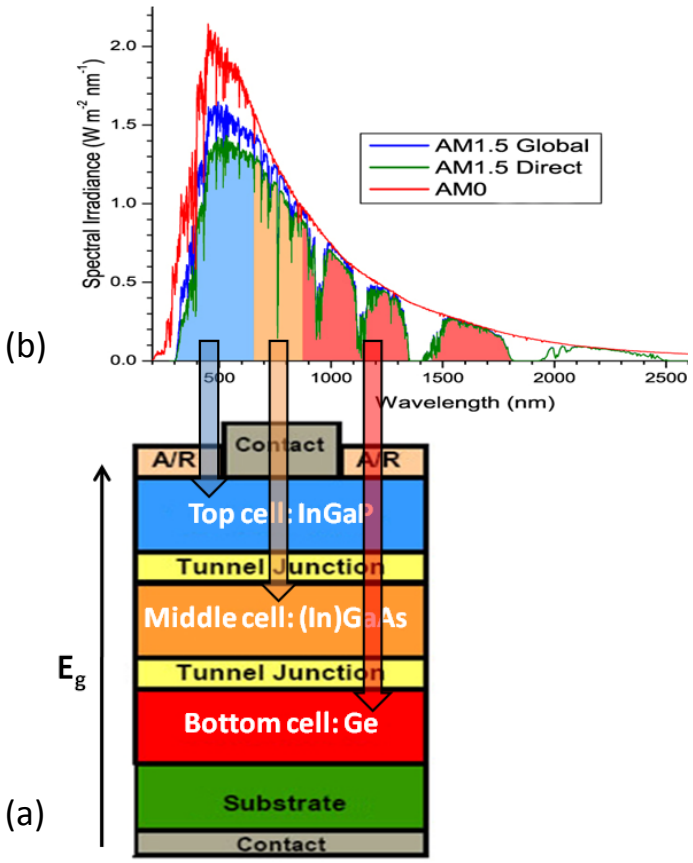

Figure 6.2: Typical structure of multi-junction solar cells (a) and the solar spectrum divided into the absorption range of each sub-cell (b)

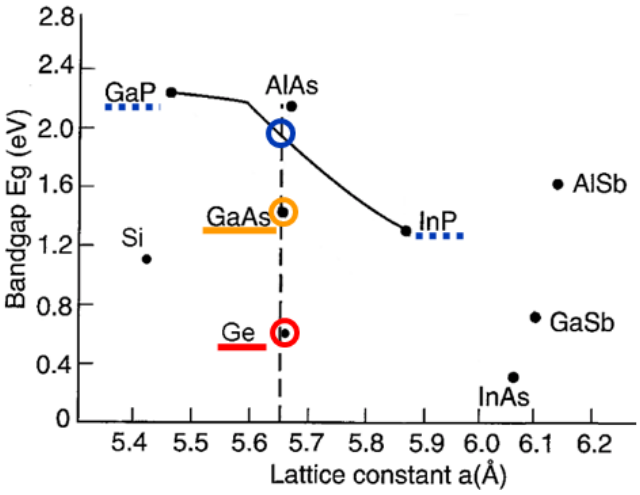

Figure 6.3: Band gap vs. lattice constant values of the most employed semiconductors in PV. The nearly perfect lattice match of Ge, GaAs and InGaP is evidenced.

6.2.2 Gallium Antimonide

GaSb, unlike Ge, shows superior optical absorption properties, due to its direct band gap that makes it an ideal absorber for infrared radiation, leading to an increase in light conversion efficiency. The latter is also enhanced by the higher V_{OC} values, due to the larger E_g, subjected to a minor drop under concentrated light. GaSb-based PV applications started at the beginning of 1990s, when GaSb/GaAs mechanically stacked solar cells, were realized. These devices consist in two electrically independent solar cell, positioned one over the other, in order to optimize the absorption of the incident radiation (Figure 6.4). GaAs and GaSb represent the ideal materials for the top and the bottom cell, respectively, leading to conversion efficiencies of ~30% [2]. These devices, although they allowed to overcome the limitations due to the current matching of multi-junction devices, didn't achieve a relevant market share because

they need complex electric interconnections and two expensive monocrystalline substrates.

At the present time, GaSb-based compounds appear as the most suitable solution for TPV applications. The best-established GaSb TPV devices have a quite simple design (Figure 6.5), based on p-n homo-junctions obtained by a low cost technology, during which the diffusion of Zn into a n-type GaSb substrate (Te-doped) is performed from a Zn vapor over-pressure, in a "pseudo-closed" box at T ~ 450° C [3]. These structures present good conversion efficiencies: η=~8% at AM1.5 and η=~28% with a 2000K black body emitter radiation, against η=~5-6% and η=~16% values relative to the Ge-based devices. Other methods have been investigated to form GaSb p-n junctions, such as the spin coating of the diffusive species compounds [4] and epitaxial growth of GaSb layers [5], but without a significant increase in the conversion efficiency.

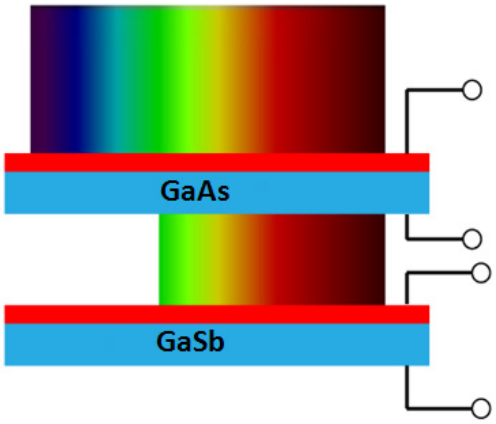

Figure 6.4: GaAs/GaSb mechanically stacked solar cell structure. The two cells are optically in series, but electrically independent.

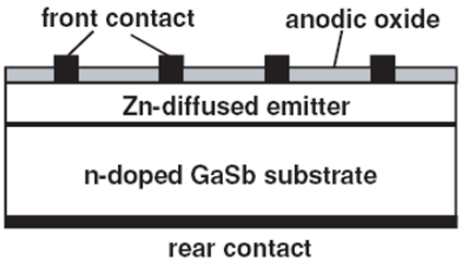

Figure 6.5: Typical GaSb TPV device structure, obtained by Zn-vapor phase diffusion in n-doped GaSb substrates.

6.3 GaSb: physical properties, applications and Hall analysis

Thanks to its potential superior photovoltaic properties in respect to Ge, we employed GaSb as bottom junction material to develop our tandem structure, even if this compound presents two main limits: a high cost of the monocrystalline substrates (~300 $ for 2" wafers) and a large lattice misfit with GaAs (7.8%), which constitutes the top p-i-n junction.

The first one does not represent a very constraining parameter in this preliminary step of the research, which has to be still considered a feasibility study of a new semiconductor structure for photovoltaic applications and does not contemplate the production of finished devices. In a second step of the research, it will be considered the possible replacement of the bulk GaSb junction with an epitaxial one, grown on cheaper monocrystalline wafers or virtual substrates. Having said that, it is useful to point out that the price of the substrates is due to the fact that only a small market exists for GaSb wafers [6]. However, as Fraas et al. pointed out [7], "the real cost of a semiconductor chip is not the material costs but the processing cost'. In fact, they calculated that, for a higher market volume of 1MW, the wafer costs could be reduced by a factor of 20 from the current point of view.

Coming to the second problem relative to GaSb, that is the non-optimal lattice matching with GaAs, it is certainly more crucial, because it could hinder the obtainment of a MOVPE grown structure with good electrical properties, although the peculiar design of our tandem configuration, and in particular of the GaSb bottom junction, should make this problem not so relevant, as discussed later, in paragraph 6.4.

GaSb has a zincblend crystal structure, with a lattice parameter a = 6.0959 Å, and a narrow direct band gap, equal to 0.725eV at RT [8] and 0.810eV at 2K [9]. The melting point, equal to 710° C, is quite low if compared to other III-V

semiconductors. This represents a significant parameter to be taken into account, especially during the epitaxial growths: the good structural quality, in fact, can be compromised by high temperatures, for instance because of Sb evaporation.

6.3.1 Band structure

The band structure of GaSb is particularly interesting (Figure 6.6). The absolute valence band (VB) maximum is at the point Γ, at the centre of the Brillouin zone, wherein two degenerate bands coexist. This degeneracy is resolved at wave-vectors k≠0 through the formation of two bands with the corresponding effective mass values of m_{hh}=0.2197m_0 and m_{lh}=0.0478m_0 for heavy and light holes, respectively (in parabolic approximation). The absolute minimum of the conduction band (CB) is at Γ, characterized by a small effective mass, and therefore a small effective density of the states, while other secondary non isotropic minima lie in proximity of the points L and X of the Brillouin zone, along the (111) and (100) crystallographic directions, respectively. The energy separation between Γ and L minima is quite low, even if the values reported in the literature spread from 40 meV [10] to almost 100 meV [11]. The narrow value of E_Γ-E_L, as well as the fact that the density of the states in the L-valley is much greater than in the absolute CB minimum, induce a lot of electrons to occupy the L-valleys at RT and, in heavily doped samples ($n>10^{17}$ cm^{-3}), also at low temperature, giving rise to mixed conduction effects. The X-minima are, on the other hand, 300-400 meV far from the Γ-minimum: as a consequence, its contribution to the conduction process is remarkable only under hydrostatic pressure, when the occupation density of the X-valley become significant. Owing to the small effective mass, the non parabolicity effects in the Γ valley are significant also for relatively low doping levels and this makes difficult the determination of the electron effective mass

in Γ. The most commonly accepted value for electrons in the minimum of the band is $0.042m_0$, which implies a density of the states equal to $4.2\times10^{13}T^{3/2}$ cm^{-3}. Such a low effective mass leads to a very high theoretical electron mobility: taking into account only the optical polar phonon scattering, a RT mobility of ~4400 cm^{2}V^{-1}s^{-1} was calculated [12], which, among the III-V semiconductors, is lower than only indium arsenide and indium antimonide. On the other hand, electrons in the L-valley have a very low mobility, owing to a high effective mass, comparable, if not even higher, than that of the holes in the valence band.

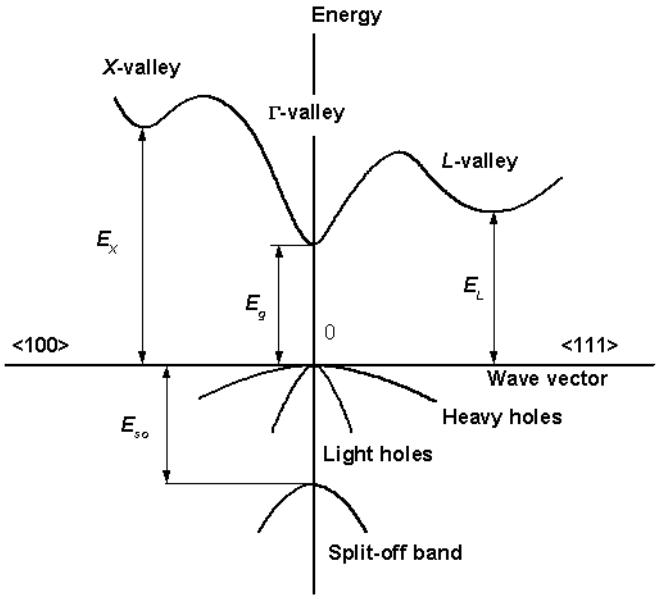

Figure 6.6: GaSb band structure.

6.3.2 Doping

Unintentionally doped GaSb results p-type, with a residual acceptor concentration of 1.5×10^{17} cm^{-3} in bulk material. The origin of this defect is attributed to a stoichiometric defect of Sb: the Sb-vacancy sites are occupied by Ga atoms, producing the antisite defects Ga_{Sb} [13]. The dependence of the p-concentration value on the growth technique confirm this explanation: by molecular beam epitaxy (MBE), in fact, it's possible to reduce the intrinsic acceptor concentration to 1×10^{16} cm^{-3}, a magnitude order lower than with Czochralski growth. Even lower hole density have been obtained, but beyond a certain limit the decrease of holes in the valence band comes with a decrease in the mobility values, meaning that the defect is compensated rather than deleted.

As for the doping of GaSb, a wide set of elements can be used. For p-doping, Zn and Be give good results, allowing to obtain hole densities of 1×10^{18} - 1×10^{19} cm^{-3} in a controlled way. For this purpose, it's possible to employ also some IV group elements, as Sn and Ge, which mainly tend to occupy the Sb-vacancies. This mechanism is probably due to the larger covalent radius of Sb (1.36 Å) than that of Ga (1.26 Å). Si has an amphoteric doping behavior in GaSb and represents the most used dopant in the MBE growth of highly compensated layers.

To obtain n-doped GaSb, Te (Se) and S are usually used. The first produces a very shallow donor level, with a concentration level ranging between 5×10^{16} and 1×10^{18} cm^{-3}, while the latter forms a much deeper donor level, ~60 meV at Γ (Figure 6.7). Because the p-background doping level must be overcame to obtain n-type conductivity, the net donor density in GaSb cannot be lower than a few 10^{16} cm^{-3}, which is a value higher than the critical density for the Mott transition predicted for a shallow hydrogenic donor. Te-doped GaSb, in particular, always exhibits metallic behaviour.

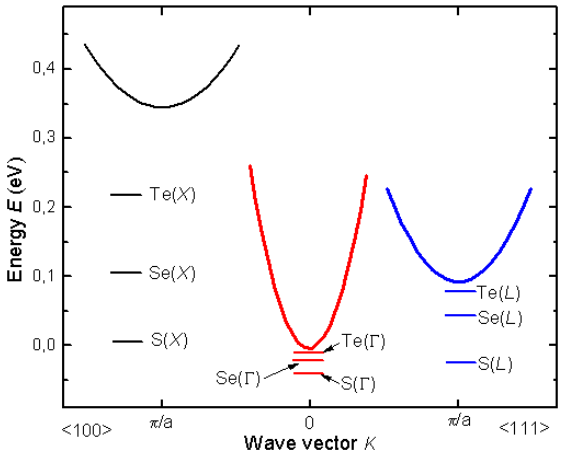

Figure 6.7: Diagram of group VI donor states in GaSb.

6.3.3 Fields of interest

The study of Sb-based compound, and in particular of GaSb, has gained in importance in last years thanks to their remarkable potentialities both in the application and research field.

In the technological application field, GaSb, with a direct band gap that implies band to band transitions at 1.72 μm wavelength at RT, is the ideal candidate for the production of opto-electronic devices working in the third window of traditional quartz optical fibres (λ=1.5-1.6 μm), in which absorption and emission can be easily tuned (Figure 6.8). In this context, the AlGaSb/AlSb heterostructure, showing a reduced lattice misfit (~0.6%), led to the realization of double-heterostructure lasers whose emission is tuned in the transparent window exploiting the confinement effect of the quantum wells on the electronic levels energy [14]. Devices that can operate at the wavelength of ~4 μm, where fluoride glasses optical fibres show a two or three times lower attenuation than traditional ones, have an even higher importance (Figure 6.9); GaInAsSb can be obtained with a band gap equivalent to the interval 1.8-4.1 μm

and a narrow lattice misfit with GaSb that make it an ideal active layer in this spectral region [15].

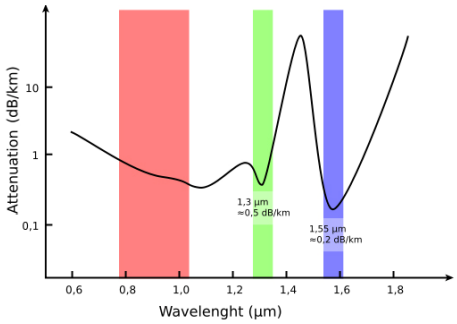

Figure 6.8: First (red), second (green) and third (blue) transmission windows in standard optical fiber.

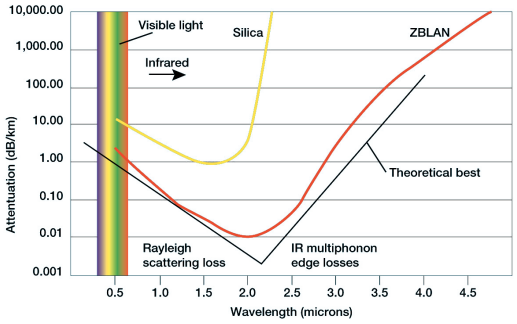

Figure 6.9: Light attenuation by silica and fluoride (ZBLAN) glasses.

Also in the photodetector field, the AlGaSb/GaSb structure, operating between 1.3 and 1.6 μm, is very effective [16].

On the other hand, GaSb does not present strong qualities for high-speed electronic devices, since its electron mobility is not very high, in spite of the low electron effective mass in the absolute minimum of CB. This is due to the low energy difference between Γ and L minima, which causes significant intervalley scattering phenomena. In this field GaSb is employed as substrate or non-active part of the heterostructures. For example, negative differential resistance devices were developed with the InAs/GaSb structure: an high carrier density was achieved in the InAs wells, since the top of the GaSb VB has an energy higher than the minimum of the InAs CB, causing an electron transfer from the first to the latter [17].

As for the basic research, GaSb represents a model system for more than one field. One of these is the DX centre phenomenology. The DX centre is a point defect introduced by donor impurities, which presents, in addition to the usual substitutional

configuration, also a distorted configuration. The ground state connected with the latter is much more localized than that of the usual hydrogen-like levels and is commonly indicated as DX centre. This results to be hooked on the L minima and, therefore, in the compounds where the latter is not too far from the absolute minimum, it lies into the forbidden band gap, controlling the electrical properties of the semiconductor. The main part of the studies on this centre have been performed on GaAs under hydrostatic pressure, to make the L minima to get closer to Γ, and on $Al_xGa_{1-x}As$, where for $x>0.22$ the DX centre enters the band gap. In the first case, all the complications related to working at high pressure are present, while, in the second one, dealing with a ternary compound, alloy disorder effects and different configuration of first- and second-neighbours around the impurity occur. All these problems are avoided by working with S-doped GaSb (sulphur is the only dopant by which the DX centre has been revealed in GaSb), because this is a binary compound that does not require high pressure measurements, since the L minima of CB is particularly near to the absolute minimum.

As for the study of strained structures, a model system is represented by the GaSb/AlSb structure, by which is possible to investigate the influence of the elastic deformations on the electronic states of quantum wells and superlattices. In fact, the lattice misfit of this heterostructure (~0.6%) is considered to be ideal for this purpose, since it allows a good control of the lattice deformation without the issues related to the composition control of ternary compounds.

6.3.4 Hall measurements in Te-doped GaSb substrates

The n(Te)-doped GaSb substrates employed for the realization of the bottom p-n junction were characterized by Hall effect measurements. The carrier concentration values, reported in Figure 6.10 in function of the temperature, show an unusual behaviour, essentially related to the overcoming of the critical density for the Mott transition, mentioned before. At low temperature, the apparent electron concentration remains nearly constant until ~35 K, where it starts to decrease quickly with the temperature rising. This trend can be easily explained by considering the peculiar band structure of the material, and, in particular, the proximity of the L minima to the absolute Γ minimum of the CB. Because the Te impurities are high enough in density to induce the Mott transition, they are fully ionized at any temperature, therefore it is not the overall number of conduction electrons that varies with temperature, but their distribution between the two minima, Γ and L: at the lowest temperatures the electron populates only the Γ minimum, but as the temperature increases, some electrons move to the higher energy minima, giving rise to mixed conduction, the more significant the higher is the temperature. The conductivity in L valleys, in fact, increases with the temperature, notwithstanding the lower mobility, thanks to the higher density of the states in respect to Γ valley, which resulted in a rapidly increasing occupancy. The mixed conduction effects, in conclusions, makes the Hall electron density only apparently lower than the drift one.

At the lowest temperatures the Fermi level enter into the Γ valley and defines the highest populated energy states, as predicted by the Fermi-Dirac statistics for a degenerate electron gas: for electron concentrations of a few 10^{17} cm^{-3}, the low-T Fermi level assesses significantly below the L valley states, which, for a low enough thermal energy K_BT, are almost not populated. As a consequence, the electron concentration measured in this temperature range corresponds to the net N_D-N_A

value of not compensated donors present in the sample: given that the as-grown GaSb is p-type, with a native defect concentration of 1.5×10^{17} cm^{-3}, these latter can be assumed to be present also in n-doped samples, where they act as compensating impurities.

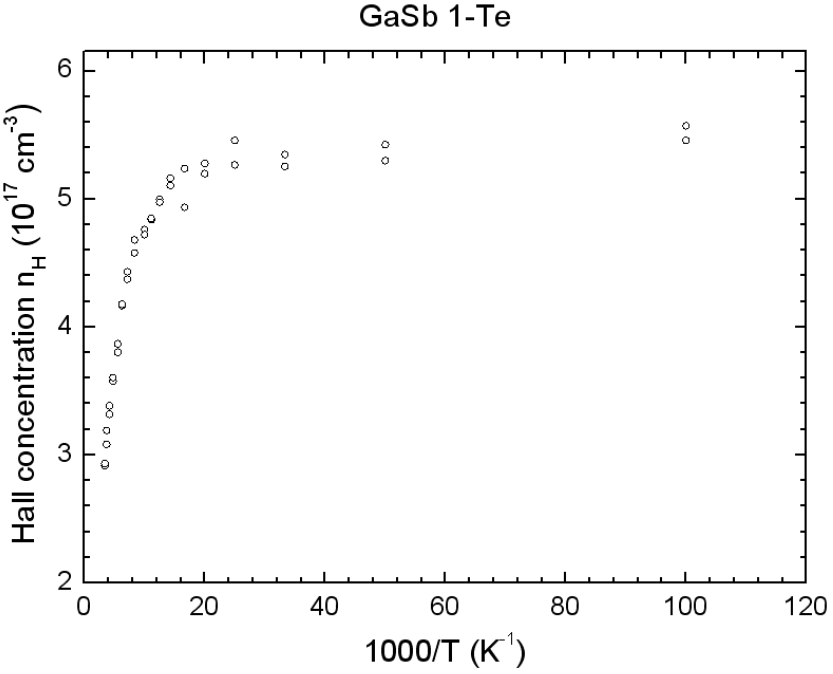

Figure 6.10: Hall electron concentration vs. temperature of the GaSb Te-doped substrate named "GaSb 1-Te".

The dependence of the mobility on the temperature, shown in Figure 6.11, is coherent with the explanation given for the concentration trend. At low temperature the mobility values are virtually independent of the temperature, as expected for a degenerate electron gas, while at higher temperature, after a weak maximum at ~100 K, they show a very significant decrease, which is not entirely ascribable to the polar optical phonon scattering, but it is also influenced by mixed conduction effects.

In particular, the temperature-independent mobility trend is shown in the same temperature interval by which all the electrons are in the absolute minimum: given the high donor concentration, in fact, the mobility remains virtually constant. It is well known that with the increase in the concentration of the ionized impurities, and therefore of the conduction electrons, the typical peak in electron mobility, due to the ionized impurity scattering, gets weaker and weaker until it fades, because of the shield effect of the electrons that limits the efficiency of this scattering mechanism.

On the other hand, the temperature interval during which mobility decreases, corresponds to the occupation of a second valley (the L valley) whose electrons has a higher effective mass that those in Γ (and therefore a lower mobility). This fact has two effects on the mobility values: firstly, the standard mobility calculation is not correct anymore, since mobility does not simply correspond to the inverse of the product between the resistivity and the Hall coefficient. Furthermore, due to the low energy difference between the CB minima, the intervalley scattering, which involves a real mobility decrease, is also relevant.

As for the presence of the maximum in the mobility trend, it cannot be easily interpreted. The most suitable explanation is that it is caused by the variation of the Hall factor r_H, defined as $\langle\tau^2\rangle/\langle\tau\rangle^2$ for each scattering mechanism, having mean scattering time $\langle\tau\rangle$: the mobility, in fact, changes from ~4600 $cm^2V^{-1}s^{-1}$, in the plateau, to ~5300 $cm^2V^{-1}s^{-1}$, in the maximum, with a ~10% variation, which is consistent with the corrections usually made by r_H. Another explanation could be that the peak is due to the decrease of the electron effective mass in the absolute minimum, which is known to be not exactly parabolic, given by the energy variation of the Fermi level in it.

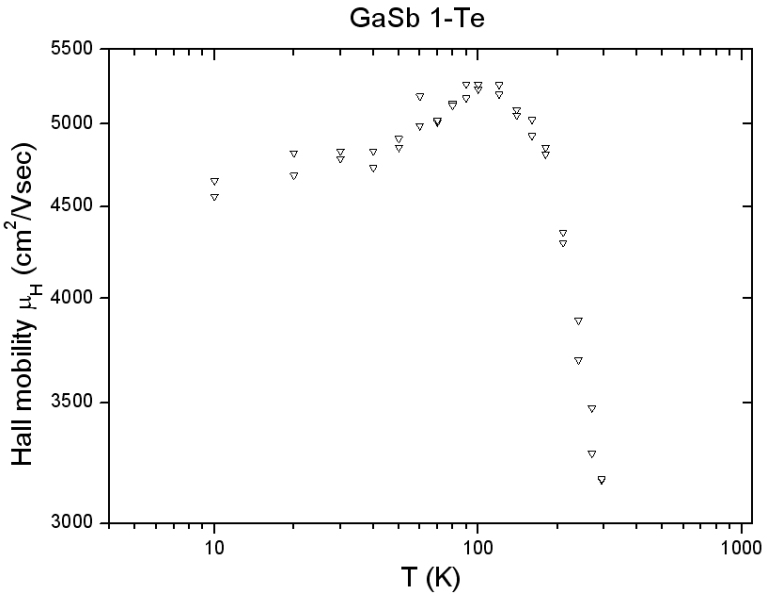

Figure 6.11: Hall electron mobility vs. temperature of the GaSb Te-doped substrate named "GaSb 1-Te".

6.4 GaSb bottom junction

In order to achieve the bottom junction of the whole tandem structure, we deposited by MOVPE a ~500 nm thick p^{++}(Zn)-GaAs layer on n(Te)-doped GaSb substrates: thanks to the growth process, which acts as a real annealing treatment (T=600° C, t=15 min), the interdiffusion of Zn from GaAs towards GaSb forms a buried GaSb p-n homojunction (Figure 6.12). The resulting GaAs layer is characterized by an almost complete strain-relaxation, since its critical thickness on GaSb, due to a lattice misfit of 7.8%, is only ~10 nm: beyond this limit, the elastic energy accumulated in the growing layer to adapt its lattice parameter to the substrate one, is released through the formation of misfit dislocations. The GaAs layer is therefore expected to be ready for the re-growth of a n^{++}-p^{++} GaAs tunnel diode, interconnecting the GaSb junction with the p-i-n GaAs top cell.

Both different Zn doping levels, from 1×10^{19} to 1×10^{20} cm^{-3} (measured by Hall effect on equivalent GaAs layers grown on GaAs S.I. substrates), and time-temperature annealing values, from 0 to 4 hours and from 600° to 660°C, were investigated in order to control the depth of the junction, which has a relevant role in controlling the collection of light-generated carriers. The GaAs/GaSb interface is, in fact, thought to be a particularly defected region, due to the significant misfit between the two materials, and, therefore, a main recombination site for electrons and holes. For an effective collection of photogenerated carrier is therefore necessary that the effective junction plane is sufficiently (more than a diffusion length) far from the metallurgical interface.

The GaAs/GaSb samples were characterized by electrical (dark and light I-V) and SIMS (Secondary ion mass spectrometry) measurements.

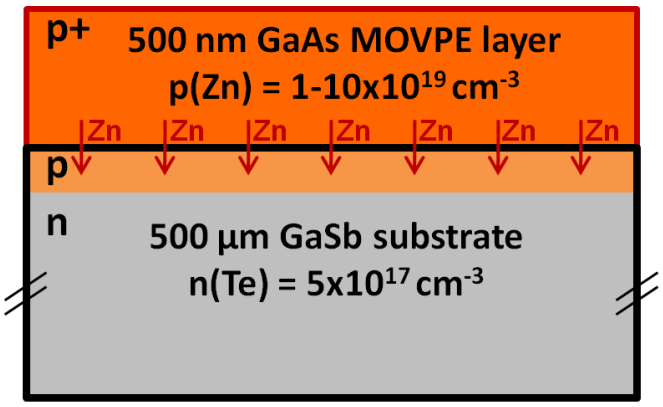

Figure 6.12: GaAs/GaSb sample structure, composed by a Zn-doped GaAs layer deposited on n-GaSb substrate. The Zn interdifussion, highlighted by red arrows, forms the buried p-n junction in GaSb.

6.4.1 GaAs growth on GaSb

Lattice-mismatched GaSb-on-GaAs heterojunctions have been deeply investigated in the recent past thanks to a considerable interest for III-Sb electronic and optoelectronic devices on GaAs substrates such as midwave infrared lasers, detectors and transistors [18 Chap. 8, p. 260, 19]. On the contrary, GaAs-on-GaSb structures are virtually absent from the literature, except for a single work that analyzes the formation of interfacial misfit (IMF) array in GaAs deposited by MBE on GaSb substrates, as briefly reported below [20].

In this work, by Huang *et al.*, the tensile IMF resulted to have an atomic structure, initiated by a single layer of As (001) atoms bonded to the underlying Ga (001) atomic layer, similar to compressive strain GaSb-on-GaAs system. The strain relief was achieved by a skipped As–Ga bond every 13 lattice sites. However, in contrast to the nonreactive nature of the Sb atoms at the GaAs surface, the IMF formation at the tensile GaAs-on-GaSb interface is more complex since the As_2 specie reacts aggressively with the GaSb surface during an As_2 soak. This reactivity forms nanoscale highly crystallographic pits and makes a reconstructed As layer on the GaSb surface difficult to establish. Different As soak times (60, 10 and 0 s), prior to the growth of GaAs layer, were investigated to find the best conditions to obtain a high quality GaAs layer. Cross-sectional and plan-view TEM investigation showed that as the soak time decreases the number and the dimension of the nanoscale pits on the GaSb surface also decrease. At the same time, the threading dislocation density in GaAs epilayer reduces from ~1×10^9 defects/cm^2 to ~3×10^6 defects/cm^2. The resulting GaAs bulk material was both strain-free and highly crystalline.

Apart from this single exception, the lack of literature data, relating to the GaAs-on-GaSb growth, gives to our work an intrinsic degree of novelty.

6.4.2 Experimental procedures

The growth of heavily Zn-doped GaAs single layers was performed by a horizontal low-pressure MOVPE Aixtron reactor (model AIX200 RD) with a single wafer rotating susceptor. The metal-organic precursors were terbutylarsine (TBAs) and trimethylgallium (TMGa) for the V and III group elements, respectively, and dimethylzinc (DMZn) as p-doping source, while palladium-purified H_2 worked as carrier gas. The substrates were 2" (100) Te-doped GaSb wafers with a n-doping level of ~5.5×10^{17} cm^{-3}, obtained by low temperature Hall effect measurements (see Figure 6.10), which were cleaned in HCl for 1 min and then rinsed in isopropanol and dried in blowing nitrogen to reduce the native oxide formation. Once in the reactor, the substrates were heated to 600°C for 5 min under hydrogen atmosphere to desorb any remaining surface oxide. The growth was carried out at a total pressure of 50 mbar and a total gas flow of 6.8 l/min, through the simultaneous switching of TBAs, TMGa and DMZn; the TMGa partial pressure was fixed at 5.6×10^{-3} mbar, at a fixed V/III ratio of 26, and the Zn/Ga partial pressure ratio was varied in the range of 6.3×10^{-3} to 1.0. Typical growth rates of 2.1 μm/h led to ~450 nm thick GaAs layers at a fixed growth temperature (T_g) of 600°C.

In order to perform electrical and photoelectrical I-V characterizations, AuZn dots (400 μm in diameter) and AuGeNi were deposited by a thermal evaporation system, obtaining front and back ohmic contacts, respectively. To minimize the contact resistivity of AuGeNi, the effects of different annealing temperature were investigated, according to issues reported in the literature on the fabrication of low-resistivity ohmic contact to n-type GaSb, due to the surface Fermi level pinning close to the valence band [21]. Figure 6.13 shows the I-V curves relative to AuGeNi contacts on GaSb annealed for 2 min at different temperatures in a reductive atmosphere (N_2-5%H_2): the best contact quality is obtained at 300° C. The same low-resistivity

characteristic was obtained at lower annealing temperature (200-250° C) if some μm of GaSb were chemically etched by a 2 min attack with H_2SO_4:H_2O_2:H_2O 5:1:1 solution: in this way, the most Sb-rich part of GaSb, formed due to the high Sb diffusivity at the MOVPE process temperatures (600° C), is removed and AuGeNi can optimally diffuse into the substrate. This last procedure was adopted in our processing methodology.

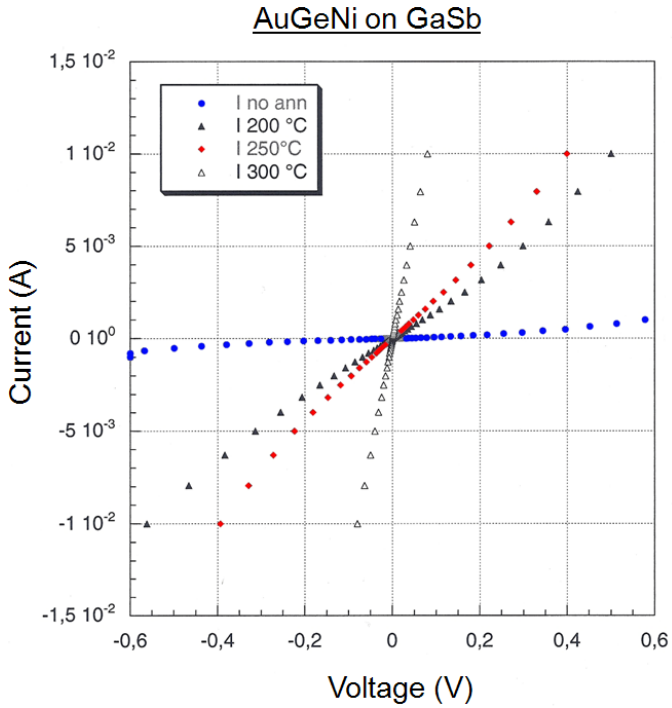

Figure 6.13: I-V curves relative to AuGeNi back ohmic contact on GaSb at different annealing temperatures. The lowest resistivity condition is obtained at 300° C. The same result is obtained at lower temperature (200-250° C) if some μm from the back of GaSb were removed through a chemical etching.

Mesa structures, 500 μm in diameter and ~3.5 μm deep, concentric to the AuZn dots, were created by a two-stage chemical etching based on $C_6H_8O_7$:H_2O:H_2O_2 5:5:1 and H_2SO_4:H_2O:H_2O_2 5:1:1 solutions for the GaAs and GaSb attack, respectively. Citric acid ($C_6H_8O_7$) provides a very selective attack, with etching rates of 2513 Å/min for GaAs and 7 Å/min for GaSb.

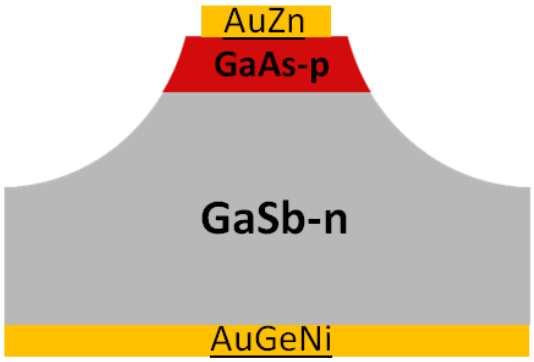

Figure 6.14: Mesa structures, obtained by photo-litographic techniques and chemical etching, for the electrical characterization of the samples. AuZn and AuGeNi form ohmic contacts on p-GaAs and n-GaSb, respectively.

Secondary ion mass spectrometry (SIMS) depth profiles, performed by Prof. Andrea Gasparotto at the Physics Department of the University of Padova, were obtained with a CAMECA IMS4f instrument, using a 5.5 keV Cs^+ primary beam and detecting $ZnCs^+$ and $TeCs^+$ molecular species as secondary ions. The primary beam was rastered on a 200x200 μm^2 square area and secondary ions were collected from a 60 μm diameter circular area at the crater centre to avoid crater edge effects. The quantification of the Zn signal in the GaAs layer was obtained by means of a Zn implanted certified standard sample measured in the same experimental conditions, whereas the Te signal was converted in a concentration profile by assuming the nominal concentration in the GaSb bulk side.

6.4.3 Dark I-V characterization

From I-V measurements the GaAs/GaSb samples turned out to be highly in-plane homogeneous, since every single mesa diode gave pretty much the same characteristics. The dark I-V curves relative to 1×10^{19}, 7×10^{19} and 1×10^{20} cm^{-3} Zn-doped GaAs layers are reported in Figure 6.15, showing good rectifying properties (rectification ratio up to 4 orders of magnitude at 0.4 V) suggesting that the p-n junction was electrically active. Moreover, the achievement of the same I-V characteristics in samples where the GaAs layer was totally removed, permitted to confirm that: i) the p-n junction was located in the GaSb substrate, ii) an homo-junction in GaSb was likely obtained by the diffusion of zinc into the substrate.

It can also be noted that the rectification ratio of the junction increases by lowering the Zn doping levels, thanks to the higher forward current. Diode ideality factors resulted to be ~1.1 in samples with Zn concentration of 1×10^{19} and 7×10^{19} cm^{-3}, and ~1.7 in samples with 1×10^{20} cm^{-3} Zn doping level.

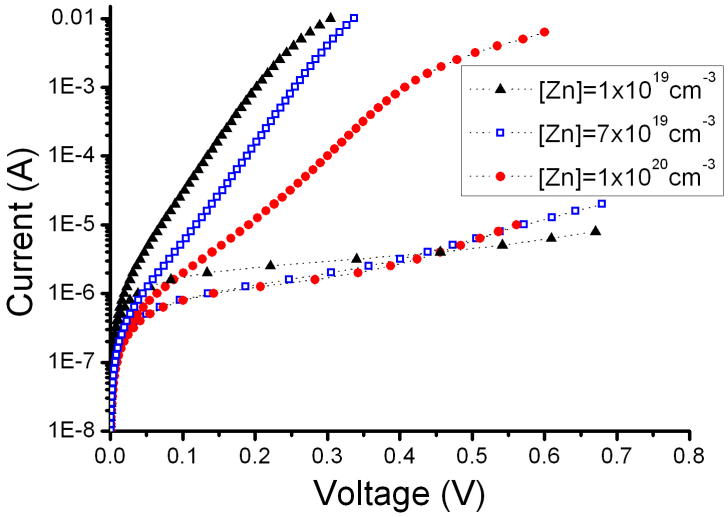

Figure 6.15: I-V curves of p-GaAs/n-GaSb mesa junctions. Forward (symbols) and reverse (symbols + line) characteristics of 1×10^{19} cm^{-3} (full black triangles), 7×10^{19} cm^{-3} (empty blue squares) and 1×10^{20} cm^{-3} (full red circles) Zn-doped samples.

6.4.4 SIMS characterization

Since Zn diffusion through GaSb is of fundamental importance for these structures, especially regarding the light conversion properties, they where characterized also by secondary ion mass spectroscopy (SIMS). Figure 6.16 shows the Zn and Te profiles in GaAs (on the left) and GaSb (on the right) at different Zn doping levels of GaAs layers: a quite low penetration depth of Zn in GaSb is evident if the Zn profile is observed in relation to the Te one. By considering a negligible diffusion of Te in GaAs, both the profiles relative to the same samples are translated to superimpose the Te signal, in order to compare the different Zn diffusion of each sample. The resulting graph is reported in Figure 6.17, where the GaAs/GaSb interface zone is enlarged: the penetration depth of Zn in GaSb varies from 50 to 100 nm with growing Zn

concentrations. These values are quite limited, especially if compared with those obtained by the common diffusion methods from a Zn vapor over-pressure, applied in the realization of TPV devices [22]. An example of the large diffusion depth obtained by this method is reported in figure 6.18: at a temperature of 450° C an annealing of 5 minutes is sufficient to push Zn 0.5 μm deep in GaSb and by extending the annealing time the diffusion depth increases even more.

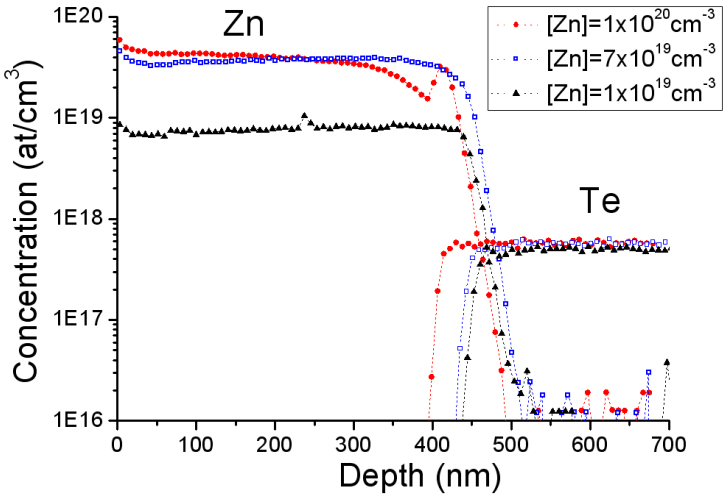

Figure 6.16: Zn and Te SIMS profiles in 1×10^{19} cm^{-3} (full black triangles), 7×10^{19} cm^{-3} (empty blue squares) and 1×10^{20} cm^{-3} (full red circles) Zn-doped samples. The origin of the x-axis represents the GaAs surface and the x values increase going towards GaSb.

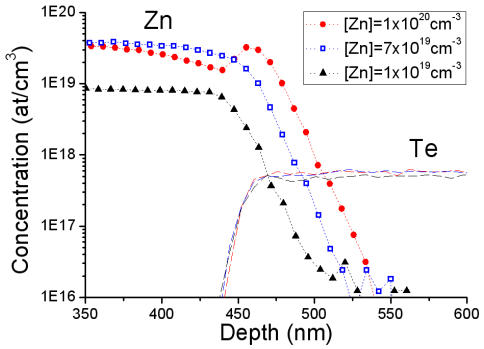

Figure 6.17: Detail of Zn and Te SIMS profiles in the depth zone of the GaAs/GaSb interface. The penetration depth of Zn in GaSb varies from 50 to 100 nm.

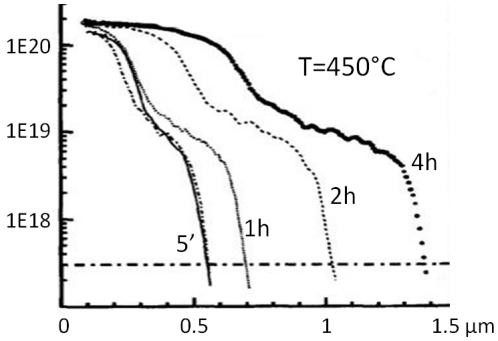

Figure 6.18: SIMS profiles, obtained by Bett *et al.* [22], relative to the Zn diffusion in GaSb achieved through the annealing of a GaSb substrate in a "pseudo-closed box" with a Zn vapour over-pressure at 450° C, for 4 different times. The higher diffusion depth in respect to our method is evident.

In order to further investigate the diffusion mechanisms, samples with a Zn doping level of 1×10^{20} cm^{-3} were annealed at 600°C for 0, 2, 4 h and at 630 and 660°C for 2 h in H_2 atmosphere, within the MOVPE reactor chamber. The SIMS analysis of these samples, shown in Figure 6.19, revealed that neither temperature nor time of annealing considerably affects the Zn diffusion depth. At the same time, no changes in both light and dark I-V characteristics were observed. The only difference in SIMS profile concerns the height of the Zn concentration peak in correspondence to the GaSb surface: as the annealing proceeds, the peak tends to decrease turning into a knee in the concentration profile.

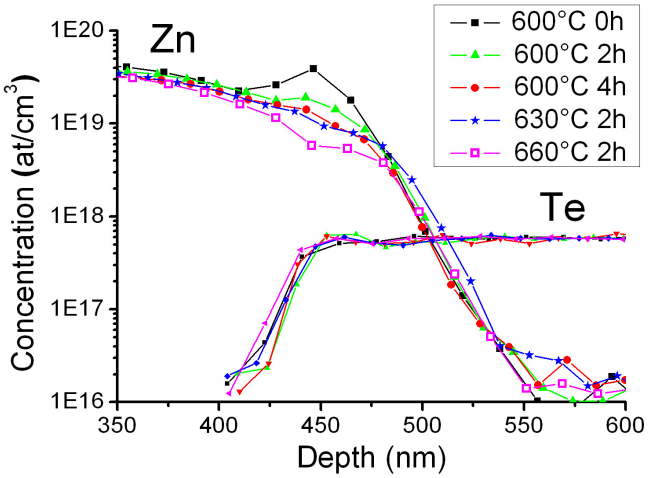

Figure 6.19: Detail of Zn and Te SIMS profiles in 1×10^{20} cm^{-3} Zn-doped samples annealed at different time and temperature.

The overall limited Zn diffusion with respect to the results of Ref. [22] could have several possible explanations. In the traditional "pseudo-closed box" system an extremely high density of Zn atoms from vapour phase comes constantly in contact with the surface of GaSb and then diffuse through it, mainly through interstitial sites. In the present work, on the contrary, a relatively low amount of Zn is involved in the diffusion process, since only the atoms from a few nm thick GaAs layer, close to the metallurgical interface, tend to migrate towards the substrate. Moreover, Zn mainly occupies substitutional sites in GaAs, since Hall effect and electrochemical capacitance voltage (ECV) profile measurements demonstrate that carrier concentration virtually coincides with the atom concentration obtained by SIMS profiles. As is expectable, and also well known in the literature, the diffusion coefficient of substitutional species is negligible if compared with the interstitial ones [23]. In addition, it should not be ruled out a contribution of the misfit dislocations, which most presumably are concentrated along the GaAs/GaSb interface: the line defects, which usually lie parallel to the surface of the sample [24], could act as a

barrier for Zn movement, slowing down the diffusion process. To support this last hypothesis, an accurate structural analysis of the interfacial region between GaAs and GaSb is in progress. This study is expected to be also useful to propose a realistic interpretative model to explain electrical measurements such as I-V curves.

6.4.5 Light response with solar simulator

The response to light of the samples turned out to be quite encouraging. The open circuit voltage increased with Zn doping levels in GaAs, while short circuit current was virtually independent of Zn concentration.

In order to obtain more reliable PV data than those obtained with small area mesa structures, proper 7×7 mm^2 prototype devices were manufactured, with the deposition of a suitable grid top-contact and a chemical etching of the sample borders in order to limit leakage currents. The so-obtained square samples, with an active area of ~0.3 cm^2, were then attached and electrically contacted to an opportune copper plate where the electrical contacts are obtained (Figure 6.20).

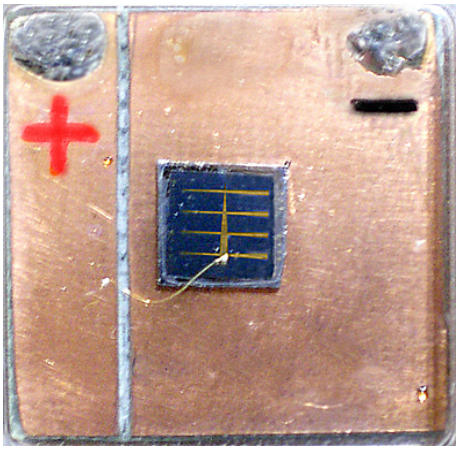

Figure 6.20: 7×7 mm^2 prototype device mounted on a copper plate, where the electrical contacts are obtained.

The light I-V characteristics of the samples were measured with a solar simulator emitting 770 W/m² at AM1.5. The curves relative to 1×10^{19}, 7×10^{19} and 1×10^{20} cm^{-3} Zn-doped GaAs layers are reported in Figure 6.21. The best results, obtained by the sample with the highest Zn concentration, were: V_{OC}=200 mV, J_{SC}=25 mA/cm² (corrected to an incident light power of 1000 W/m²), FF=0.37. The first two data are not too far from the best literature values of 350 mV and 35 mA/cm². The fill factor, on the other hand, is exactly the half of the current best results (FF=0.70) limiting the conversion efficiency η to ~1.8%. This denotes a not yet optimized design of the junction and, maybe, a limiting effect of the contact quality.

Probably the low Zn diffusion in the substrate forms a p-type GaSb layer that is too thin to provide a sufficiently high lifetime of the photocarriers, which are supposed to recombine preferentially at the defected GaAs/GaSb interface.

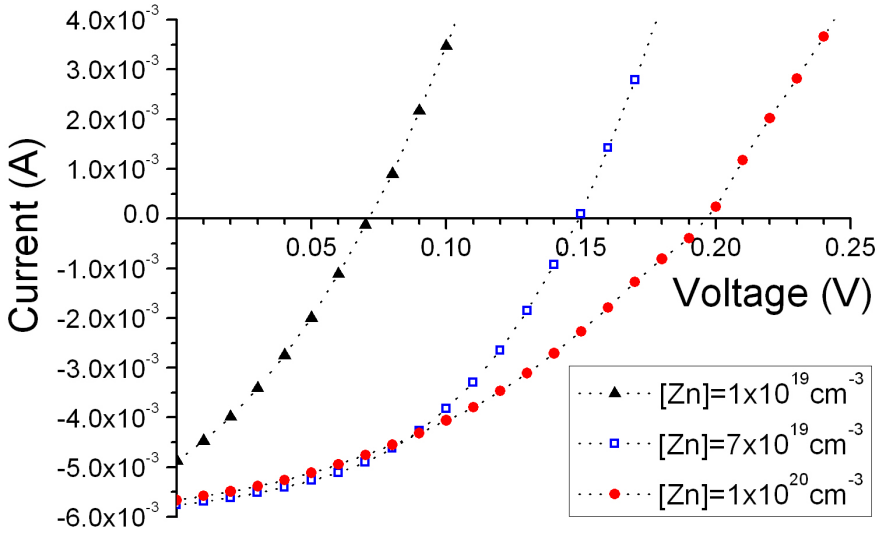

Figure 6.21: Light I-V characteristics of 7x7 mm² samples obtained with a solar simulator emitting 770 W/m² at AM1.5. It can be observed that the open circuit voltage increases with Zn doping levels in GaAs, while the short circuit current is virtually independent of Zn concentration.

6.4.6 Effective diffusion length extracted from light I-V curves

By following the model proposed by Taretto *et al.* in Ref. 25, which allows to extract the minority carrier effective diffusion length (L_{eff}) from some solar cell parameters, the analysis of the V_{OC} and J_{SC} values permitted to estimate L_{eff} in our GaAs/GaSb structures. The main concepts of this model are briefly reported below.

In photovoltaic materials, the bulk minority carrier diffusion length L constitutes one of the most important figure of merit, but in completed solar cells an effective diffusion length L_{eff}, which includes additional, device specific parameters, must be considered. For example, cells prepared with monocrystalline semiconductors have an effective diffusion length $L_{eff}(L, S)$ that depends on the bulk recombination length L and the recombination velocity S at the contacts. The value of L_{eff} is usually obtained from the analysis of internal quantum-efficiency (IQE) measurements [26], but this procedure requires an exact knowledge of the light absorption and reflection in the particular cell under study, which are not always available or easy to be measured. This deficit makes the IQE analysis rather intricate.

The model of Ref. 25 analyzes the current (J)/voltage (V) equation of p-n solar cells and yields an analytical dependence between L_{eff}, J_{SC}, V_{OC}, and the doping level N_A in the base, which considers recombination in the neutral regions as well as in the space-charge region. By solving this equation for L_{eff}, and using the resulting equation it's possible to determine $L_{eff}(V_{OC}, J_{SC}, N_A)$, with an accuracy of 35%, from J_{SC}, V_{OC}, and N_A, which are much more easily accessible than an IQE spectrum of the device.

The starting point for the obtainment of the final $L_{eff}(V_{OC}, J_{SC}, N_A)$ equation is the two-diode model for p-n solar cells (see paragraph 2.3.7), which models the solar cell as a current source connected in parallel with two diodes representing the recombination in the space charge region SCR and in the neutral regions (Figure 6.22).

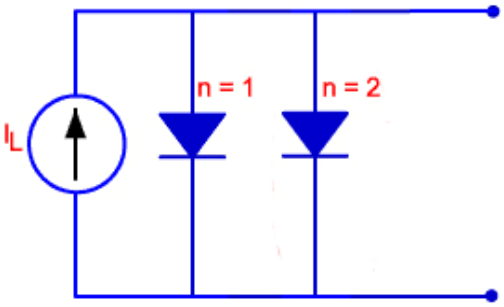

Figure 6.22: Circuit diagram of the simplified two diode model for solar cells.

The J/V characteristic of the simplified two-diode model is given by [27]:

$$J = J_{01}\left[\exp\left(\frac{V}{n_1 V_t}\right) - 1\right] + J_{02}\left[\exp\left(\frac{V}{n_2 V_t}\right) - 1\right] - J_{SC} \qquad (6.1)$$

The first two terms in equation (6.1) are recombination currents characterized by the saturation current densities J_{01} and J_{02} and the ideality factors n_1 and n_2, which are all independent of V. The first term represents recombination in the neutral base, and assumes that the minority carrier density is much lower than the majority carrier density (low-injection conditions), yielding an ideality $n_1=1$. The second term describes recombination in the SCR assuming that electron and hole concentrations have similar values, and Shockley–Read–Hall recombination via a single defect level near the center of the band gap. These assumptions yield an ideality $n_2=2$.

In equation (6.1), the saturation current density J_{01} depends on the effective diffusion length L_{eff} of minority carriers according to:

$$J_{01} = \frac{q D_n n_i^2}{N_A} \frac{1}{L_{\text{eff}}} \qquad (6.2)$$

where q is the elementary charge, n_i the intrinsic carrier concentration, and N_A is the density of ionized acceptor atoms in the p-type base of the cell. In a monocrystalline material, L_{eff} is given by:

$$L_{\text{eff}}^{\text{mono}} = L_n \frac{\cosh\left(\frac{W}{L_n}\right) + \sigma \sinh\left(\frac{W}{L_n}\right)}{\sinh\left(\frac{W}{L_n}\right) + \sigma \cosh\left(\frac{W}{L_n}\right)} \tag{6.3}$$

that considers a solar cell with a p-type base of thickness W, minority carriers (electrons) with diffusion length L_n, and a diffusion constant D_n. The recombination velocity S_b at the back contact is contained in σ, which is defined by $\sigma = S_b L_n / D_n$.

The current density J_{02} depends only on the diffusion length L_n of carriers, not including contact recombination. In order to simplify the analysis, without losing generality, it's possible to make two considerations that enable to use the same diffusion length to calculate J_{01} and J_{02} : i) the value of L_n does not depend on the position in the cell (SCR or bulk), and ii) in solar cells with high-SCR recombination, the effective diffusion length equals the bulk diffusion length ($L_{eff} = L_n$). This assumption imposes that L_n is smaller than the thickness W of the cell's base from equation (6.3). In cells that are not dominated by SCR recombination, this restriction is not needed because for such cells, the numerical value of the first term in equation (6.1) is much greater than the second one.

Considering these assumptions, the saturation current density J_{02} is expressed by:

$$J_{02} = \frac{q \pi D_n n_i V_t}{F_{\max}} \frac{1}{L_{\text{eff}}^2} \tag{6.4}$$

where F_{max} is the maximum electric field in the SCR under thermodynamic equilibrium. By approximating an abrupt junction, $F_{max}=(2qN_AV_{bi}/\varepsilon_s)^{1/2}$, where ε_s is the absolute dielectric constant of the semiconductor, and V_{bi} is the built-in voltage.

Having defined J_{01} and J_{02} as a function of L_{eff}, equation (6.1) can be written as a function of L_{eff}. At J=0, $V=V_{OC}$, and using the expressions for J_{01} and J_{02} given above, the J_{SC} expression becomes a quadratic function of $1/L_{eff}$:

$$J_{SC}=\frac{qn_i^2D_n}{N_A}\exp\left(\frac{V_{OC}}{V_t}\right)\frac{1}{L_{eff}}+q\pi n_iD_nV_t\sqrt{\frac{\varepsilon_s}{2qN_AV_{bi}}}\exp\left(\frac{V_{OC}}{2V_t}\right)\frac{1}{L_{eff}^2} \quad (6.5)$$

Defining $x=1/L_{eff}$ and $y=\exp(V_{OC}/2V_t)$, this equation reveals a symmetric expression of the form $xy^2+yx^2=const.$, indicating that both L_{eff} or V_{OC} are given analytically by the solution of a second-order polynomial. Since N_A has an exponent -1 in the first term, and -1/2 in the second term, equation (6.5) can be written as:

$$J_{SC}=z\frac{1}{L_{eff}}+\pi V_t\sqrt{\frac{D_n\varepsilon_sz}{2V_{bi}}}\frac{1}{L_{eff}^2} \quad (6.6)$$

where z is defined by:

$$z=qn_iD_n\exp\left[\frac{V_{OC}}{V_t}-\ln\left(\frac{N_A}{n_i}\right)\right] \quad (6.7)$$

By solving equation (6.6) for L_{eff}, the latter is expressed by:

$$L_{eff}=\frac{z+\sqrt{z^2+2\pi V_tJ_{SC}\sqrt{\frac{2D_n\varepsilon_sz}{V_{bi}}}}}{2J_{SC}} \quad (6.8)$$

Separating known from unknown quantities, ε_s and n_i are material constants. The value of D_n is obtained from measurements of the carrier mobility. Although the built-in voltage V_{bi} could be obtained by capacitance- voltage measurements, its exact value is actually not really needed to calculate L_{eff} from equation (6.8) because L_{eff} shows only a weak dependence $L_{eff} \propto V_{bi}^{-1/4}$. Thus, the only quantities is needed to calculate the effective diffusion length are J_{SC}, V_{OC}, and N_A. This statement holds independently of the material of the solar cell.

Figure 6.23 shows the increase of L_{eff} with the open-circuit voltage V_{OC} obtained from equations (6.6) and (6.7) for our GaSb bottom cell, using the short-circuit current density J_{SC} as the parameter. Since our structure is based on a n-doped base, we took into account the minority carrier diffusion constant D_p and the donor concentration N_D, which is included in the abscissa in order to consider all the possible doping densities. These curves were calculated using the following values: $\varepsilon_s = 1.39 \times 10^{-12}$ Fcm^{-1}, $n_i = 1.5 \times 10^{12}$ cm^{-3}, $D_p = 18$ cm^{2}s^{-1}, $V_{bi} = 0.726$ V, $N_D = 5.5 \times 10^{17}$ cm^{-3}.

All the curves show two regions:

1) the region of low L_{eff}, where the recombination in the SCR determines V_{OC}, and $n_{id} = n_2 = 2$, and
2) the region of higher L_{eff}, where V_{OC} is limited by bulk recombination, resulting $n_{id} = n_1 = 1$.

In our case, for $V_{OC} = 0.2$ V and $J_{SC} = 25$ mA/cm^2, L_{eff} is located in the first region, with a value of 0.8 μm. This result suggests a considerable recombination rate in the space charge region, which is probably too close to the structurally defected GaAs/GaSb interface.

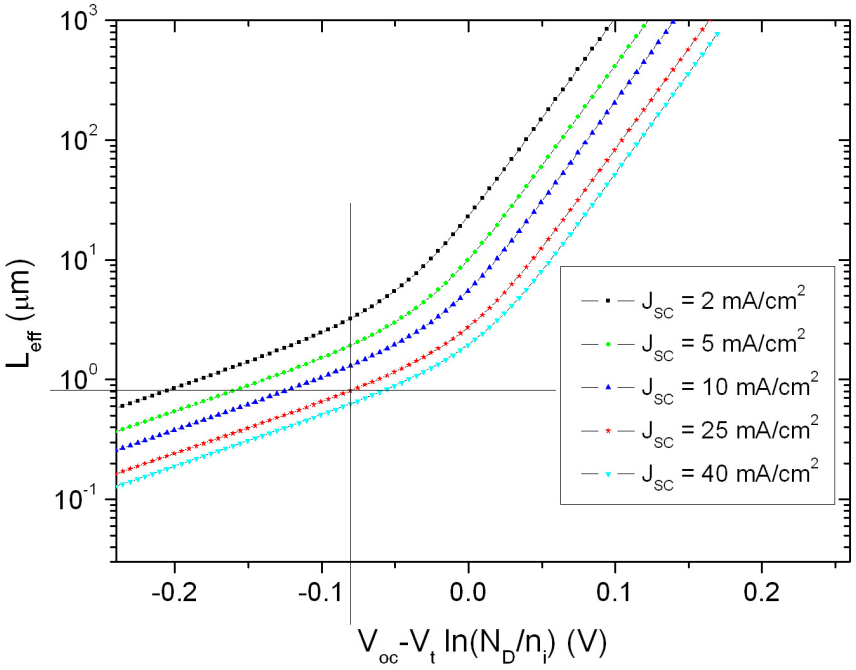

Figure 6.23: General solution for the effective diffusion length L_{eff} from equation (6.8) of a p-n solar cell. The relationship holds for both, cells with dominating recombination in the SCR (with an ideality n_{id}=2, bottom part of the curves) or in the bulk (n_{id}=1, top part of the curves). The curves shown here are calculated at 300 K (thermal voltage V_t=25.8 mV) and assuming an intrinsic carrier concentration n_i=1.5×10^{12} cm^{-3}. The intersection of the horizontal and vertical lines corresponds to our solar cells parameters (V_{OC}=0.2 V, J_{SC}=25 mA, N_D=5.5×10^{17} cm^{-3}), which give an effective diffusion length L_{eff}=0.8 μm.

6.5 GaAs tunnel junction

To achieve a high power density, the sub-cells constituting the multi-junction devices must be effectively electrically connected, in order to guarantee the sum of the voltage produced by the individual cells. Unfortunately, stacking the cells in tandem would result in a parasitic junction formed by the two dissimilar regions of the different cells. The better solution to this issue is to use a tunnel junction to separate the individual cells. The tunnel junction, which connects the p terminal of one sub-cell to the n terminal of an adjacent sub-cell, allows photons to pass through as well as pass current with minimal voltage loss.

It's therefore essential to us to develop an effective tunnel junction to interconnect the GaSb bottom junction with the GaAs top part of the structure. In this section, the physical fundamentals of the tunnel junction and the production of a GaAs p^{++}-n^{++} tunnel diode are presented.

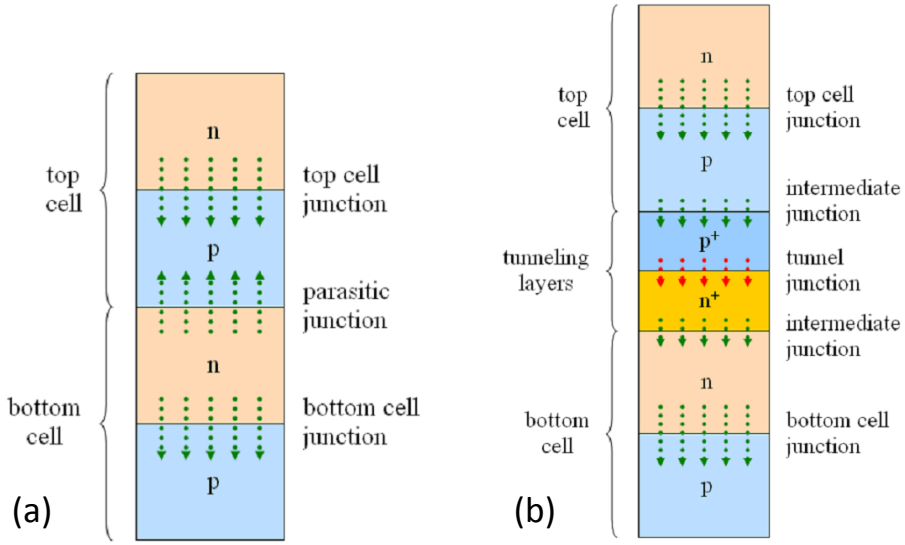

Figure 6.24: Tandem solar cells connected without (a) and with (b) the employment of p^+-n^+ tunnel junction.

6.5.1 Theory of the tunnel junction

Since its discovery in 1958 [28], the tunnel junction has been employed in a number of practical electronic circuit designs, being its major application the switching and oscillator circuits. The tunnel junction work principle is based on the fact that a charge carrier is capable, with a certain probability, of traversing a potential barrier with a potential energy higher than that of the charge carrier. This is known as tunnel effect. The probability that this occurs is a function of the height, width and shape of the potential barrier, the charge carrier energy and mass, etc. In particular, the tunnelling probability increases as the effective mass of the charge carrier and the potential barrier height decrease or when the electric field increases (i.e. the barrier width decreases).

A semiconductor tunnel diode consists of a n^{++}-p^{++} homo- or hetero-junction where both sides are so heavily doped that the n and p materials are degenerated. Due to the resultant thin space charge region, there exists the possibility that the normal thermal current characteristic of the p-n junction can be "shorted" by tunnelling through the narrow space charge region.

This concept is easily explainable using the usual simplified band diagram of a p-n semiconductor junction. At the thermal equilibrium, the band diagram of a tunnel homo-junction is reported in Figure 6.25.

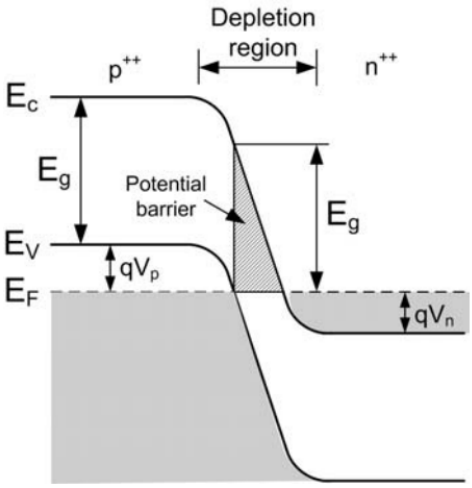

Figure 6.25: Band diagram of a tunnel homojunction at the thermal equilibrium, with the detail of the potential barrier created between the conduction and valence band.

As can be seen, at thermal equilibrium (0 V bias) the Fermi level is constant across the junction and it is placed within the bands of the semiconductor, due to its degeneracy. A region of completely empty states and a region of completely filled states appear in the p and n type regions, respectively, with a triangular-shaped potential barrier between them, through which a tunnelling process may occur. However, due to the position at different energies of the carries at thermal equilibrium, no tunnelling current can flow through the junction. In Figure 6.26, it is schematized the situation when a voltage bias is applied to the tunnel junction [18].

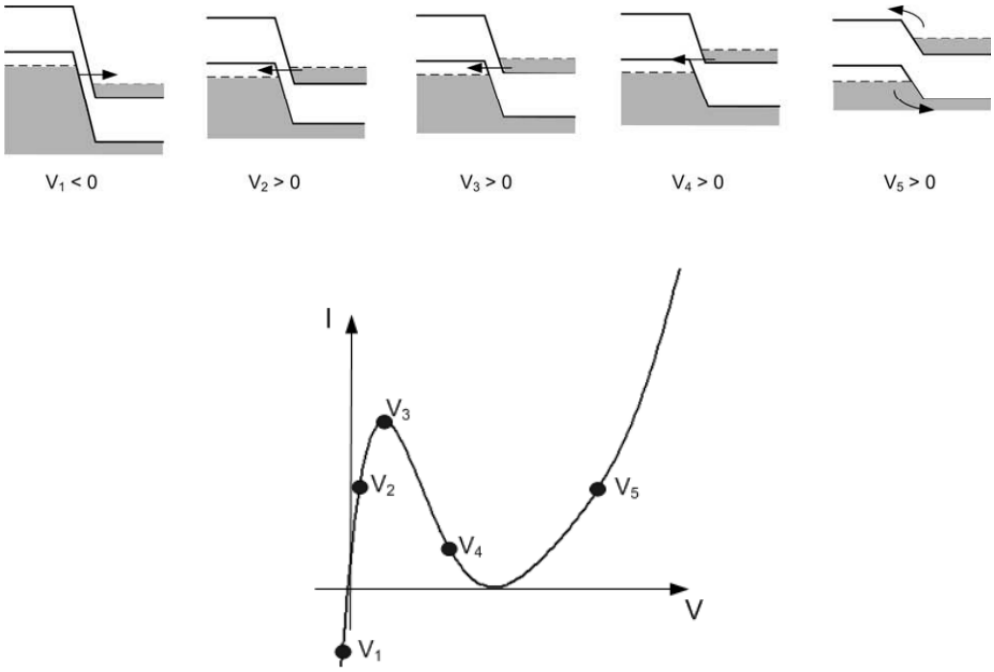

Figure 6.26: Schematic band diagrams of a tunnel homojunction for different voltage bias and the resulting I-V curve..

For negative voltage bias, the electrons can flow from the position of completely filled states in the valence band to the position of completely occupied states in the conduction band. The resulting current is negative, since it flows from the n-side to the p-side. If a positive voltage is applied, the situation is reversed: electron from the conduction band can flow to the valence band, giving rise to a positive current. However, if the voltage is increased, the situation comes to a point where there is no occupied energy states in the valence band at the same energy level as any occupied state in the conduction band, so tunnelling current becomes zero. If the voltage is further increased, the junction operates as a typical p-n diode under forward bias so that the direct current will flow, increasing exponentially with the applied voltage. Thus, the shape of the tunnel junction I-V curve, shown in Figure 6.26, is obtained.

Since the tunnel junctions inserted in a multi-junction solar cell are wanted to be able to manage the highest possible current with the minimum voltage drop (so as to minimize the series resistance), the tunnelling process must be favoured as much as possible. This can be achieved by reducing the effective height and width of the potential barrier. In practice, this is accomplished firstly by using very high doping levels. As can be deduced from Figure 6.25, the highest the doping level, the lower the potential barrier width. The high tunnelling current obtained with low band gap materials is due to the reduced potential barrier height obtained with these materials. Unfortunately, their high optical absorption affects negatively the multi-junction solar cell short circuit current.

Among all the parameters that affect the series resistance of the solar cell, the tunnel junction contribution can be the most important if it is not correctly designed and implemented. This fact has a special relevance in the case of photovoltaic systems operating under concentrated sunlight, since the concentrator optics generally forms a non-uniform illumination profile on the cell with a maximum irradiance significantly

higher than the average concentration level. Since tunnel junctions are usually designed and manufactured to operate properly at a given nominal concentration, assuming a uniform light profile, the lack of light uniformity impinging on the solar cell when working in a concentrator can bring about a significant drop in the efficiency. This is due to the fact that the peak current of the tunnel junction cannot be high enough to manage the current produced in the areas of the solar cell with the highest illumination level and, consequently, the tunnel junction does not work in the linear region, although the average current in the whole solar cell can be below the tunnel junction peak current. Consequently, it is important to develop tunnel junctions that can assure peak current well over the maximum level of concentrated light on the multi-junction solar cell together with negligible voltage drops and minor optical losses.

6.5.2 MOVPE growth of GaAs n^{++}-p^{++} tunnel junctions

To electrically connect the bottom and the top part of the tandem structure, four different tunnel junctions were realized, by growing on a p-type (100) GaAs substrate 150 nm thick p^{++}- and n^{++}-GaAs layers. The structure and the main parameters of the samples are shown in Figure 6.27 and table 6.1, respectively. Different both doping levels and doping sources were investigated in order to find the best electrical properties.

A delicate point in growing tunnel junctions is to master abrupt doping profiles: dopant species with low diffusion coefficients should be used. Silicon (from Si_2H_6 source) is ideal, in this sense, since it has a low diffusivity, while, as for p-doping, our MOVPE apparatus offers two type of doping sources: C, through the self-doping from C-rich metallorganic precursors, and Zn, from dimethylzinc liquid source. These chemical species, when used as dopants in III-V compounds, have complementary features:

- Carbon is a very low diffusive specie, but the self-doping gives a maximum donor density of ~5×10^{18} cm^{-3}, not sufficient to degenerate the p-GaAs as required to give a tunnel effect.
- Zinc, on the other hand, allows to achieve a maximum doping level of ~1×10^{20} cm^{-3}, but it shows a strong diffusivity.

Considering these issues, in all the structures we used Si for the GaAs n-type doping, while the p-type doping was obtained through C self-doping in the first two samples (named Tunnel01 and Tunnel02) and through Zn doping in the second two (Tunnel03 and Tunnel04).

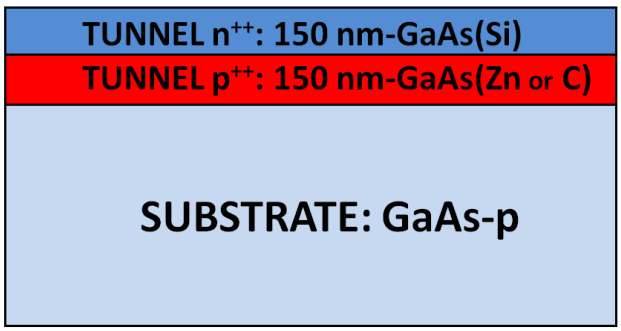

Figure 6.27: Structure of the tunnel diodes.

Table 6.1
Main parameters of the tunnel diodes: doping details of each layer, with the corresponding electrical characteristic.

Sample	p-type doping	n-type doping	I-V curve
Tunnel01	C: p=1×10^{18} cm^{-3}	Si: n=5×10^{18} cm^{-3}	Diode
Tunnel02	C: p=5×10^{18} cm^{-3}	Si: n=5×10^{18} cm^{-3}	Diode
Tunnel03	Zn: p=1×10^{20} cm^{-3}	Si: n=5×10^{18} cm^{-3}	Diode
Tunnel04	Zn: p=7×10^{19} cm^{-3}	Si: n=7×10^{18} cm^{-3}	Tunneling (J_p=500mA/cm^2)

The growth parameters were similar to those reported in paragraph 6.4.2. In this case, the substrates were 2" (100) p-doped GaAs wafers, which received the same pre-growth treatment than GaSb. The growth temperature for the self-doped p-layers was decreased from 600° to 500° C to enhance the C concentration density. In order to perform the electrical characterizations, standard photolithographic techniques were used for ohmic contacts and mesa structures.

Through I-V characterizations was evidenced that the only sample which provided the desired tunnelling current peak was Tunnel04, while the others three showed rectifying behaviours. The I-V curve relative to Tunnel04 is shown in Figure 6.28: the peak current density J_p is ~500 mA/cm^2, with a peak-to-valley current ratio of ~10. These results, which are comparable to those reported in the literature concerning GaAs p-n tunnel junction obtained by Si and Zn doping [29], show that Tunnel04 represents an efficient electrical interconnection between the top and the bottom junctions of the tandem structure, in low-concentrated light (<10× suns). Both negligible voltage drops and minor optical losses are provided.

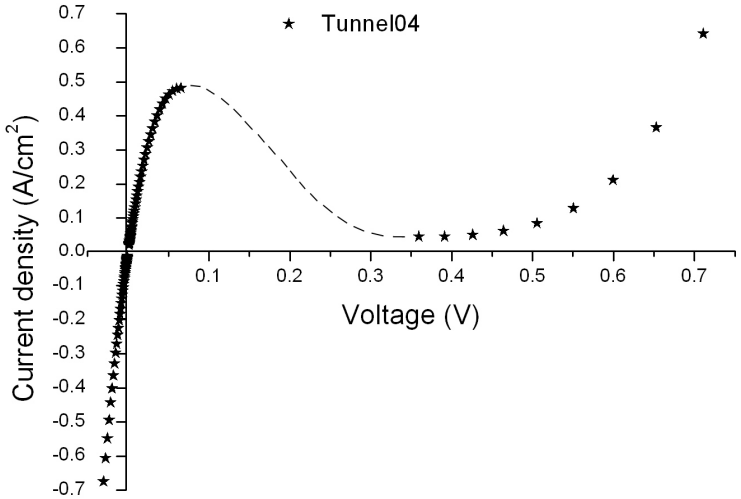

Figure 6.28: I-V curve of Tunnel04 sample, with the characteristic tunneling current peak. The peak current density J_p is ~500 mA/cm^2, with a peak-to-valley ratio of ~10.

6.6 GaAs/GaSb: the tandem structure prototype

A first attempt to produce a prototype of a tandem structure, named MJCELL01, was realized in the last period of my PhD research. As the bottom junction was used the GaAs/GaSb structure with the highest p-doping level of the GaAs layer ($p=1x10^{20}$ cm^{-3}), which provided the best photovoltaic properties, while the electrical interconnection was provided by the Tunnel04 structure, which showed a good current peak density. The top junction was the p-i-n GaAs cell that was developed in the past in our laboratory, showing a good efficiency light conversion, equal to ~17% (V_{OC}=0.95 mV, J_{SC}=28 mA/cm^2, FF=0.83 at AM0) for large area samples (8 cm^2) and >20% on 500 μm large dots of a test sample. The whole structure, shown in Figure 6.29, was monolithically grown on a n-doped GaSb substrate in a single MOVPE growth run. The only non-GaAs grown layer is the AlGaAs window that limits the surface recombination of the minority charge carriers.

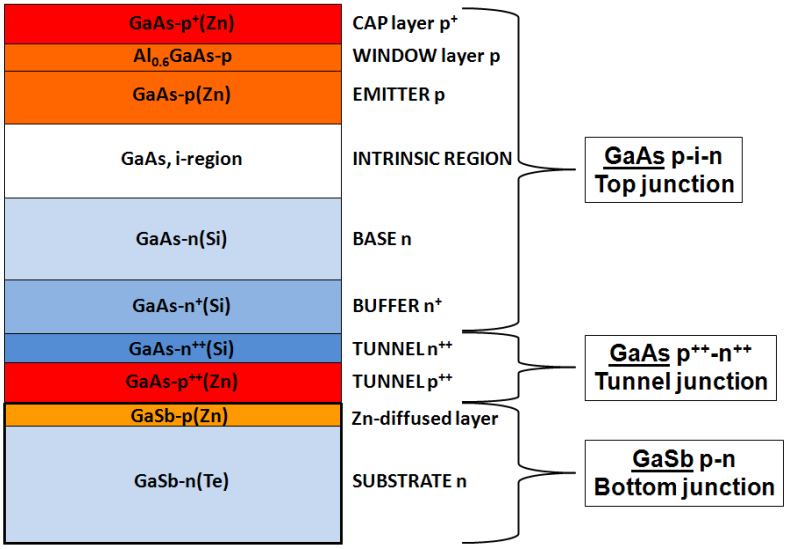

Figure 6.29: Main structure of the full GaSb/GaAs tandem sample MJCELL01, with the three main constituent parts evidenced.

6.6.1 Experimental procedures

The growth was performed with our horizontal low-pressure MOVPE reactor. The metal-organic precursors were terbutylarsine (TBAs), trimethylgallium (TMGa) and trimethylaluminum (TMAl) for As, Ga and Al, respectively, while dimethylzinc (DMZn) and hydrogen-diluted disilane (Si_2H_6) where used as the p- and n-doping sources. Palladium-purified H_2 worked as carrier gas. The substrate was a 2" (100) Te-doped GaSb wafer with a n-doping level of ~5.5×10^{17} cm^{-3}, obtained by low temperature Hall effect measurements, which received our standard pre-growth treatment. The growth was carried out at a total pressure of 50 mbar and a total gas flow of 6.8 l/min. The partial pressure of the precursors were: $1.1\times10^{-3}<pTMGa<5.6\times10^{-3}$ mbar; $2.2\times10^{-2}<pTBAs<1.45\times10^{-1}$ mbar; $pTMAl=6.4\times10^{-3}$ mbar. The Zn/Ga and Si/Ga partial pressure ratios ranged between 6×10^{-3}-1.0 and 2.6×10^{-5}-5×10^{-3}, respectively. The V/III ratio was 26 and 5.2 for the GaAs and AlGaAs growth, respectively. The growth temperature T_g ranged between 600° and 650° C through the 167 minutes of the whole process.

In order to perform a preliminary light I-V characterization by solar simulator, proper 7×7 mm^2 prototype devices were manufactured as reported in paragraph 6.4.5.

6.6.2 Preliminary characterization

The photovoltaic response of the 7×7 mm^2 MJCELL01, obtained by solar simulator measurements, showed a behaviour similar to that of the GaSb bottom junction, with the following photovoltaic values: V_{OC}=310 mV, J_{SC}=20 mA/cm^2 (corrected to an incident light power of 1000 W/m^2), FF=0.37, η=2.3% (Figure 6.30).

These results relate to a first sample of the complete structure, nevertheless it should be noted that the V_{OC} and J_{SC} measured values are quite far from the expected ones, given, respectively, by the sum of the voltages produced in the single junctions and by the photo-current relative to the lowest current-producing junction. In this ideal condition V_{OC} should be greater than 1 V, with 0.95 and 0.20 V respectively coming from the top and the bottom junction, while J_{SC} should be limited by the GaSb junction value, equal to ~25 mA/cm^2.

Notwithstanding the very preliminary results, some remarks can be pointed out. In a 160 minutes long MOVPE growth, many parameters can deviate from the optimal values. One of the most delicate part of our structure, which is fundamental for the overall optimal working, is the tunnel junction, especially because of the presence, in a very thin GaAs layer, of a high concentration of Zn atoms, which have a large diffusion coefficient. In fact, if Zn would diffuse from the p-doped layer of the tunnel diode (which also acts as diffusion source for the formation of the GaSb p-n junction) to the n-doped layer, it would create a compensated GaAs region that would hinder the tunnelling effect by the increase of the space charge region. On the other hand, the further diffusion of Zn from the p-tunnel layer toward the GaSb substrate is not expected, since neither a 2 hours 660° C annealing showed an increase in the Zn diffusion depth into the substrate (see SIMS analysis in paragraph 6.4.4). Therefore, the degradation of the tunnel junction, during the growth process, is probably the main cause of the low light conversion properties of MJCELL01.

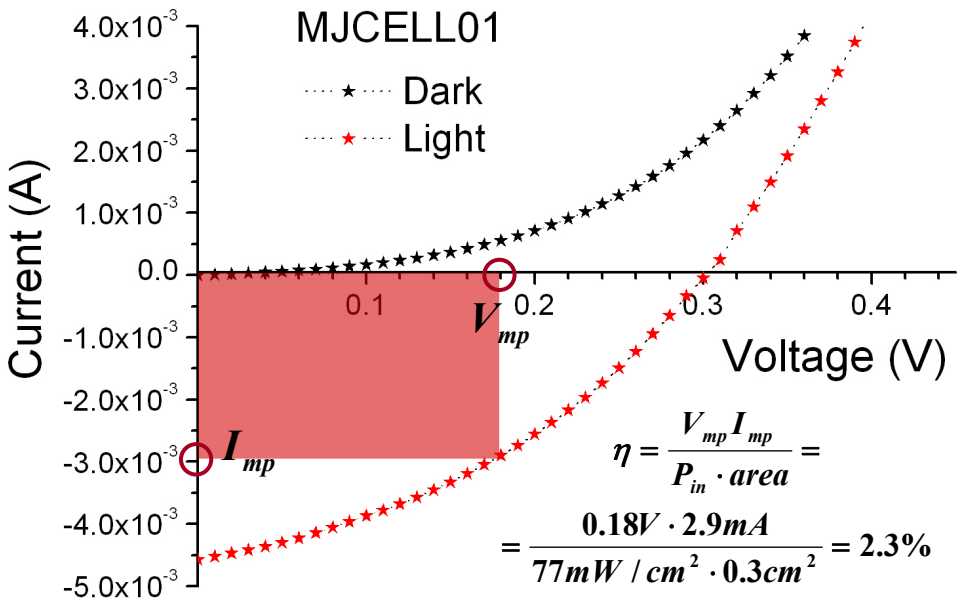

Figure 6.30: Light I-V characteristic of 7x7 mm² MJCELL01 sample with the resulting conversion efficiency. The red rectangle represents the maximum power that can be extracted from the device.

6.7 Conclusions

The subject of the second part of my PhD research was the realization of a relatively simple monolithic tandem structure for photovoltaic applications. In particular, my main purpose was to study and develop a p-n junction, which was able to absorb, and efficiently convert, the low energy radiation, suitable to represent the bottom part of the whole structure. The top part, consisting of a p-i-n GaAs junction, was, in fact, already grown in the past in our laboratories, with good photovoltaic properties, such as η>17% for a 8 cm^2 sample.

In order to achieve the bottom junction, we deposited by MOVPE a Zn-heavily doped GaAs layer on n(Te)-doped GaSb substrates, so that the high temperature of the growth process (T_g=600° C) induces the interdiffusion of Zn from GaAs in GaSb, forming a buried GaSb p-n homojunction. The strain relaxed GaAs layer is expected to be ready for the re-growth of a n^{++}-p^{++} GaAs tunnel diode, interconnecting the GaSb junction with the p-i-n GaAs top cell.

GaSb bottom junction

Both different Zn doping levels and time-temperature annealing values were investigated in order to control the depth of the junction, which has a relevant role in controlling the collection of light-generated carriers. The samples showed I-V characteristics with diode ideality factors between 1.1 and 1.7 and good rectification properties, which improve with the lowering of the Zn doping levels. SIMS profiles pointed out a quite limited Zn diffusion depth in GaSb, with a maximum value of ~100 nm in the highest doped sample ($p=1x10^{20}$ cm^{-3}). This thickness results considerably lower than the one typical of traditional diffusion methods from oversaturated vapour phase, which exceeds 0.5 μm only at T=450° C. Neither temperature nor time in the annealing process proved to extend the penetration depth

of Zn into the substrate, obtaining a quite shallow junction. This is mainly explained by the fact that the Zn atoms taking part in the diffusion process belong to a very thin fraction of the GaAs layer close to the hetero-interface and occupy almost exclusively substitutional sites. For what concerns the photovoltaic properties of the structure, obtained by a solar simulator on 7x7 mm^2 specifically processed samples, the best structures resulted to be those with the highest Zn doping level ($p=1x10^{20}$ cm^{-3}): both the open-circuit voltage (V_{OC}=200mV) and the short-circuit current (J_{SC}=25mA/cm^2 at AM1.5) were quite encouraging, while the fill factor was only 0.35, limiting the conversion efficiency η to ~1.8%. The latter result, together with the estimated effective diffusion length of 0.8 μm and the diode ideality factor of 1.7, contribute to indicate that the structure is not yet optimized for solar cell operation, probably because the GaSb homo-junction is too close to the defected metallurgical interface. Further efforts will be made to push the effective junction line more deeply into the substrate.

GaAs n^{++}-p^{++} tunnel junction

The tunnel junction is of primary importance for the good working of the entire structure, since it allows both photons and current to pass through with minimal voltage loss.

To electrically connect the bottom and the top part of the tandem structure, four different tunnel junctions were realized, by growing on a p-type GaAs substrate p^{++}- and n^{++}-GaAs thin layers. Different both doping levels and doping sources, in particular for p-type doping, were investigated in order to find the best electrical properties.

Good tunnelling properties were obtained by Tunnel04 sample, through doping levels of 7×10^{18} and 7×10^{19} cm^{-3} for the n- and p-type layers, respectively. The first was obtained by Si, an ideal dopant thanks to its very low diffusivity, while the latter

through Zn, which has a high diffusion coefficient but allows to achieve high doping levels (>1×10^{20} cm^{-3}). This tunnel diode provided a peak current density J_p=500 mA/cm^2, with a peak-to-valley current ratio of ~10, which is sufficient to guarantee an efficient electrical interconnection between the top and the bottom junctions of the tandem structure, in low-concentrated light (<10× suns).

GaAs/GaSb complete tandem structure

A first complete tandem structure, named MJCELL01, was realized in the last period of my PhD research. In a single MOVPE run, the Tunnel04 junction, whose GaAs p-layer also acted as diffusion source for the formation of the buried GaSb p-n junction, and the p-i-n GaAs cell were monolithically grown on a n-doped GaSb substrates. In this way, the whole structure results to be entirely based on GaAs layers, with different doping levels, and a GaSb substrate, apart from a thin $Al_xGa_{1-x}As$ window layer.

The photovoltaic response of the 7×7 mm^2 MJCELL01 showed a behaviour similar to that of the GaSb bottom junction, with V_{OC}=310 mV, J_{SC}=20 mA/cm^2 at AM1.5, FF=0.37 (η~2.3%). These data, which refer to a very first attempt to realize a prototype of the tandem structure, are quite far from the expected ones, calculated from the properties of the single components.

The degradation of the tunnel junction during the 160 minutes long growth process (T_g =600-650° C) is probably the main cause of the low light conversion properties of MJCELL01. Zn, in fact, could have diffused from the p-doped layer of the tunnel diode to the n-doped layer, forming a compensated GaAs region, which hinders the tunnelling effect by the increase of the space charge region. An accurate study of the tunnel junction properties for high temperature and long time annealing, is then required.

References

[1] W. Guter, J. Schone, S.P. Philipps, M. Steiner, G. Siefer, A. Wekkeli, E. Welser, E. Oliva, A.W. Bett, and F. Dimroth, Appl. Phys. Lett. **94**, 223504 (2009)

[2] L.M. Fraas, J.E. Avery, V.S. Sundaram, V.T. Dinh, T.M. Davenport, 21st IEEE Photovoltaic Specialists Conference, Kissimmee, Florida, pp. 190–195 (1990)

[3] A.W. Bett., O.V. Sulima, Semicond. Sci. Technol. **18**, S184–S190 (2003)

[4] S. Dakshinamurthy, S. Shetty, I. Bhat, C. Hitchcock, R. Gutmann, G. Charache, M. Freeman, J. Electron. Mater. **28**, 355 (1999)

[5] V.M. Andreev, S.V. Sorokina, N.K. Timoshina, V.P. Khvostikov, M.Z. Shvarts, Semiconductors **43**, 668–671 (2009)

[6] F. Dimroth, C. Agert, A.W. Bett, J. Cryst. Growth **248**, 265-273 (2003)

[7] L.M. Fraas, H.X. Huang, S.Z. Ye, S. Hui, J. Avery, R. Ballantyne 1997 3rd NREL Conf. on the Thermophotovoltaic Generation of Electricity (AIP Conf. Ser.) vol 401, ed T J Coutts, C S Allman and J Benner pp 33–40 (1997)

[8] C. Alibert, A. Joulliè, A.M. Joulliè, C. Ance, Phys. Rev. B **27**, 4946 (1983)

[9] A. Bignazzi, E. Grilli, M. Guzzi, C. Bocchi, A. Bosacchi, S. Franchi, R. Magnanini, Phys. Rev. B **57**, 1 (1998)

[10] N. Steljan, Rev. Romanian Phys. **67**, 3032 (1970)

[11] J. Basinsky, C.C.J. Kwan, J.C. Wolley, Canadian J. Phys. **50**, 1068 (1972)

[12] H. Enreich, J. Appl. Phys. **32**, 2155 (1961)

[13] A. Bosacchi, S. Franchi, P. Allegri, V. Avanzini, A. Baraldi, C. Ghezzi, R. Magnanini, A. Parisini, L. Tarricone, J. Cryst. Growth **150**, 844 (1995)

[14] C.A. Wang, K.F. Jensen, A.C. Jones, H.K. Choi, Appl. Phys. Lett. **68**, 400 (1996)

[15] D. Donetsky, J. Chen, L. Shterengas, G. Kipshidze, D. Westerfeld, J. of Elec. Mat. **37**, Number 12, 1770-1773 (2008)

[16] S.K. Lohokare, O.V. Sulima, V.A. Solovev, S.V. Ivanov, D.W. Prather, Electron. Lett. **40**, 1377-1378 (2004)

[17] K.Taira, I. Hase, H. Hawai, Electron. Lett. **25**, 1708-1709 (1989)

[18] S.M. Sze, Semiconductor Devices (Wiley, New York, 2002)

[19] C. Mourad, D. Gianardi, R. Kaspi, J. Appl. Phys. **88**, 5543 (2000)

[20] S.H. Huang, G. Balakrishnan, M. Mehta, A. Khoshakhlagh, L.R. Dawson, D. L. Huffaker, Appl. Phys. Lett. **90**, 1619002 (2007)

[21] R.K. Huang, C.A.Wang, C.T. Harris, M.K. Connors, D.A. Shiau, J. Elec. Mat. **33**, 1406 (2004)

[22] A.W. Bett, S. Keser, O.V. Sulima, J. Cryst. Growth **181**, 9-16 (1997)

[23] L.R. Weisberg, J. Blanc, Phys. Rev. **131**, 1548–1552 (1963)

[24] M.S. Abrahams, J. Appl. Phys. **37**, 2596 (1966)

[25] K. Taretto, U. Rau, J.H. Werner, J. Appl. Phys. **93**, 5447 (2003)

[26] P.A. Basore, IEEE Trans. Electron Devices ED-**37**, 337 (1990)

[27] A. Goetzberger, B. Voss, J. Knobloch, Sonnenenergie: Photovoltaik (Teubner, Stuttgart, p.94, 1997)

[28] L. Esaki, Phys. Rev. **109**, 603 (1958)

[29] P. Basmaji, M. Guittard, A. Rudra, J.F. Carlin, P. Gibart, J. Appl. Phys. **62**, 2103 (1987)

Conclusions and perspective

This PhD thesis dealt with an extensive study of multiple band gap heterojunctions for advanced photovoltaic applications. Two types of structures, obtained by metal organic vapour phase epitaxy (MOVPE) and based on III-V semiconductors (in particular GaAs, GaSb and InGaP), were examined as potential candidates for third generation photovoltaics.

A quantum well structure based on the InGaP/GaAs system, which was grown by MOVPE according to the structural parameters suggested by the workgroup of Prof. Barnham at the Imperial College of London, was here studied with particular attention to its spectral response. The structure, conceived to be part of a quantum well solar cell (QWSC), consisted in the growth of an InGaP p-i-n junction in whose nominal intrinsic region were stacked 30 periods of GaAs quantum wells (8 nm thick) and InGaP barriers (12 nm thick). The response to the light of the structure was investigated by an accurate photoelectric spectroscopy (PES) study: both the photocurrent (PC) and photovoltage (PV) signals were detected by a standard lock-in technique, as a function of the wavelength, at different sample temperatures and for different frequencies of the exciting light, modulated by a chopper.

The spectral response of the structure evidenced excitonic transitions between the discrete energy levels in the valence- and conduction-band of QWs. Their energy positions and temperature behaviour were consistent with the theoretical expectations, indicating a good control of the growth process and a high QW/barrier structural

quality. Although the presence of the 30 QWs extended the light absorption spectrum, the conversion efficiency turned out to be quite low. The reason of this behaviour is almost certainly related to an undesired background doping of the nominally intrinsic InGaP alloy in the MQWs, which shows *p*-type conductivity with a net acceptor density in the 10^{16} cm^{-3} range, higher than the one required by the QWSC project (less than 10^{15} cm^{-3}). In this way, the electric field profile significantly varies through the intrinsic region and the transit time of the photocarriers is not competitive with the recombination rate. A further investigation of the MOVPE growth processes parameters will be performed in order to solve this problem and so improve the photovoltaic response of these structures.

However, interesting and original results were obtained through the PES investigation by varying the modulation frequency of the optical excitation. It was demonstrated that the PV and PC signals are influenced by the effects due to the uncompleted depletion of the MQW region. The time constant τ, controlling the dynamic response of the structure to the modulated exciting signal, resulted to be related to the thermoionic emission rate of holes over the QW barriers, which is the transport mechanism controlling the resistance R of the undepleted MQW region. This phenomenon had been already evidenced by a previous admittance spectroscopy (AS) study, which revealed a maximum in the isothermal conductance over frequency $G(\omega)/\omega$ curves at a *resonance* frequency ϖ, which is inversely proportional to R. The PES measurements resulted complementary to the AS ones, extending the possibility of a spectroscopic investigation in a different range of frequency of the modulated exciting signal. It was evidenced that the photoelectric signals behave as complex physical quantities so that the variations of both the amplitude and the phase of PC and PV must be carefully monitored. By considering also their dependence on the modulation frequency of the external perturbation, it was possible to avoid misunderstandings in the interpretation of PE data: a peculiar non-monotonic

behaviour of these quantities was quantitatively described as due to the same *resonance* phenomenon pointed out by AS.

The investigation, for both the PE signals, of the temperature dependence of the amplitude evidenced an abrupt step in the PE intensities at the *resonance* condition, together with a peculiar behaviour of the phase shift with respect to the exciting modulated light. On the other hand, the analysis of the curves in the temperature ranges far from the *resonance* step suggested that the PV intensity is dominated by the thermoionic electron emission over the barriers, whereas the PC intensity is significantly influenced by the presence of generation/recombination centres.

A second type of photovoltaic structure was designed and realized, consisting in a relatively simple monolithic GaAs-based tandem structure grown on GaSb substrates. By taking advantage of the high temperature of the growth process (T_g=600° C), the deposition of a highly Zn doped GaAs layer enabled the Zn diffusion into the Te-doped (n-type) GaSb substrate, forming a buried GaSb p-n homojunction. By depositing additional GaAs layers with appropriate doping levels, a tunnel and a top junction could then be stacked, to obtain the final tandem structure. The originality of the proposal is related both to the method employed to activate the Zn diffusion in GaSb, and also to the assessment of the GaAs-on-GaSb epitaxial growth, covered in literature only by a single work. The possibility to realize a tandem cell by properly modulating the doping of the same compound (GaAs, in this case), thus making the fabrication process very simple, is the main advantage of this structure. The choice of GaSb substrates instead of the more frequently used Ge for the bottom junction was related to the better optical properties of the former. On the other hand, the use of GaSb introduces problems due to its high lattice misfit with GaAs, which must be tackled in order to improve the efficiency of the structure. The critical aspects of the project are therefore related (i) to the control of the penetration depth of Zn in GaSb and (ii) to the reduction of the effects of threading dislocations. A first prototype of

the complete tandem structure (named MJCELL01) was successfully realized with the growth parameters selected from the preliminary investigation of the single parts of the structure, in particular of the bottom and tunnel junctions, since the GaAs top junction had previously been grown in our laboratories, showing good photovoltaic properties (η>17% for a 8 cm^2 sample).

For the realization of the bottom junction, different Zn doping levels and time/ temperature annealing values were tested, to investigate their effects on the junction depth. In all cases, a buried p-n homojunction was obtained, showing I-V characteristics with diode ideality factors between 1.1 and 1.7 and good rectification properties, which improve with the lowering of the Zn doping levels. As concerns the photovoltaic properties of the junction, studied by a solar simulator on 7x7 mm^2 specifically processed samples, the best structures resulted those with the highest Zn doping level in GaAs ($p=1x10^{20}$ cm^{-3}): both the open-circuit voltage (V_{OC}=200mV) and the short-circuit current (J_{SC}=25mA/cm^2 at AM1.5) were quite encouraging, while the fill factor was only 0.37, limiting the conversion efficiency η to ~1.8%. The latter result, together with the estimated effective diffusion length of 0.8 μm and the diode ideality factor of 1.7, indicates that the structure is not yet optimized for solar cell operation, probably because the GaSb homojunction is too close to the defected metallurgical interface. In fact, SIMS profiles pointed out a quite limited Zn diffusion depth in GaSb, with a maximum value of ~100 nm, which resulted considerably lower than the typical values obtained by the traditional diffusion methods from oversaturated vapour phase (over 0.5 μm at only T=450° C). The role of the misfit dislocations in the GaAs layer in slowing down the Zn diffusion will be object of future investigations. Accurate structural analyses by transmission electron microscopy (TEM), cathodoluminescence (CL) and electron beam-induced current (EBIC) techniques of the GaAs layers and, in particular of the GaAs/GaSb interface, are planned or already in progress. Also the growth of GaAs on GaSb by MOVPE,

poorly investigated in the literature, deserves a deeper study. Further efforts will be made to push the effective junction plane more deeply into the substrate by using different growth and annealing conditions or alternative diffusion methods.

To electrically connect the bottom and the top parts of the tandem structure, a tunnel junction was realized. Good tunnelling properties were obtained by a GaAs p-n junction with doping levels of 7×10^{18} and 7×10^{19} cm^{-3} for the n- and p-type layers, respectively, resulting the best one among four structures fabricated using different sets of growth parameters. This tunnel diode provided a peak current density J_p=500 mA/cm^2, with a peak-to-valley current ratio of ~10, sufficient to guarantee an efficient electrical interconnection between the top and the bottom junctions of the tandem structure, in low-concentrated light (<10× suns).

In preliminary measurements, the photovoltaic response of a 7×7 mm^2 shaped MJCELL01 showed a behaviour similar to that of the GaSb bottom junction, with V_{OC}=310 mV, J_{SC}=20 mA/cm^2, FF=0.37 (η=2.3%) at AM1.5. These data, which refer to a very first attempt to carry out the tandem structure, are quite far from the optimal ones, calculated from the properties of the single components of the device.

The degradation of the tunnel junction during the 160 minutes long growth process (T_g=600-650° C) is probably the main cause of the low light conversion properties of MJCELL01. An accurate study of the tunnel junction properties for high temperature and long time annealing is then required. Moreover, further tunnel diode architectures and concentration doping levels will be investigated.

As for the p-i-n GaAs junction, the light conversion efficiency will be studied by varying the thickness of the single layers that constitute the structure, with a particular attention to the role of the intrinsic region.

Ringraziamenti

Al termine di questo periodo triennale vorrei esprimere la mia gratitudine verso i miei tutors, Prof. Luciano Tarricone e Prof. Antonella Parisini, per la guida e il supporto che hanno saputo darmi in ogni occasione. Grazie a Salvatore Rino Vantaggio, per il suo inestimabile contributo in laboratorio e per i bei momenti passati insieme.

Inoltre vorrei ringraziare tutte le persone che hanno contribuito allo sviluppo del mio lavoro di ricerca:

- Dr. E. Gombia (IMEM-CNR, Parma) Grazie di tutto!
- Dr. C. Bocchi (IMEM-CNR, Parma)
- Dr. G. Salviati (IMEM-CNR, Parma)
- Mr. A. Motta (IMEM-CNR, Parma)
- Dr. A. Bosio (Università di Parma)
- Dr. R. Jakomin (LPN-CNRS, Marcoussis)
- Prof. A. Gasparotto (Università di Padova)

Grazie alla mia famiglia e ai miei amici, non avrei potuto essere più fortunato.

Questo lavoro è stato intrapreso nell'ambito del **Progetto FIRB/MUR2007-10 "FOTOENERGIA"**, coordinato dal centro ricerche ENEA di Portici (NA). Ringrazio il Dr. Francesco Roca (ENEA) per la disponibilità dimostratami.